
The Geometric Mechanics of Contrastive Learning: Alignment Potentials, Entropic Dispersion, and Modality Gap

Yichao Cai¹ Zhen Zhang¹ Yuhang Liu¹ Javen Qinfeng Shi¹

Abstract

InfoNCE-based contrastive learning is often characterized as promoting alignment and uniformity, yet the induced population geometry and the reasons multimodal training can preserve a modality gap remain underexplored. We present a measure-theoretic view where training reshapes probability measures on a fixed embedding manifold. In the large-batch limit, we prove value and gradient consistency, showing that stochastic InfoNCE tracks a closed-form deterministic energy and revealing a geometric bifurcation between unimodal and symmetric multimodal regimes. Unimodally, the intrinsic functional over the representation measures is strictly convex with a unique Gibbs equilibrium; at low temperature, entropy only breaks ties among well-aligned solutions, so uniformity is entropic dispersion within the alignment basin. Multimodally, symmetric InfoNCE contains a persistent negative symmetric divergence coupling: at fixed temperature, each modality’s marginal acts as a logarithmic barrier shaping the other’s effective landscape, which can structurally favor a population-level modality gap under conditional heterogeneity. We validate these predictions in controlled synthetic settings and by measuring the divergence gap on pretrained CLIP embeddings on real-world data. Our analysis shifts the lens from pointwise discrimination to population geometry, suggesting that closing the modality gap requires explicitly regularizing cross-modal divergence in addition to pairwise alignment.

1. Introduction

Contrastive learning traces back to noise-contrastive estimation and density-ratio principles (Gutmann & Hyvärinen, 2010; Mnih & Teh, 2012), and is now a central tool for

¹Australian Institute for Machine Learning (AIML), Adelaide University, South Australia 5000, Australia. Correspondence to: Yichao Cai <yichao.cai@adelaide.edu.au>.

Preprint. March 17, 2026.

self-supervised and multimodal learning. InfoNCE-type objectives, introduced via contrastive predictive coding and related mutual-information surrogates (Oord et al., 2018; Poole et al., 2019; Tschannen et al., 2020), underpin multimodal foundation models such as CLIP and ALIGN (Radford et al., 2021; Jia et al., 2021). Yet a persistent empirical puzzle remains: multimodal contrastive training can yield strong *pairwise* alignment while the modality *marginals* remain separated (Liang et al., 2022). Why does matching pairs fail to match distributions? Equivalently, what population energy does InfoNCE induce over representation measures, and which equilibria does its geometry favor?

Existing theory leaves this mechanistic question partially open (see App. A for a broader review). Density-ratio analyses characterize the optimal critic as pointwise mutual information (Gutmann & Hyvärinen, 2010; Oord et al., 2018), but do not directly describe the deterministic descent directions generated by the softmax gradient, nor how these directions reshape population-level *measures*. The alignment–uniformity view (Wang & Isola, 2020) clarifies asymptotic optima via decomposition, but largely abstracts away coupled training dynamics between modalities. Identifiability results offer recovery guarantees under explicit generative assumptions (Zimmermann et al., 2021; Liu et al., 2026), addressing what is learnable in principle rather than the geometric forces that shape the learned marginals. These gaps are especially acute in multimodal settings, where positives arise from heterogeneous data-generating laws and the modality gap appears as a structural phenomenon.

We therefore adopt a measure-theoretic viewpoint that makes population geometry explicit (see Fig. 1 for a roadmap). In the feature-normalized regime, we treat the embedding space \mathcal{Z} as a fixed compact manifold with volume measure μ . Encoders push data forward to \mathcal{Z} , inducing modality-specific representation laws and a positive-pair law. Under the exponential similarity kernel, the InfoNCE denominator is a Monte Carlo estimate of a population *partition field*: a kernel-averaged functional of the current representation law that determines the softmax gradient direction. Training can thus be viewed as transporting probability mass on a fixed manifold along kernel-induced fields, shifting attention from parameters to intrinsic population geometry.

A unified analytical pipeline

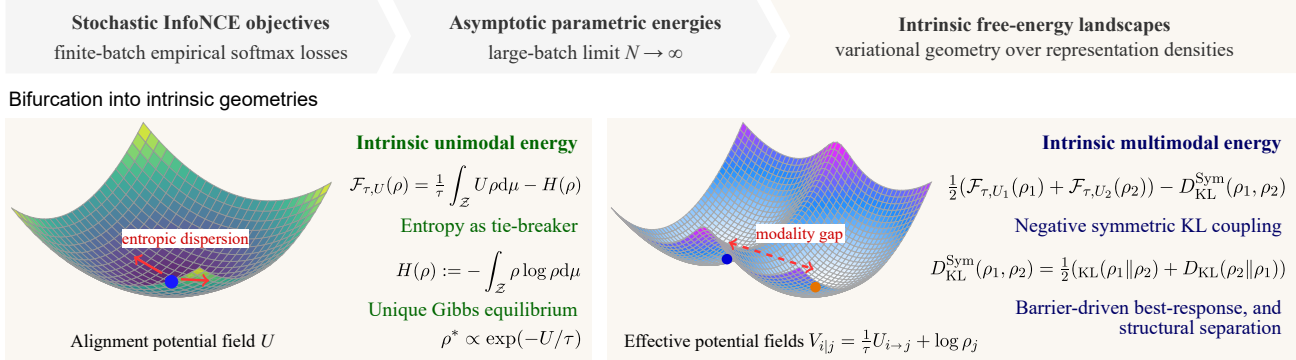


Figure 1. A unified analytical pipeline for contrastive learning geometry. Starting from stochastic InfoNCE losses, the large-batch limit yields deterministic parametric energies, which in turn lift to intrinsic free-energy landscapes over representation densities. At this intrinsic level, the geometry bifurcates: unimodally, the landscape is strictly convex, with entropy acting as a tie-breaker and yielding a Gibbs equilibrium; multimodally, a negative symmetric KL coupling induces cross-coupled barriers, producing a modality gap.

This lens yields an explicit deterministic energy description of InfoNCE. Under mild regularity, per-sample gradients are uniformly bounded, and in the large-batch limit, the stochastic loss is both value- and gradient-consistent with a closed-form population energy: the softmax denominator converges to the partition field, so gradient descent follows a deterministic direction at the level of representation measures. To separate geometry from parametrization, we lift the population energy to an *intrinsic* variational functional over probability measures on \mathcal{Z} , depending only on the induced laws. In the unimodal case, this functional is strictly convex, with a unique Gibbs equilibrium. In the low-temperature regime, the equilibrium concentrates in regions of high alignment, while entropy governs how mass spreads *within* the aligned basin—reinterpreting “uniformity” (Wang & Isola, 2020) as an entropic tie-breaker among near-optimal aligned configurations, rather than a force opposing alignment.

The multimodal case is qualitatively different. For symmetric InfoNCE (Radford et al., 2021), we again obtain a deterministic large-batch limit, but the intrinsic geometry becomes cross-coupled: heterogeneous modalities generally induce different conditional laws, hence different alignment fields. The resulting intrinsic variational objective contains a *negative* symmetric divergence coupling between modality marginals that persists at fixed temperature, with temperature controlling only a tractable KDE perturbation. This coupling makes each modality act as a logarithmic barrier in the other’s effective landscape, inducing boundary-seeking co-adaptation rather than convergence to a shared equilibrium. Exact marginal matching arises only under a knife-edge compatibility condition on the induced conditional laws that is rarely satisfied for multimodal paired data, so the modality gap emerges as a generic consequence in the analyzed regime. Our study therefore suggests that closing this

cross-modal representational gap often calls for explicit regularization of cross-modal divergence, not merely stronger pairwise alignment.

Contributions. Our main contributions are: (i) large-batch value and gradient consistency results that bridge stochastic InfoNCE training to explicit deterministic energy landscapes (Thms. 3.1 and 4.1); (ii) a characterization of unimodal InfoNCE geometry as strictly convex with a unique Gibbs equilibrium, and a reinterpretation of “uniformity” as an entropic tie-breaker within the alignment basin (§ 3); (iii) a derivation of the multimodal bifurcation: a negative symmetric divergence coupling that induces barrier-driven co-adaptation and can favor a modality gap under conditional heterogeneity (§ 4); and (iv) empirical validation of the predicted signatures, including measurement of the divergence gap on MS-COCO (Lin et al., 2014) embeddings from pretrained CLIP model families (§ 5).

2. Preliminaries and Setup

We study unimodal and multimodal contrastive learning within a measure-theoretic framework, characterizing the geometry of learned representations directly on the embedding manifold. In this section, we establish the following setup for our subsequent theoretical analysis. For ease of reference, Tab. 1 summarizes the principal notations used throughout the paper.

Data, encoders, and induced representation laws. We model training data as samples from a probability measure over positive pairs. Let $\mathcal{P}(\mathcal{S})$ denote the set of probability measures on a measurable space \mathcal{S} . In the unimodal setting, $r_{\text{um}} \in \mathcal{P}(\mathcal{X} \times \mathcal{X})$ governs pairs $(\mathbf{x}, \tilde{\mathbf{x}})$, typically two views of the same underlying example; accordingly, the two \mathcal{X} -marginals of r_{um} coincide (and we

denote this common marginal by $p_{\mathbf{x}}$). In the multimodal setting, $r_{\text{mm}} \in \mathcal{P}(\mathcal{X} \times \mathcal{Y})$ governs pairs (\mathbf{x}, \mathbf{y}) , where \mathcal{X} and \mathcal{Y} are measurable sample spaces; we write $p_{\mathbf{x}}$ and $p_{\mathbf{y}}$ for the \mathcal{X} - and \mathcal{Y} -marginals of r_{mm} , respectively, which are distinct due to heterogeneity across modalities.

Encoders transport the data laws onto the embedding manifold. We consider two encoder families $\{f_{\theta}\}_{\theta \in \Theta}$ and $\{g_{\phi}\}_{\phi \in \Phi}$ with compact parameter spaces Θ and Φ . The encoders $f_{\theta} : \mathcal{X} \rightarrow \mathcal{Z}$ and $g_{\phi} : \mathcal{Y} \rightarrow \mathcal{Z}$ map observations into a common ambient representation space $\mathcal{Z} \subset \mathbb{R}^n$, with n as the representation dimensionality. We model \mathcal{Z} as a Riemannian manifold (e.g., \mathbb{S}^{n-1}) equipped with its volume measure μ . The population-level state variables are the pushforward laws on \mathcal{Z} and $\mathcal{Z} \times \mathcal{Z}$:

$$\begin{aligned} q_{\theta} &:= (f_{\theta})_{\#} p_{\mathbf{x}}, & q_{\phi} &:= (g_{\phi})_{\#} p_{\mathbf{y}}, \\ \pi_{\theta\theta} &:= (f_{\theta} \times f_{\theta})_{\#} r_{\text{um}}, & \pi_{\theta\phi} &:= (f_{\theta} \times g_{\phi})_{\#} r_{\text{mm}}. \end{aligned}$$

Here, q_{θ} and q_{ϕ} are encoded marginal laws, while $\pi_{\theta\theta}$ and $\pi_{\theta\phi}$ are the encoded positive-pair laws.

InfoNCE objectives in contrastive learning. We analyze the standard InfoNCE family parameterized with the standard exponential similarity kernel $\kappa_{\tau}(\mathbf{z}, \mathbf{w}) = \kappa_{\tau}(\mathbf{w}, \mathbf{z}) := \exp(s(\mathbf{z}, \mathbf{w})/\tau)$, where s is a similarity critic and $\tau > 0$ is the temperature. The canonical unimodal and multimodal learning objectives are defined as follows.

Unimodal objective. In unimodal contrastive learning, given a training batch \mathcal{B} composed of a positive pair $(\mathbf{x}, \tilde{\mathbf{x}}) \sim r_{\text{um}}$ and N negative samples $\{\mathbf{x}'_j\}_{j=1}^N \stackrel{i.i.d.}{\sim} p_{\mathbf{x}}$, the empirical InfoNCE loss is¹

$$\begin{aligned} \mathcal{L}_{\text{NCE}}(\theta) &:= \\ \mathbb{E}_{\mathcal{B}} \left[-\log \frac{\kappa_{\tau}(f_{\theta}(\mathbf{x}), f_{\theta}(\tilde{\mathbf{x}}))}{\kappa_{\tau}(f_{\theta}(\mathbf{x}), f_{\theta}(\tilde{\mathbf{x}})) + \sum_{j=1}^N \kappa_{\tau}(f_{\theta}(\mathbf{x}), f_{\theta}(\mathbf{x}'_j))} \right]. \end{aligned} \quad (1)$$

Symmetric multimodal objective. In multimodal contrastive learning, given a cross-modal positive pair $(\mathbf{x}, \mathbf{y}) \sim r_{\text{mm}}$ and N i.i.d. negatives $\{\mathbf{y}_i\}_{i=1}^N$ from the marginal $p_{\mathbf{y}}$, we form the directional batch $\mathcal{B}_{\mathbf{x} \rightarrow \mathbf{y}} := \{\mathbf{x}, \mathbf{y}, \mathbf{y}'_1, \dots, \mathbf{y}'_N\}$ with $\mathbf{y}'_j \stackrel{i.i.d.}{\sim} p_{\mathbf{y}}$, and define the directional \mathbf{x} to \mathbf{y} loss:

$$\begin{aligned} \mathcal{L}_{\text{NCE}}^{\mathbf{x} \rightarrow \mathbf{y}}(\theta, \phi) &:= \mathbb{E}_{\mathcal{B}_{\mathbf{x} \rightarrow \mathbf{y}}} \\ \left[-\log \frac{\kappa_{\tau}(f_{\theta}(\mathbf{x}), g_{\phi}(\mathbf{y}))}{\kappa_{\tau}(f_{\theta}(\mathbf{x}), g_{\phi}(\mathbf{y})) + \sum_{j=1}^N \kappa_{\tau}(f_{\theta}(\mathbf{x}), g_{\phi}(\mathbf{y}'_j))} \right], \end{aligned}$$

and analogously $\mathcal{L}_{\text{NCE}}^{\mathbf{y} \rightarrow \mathbf{x}}(\phi, \theta)$ by swapping modalities. The symmetric multimodal InfoNCE loss is

$$\mathcal{L}_{\text{Sym}}(\theta, \phi) := \frac{1}{2} (\mathcal{L}_{\text{NCE}}^{\mathbf{x} \rightarrow \mathbf{y}}(\theta, \phi) + \mathcal{L}_{\text{NCE}}^{\mathbf{y} \rightarrow \mathbf{x}}(\phi, \theta)). \quad (2)$$

¹We analyze an i.i.d. negative-sampling formulation. Although in-batch sampling introduces finite-sample dependencies, the two regimes converge to the same population limit as $N \rightarrow \infty$.

A population view of InfoNCE. We define the kernel-induced state variables that make the population geometry explicit. Under InfoNCE, the softmax denominator aggregates negative samples via the similarity kernel; at the population level, this induces a kernel-averaged field on \mathcal{Z} . To obtain a normalized smoothed density from this field, we first adopt the following constant-volume condition.

Assumption 2.1 (Constant kernel volume). The representation space \mathcal{Z} is compact with $\mu(\mathcal{Z}) < \infty$. For each $\tau > 0$, there exists $V_{\kappa}(\tau) \in (0, \infty)$ such that

$$\int_{\mathcal{Z}} \kappa_{\tau}(\mathbf{z}, \mathbf{w}) d\mu(\mathbf{w}) = V_{\kappa}(\tau), \quad \forall \mathbf{z} \in \mathcal{Z}.$$

Remark 2.1 (When Asm. 2.1 holds). A sufficient condition for Asm. 2.1 is that \mathcal{Z} is a compact homogeneous Riemannian manifold, μ is its invariant volume measure, and κ_{τ} is isotropic (i.e., depends only on the geodesic distance). Then invariance implies that $V_{\kappa}(\tau, \mathbf{z}) := \int \kappa_{\tau}(\mathbf{z}, \mathbf{w}) d\mu(\mathbf{w})$ is independent of \mathbf{z} , so Asm. 2.1 holds exactly. If $V_{\kappa}(\tau, \mathbf{z})$ is not constant, the definitions below extend by pointwise normalization. In that case, only results requiring uniform bounds additionally assume $\sup_{\mathbf{z}} V_{\kappa}(\tau, \mathbf{z}) / \inf_{\mathbf{z}} V_{\kappa}(\tau, \mathbf{z}) < \infty$.

Definition 2.1 (Population partition fields). Given a representation laws q_{θ} and q_{ϕ} , define the population *partition field* as $\Gamma_{\theta, \tau}(\mathbf{z}) := \int_{\mathcal{Z}} \kappa_{\tau}(\mathbf{z}, \mathbf{w}) dq_{\theta}(\mathbf{w})$ and $\Gamma_{\phi, \tau}(\mathbf{z}) := \int_{\mathcal{Z}} \kappa_{\tau}(\mathbf{z}, \mathbf{w}) dq_{\phi}(\mathbf{w})$.

If s is bounded above on $\mathcal{Z} \times \mathcal{Z}$, then $\Gamma_{\theta, \tau}$ is finite and well-defined for any probability measure q_{θ} .

Definition 2.2 (Kernel-smoothed representation density). Under Asm. 2.1, define the kernel-smoothed representation densities $\tilde{\rho}_{\theta, \tau}, \tilde{\rho}_{\phi, \tau} : \mathcal{Z} \rightarrow \mathbb{R}_{+}$ by

$$\tilde{\rho}_{\theta, \tau}(\mathbf{z}) := \Gamma_{\theta, \tau}(\mathbf{z}) / V_{\kappa}(\tau), \quad \tilde{\rho}_{\phi, \tau}(\mathbf{z}) := \Gamma_{\phi, \tau}(\mathbf{z}) / V_{\kappa}(\tau).$$

Equivalently, $\tilde{\rho}_{\theta, \tau} d\mu$ and $\tilde{\rho}_{\phi, \tau} d\mu$ are kernel-smoothed representation measures on \mathcal{Z} .

Remark 2.2 (Finite- τ smoothing and positivity). For any $\tau > 0$, $\tilde{\rho}_{\theta, \tau}$ is a kernel-smoothing of q_{θ} via $\Gamma_{\theta, \tau}$. In particular, $\tilde{\rho}_{\theta, \tau}$ is well-defined as a μ -density (i.e., $\int \tilde{\rho}_{\theta, \tau}(\mathbf{z}) d\mu(\mathbf{z}) = 1$) even when q_{θ} is singular w.r.t. μ . Moreover, if $\kappa_{\tau}(\mathbf{z}, \mathbf{w})$ is continuous and strictly positive on $\mathcal{Z} \times \mathcal{Z}$, then $\tilde{\rho}_{\theta, \tau}$ is continuous and strictly positive on \mathcal{Z} (and similarly for $\tilde{\rho}_{\phi, \tau}$).

From a geometric perspective, $\Gamma_{\theta, \tau}(\mathbf{z})$ is the population softmax normalizer for a query at \mathbf{z} , and $\tilde{\rho}_{\theta, \tau}$ is the kernel-smoothed density of q_{θ} evaluated at scale τ . These quantities provide a natural bridge between the discrete empirical objective and the continuous population geometry: the InfoNCE denominator functions as a Monte Carlo estimator for $\Gamma_{\theta, \tau}$ (and symmetrically, $\Gamma_{\phi, \tau}$), while the continuous optimization dynamics are steered by the induced smoothed densities $\tilde{\rho}_{\theta, \tau}$ and $\tilde{\rho}_{\phi, \tau}$.

3. Unimodal InfoNCE: A Convex Landscape

This section develops the unimodal baseline that will later expose the multimodal bifurcation. Our first goal is dynamic: show that large-batch InfoNCE follows gradient descent on an explicit deterministic energy that depends on θ only through the induced laws $(q_\theta, \pi_{\theta\theta})$ on \mathcal{Z} and $\mathcal{Z} \times \mathcal{Z}$. All proofs for this section are provided in App. D.

3.1. Asymptotic Deterministic Energy

We ask: what population-level object does unimodal InfoNCE optimize when the batch size is large? The answer is a closed-form parametric energy $\mathcal{J}_\tau(\theta)$ whose gradient matches the InfoNCE gradient up to vanishing error as the batch size $N \rightarrow \infty$.

Assumption 3.1 (Optimization regularity). Assume the following conditions hold uniformly over the compact parameter space Θ :

(i) (Encoder regularity). For every $\mathbf{x} \in \mathcal{X}$, the map $\theta \mapsto f_\theta(\mathbf{x})$ is C^1 on Θ , and its parameter Jacobian is uniformly bounded: $\sup_{\theta \in \Theta} \sup_{\mathbf{x} \in \mathcal{X}} \|J_\theta f_\theta(\mathbf{x})\| < \infty$.²

(ii) (Critic regularity). The critic s is C^1 on an open neighborhood of $\mathcal{Z} \times \mathcal{Z}$, and its input gradient is uniformly bounded on $\mathcal{Z} \times \mathcal{Z}$: $\sup_{(\mathbf{z}, \mathbf{w}) \in \mathcal{Z} \times \mathcal{Z}} \|\nabla s(\mathbf{z}, \mathbf{w})\| < \infty$.

Remark 3.1 (Optimization stability). These conditions are necessary to preclude gradient explosion within the softmax, ensuring stable dynamics. Under Asm. 3.1, the InfoNCE gradient admits a uniform bound over the parameter space Θ . This property is structurally required to justify the exchange of the large-batch limit and differentiation for later analysis. Further interpretations and the formal uniform bounds are provided in App. B.1 and Lem. C.1, respectively.

We now isolate the population object estimated by the empirical softmax denominator. The key is that, for fixed τ , the negative-sample average concentrates around the population partition field $\Gamma_{\theta, \tau}$ (Def. 2.1), yielding both value- and gradient-level consistency.

Definition 3.1 (Alignment potential field). Let $\pi_{\theta\theta} \in \mathcal{P}(\mathcal{Z} \times \mathcal{Z})$ be the encoded positive-pair law with first marginal $q_\theta \in \mathcal{P}(\mathcal{Z})$. By disintegration, there exists a measurable family of probability measures $\{\nu_{\theta, \mathbf{z}}\}_{\mathbf{z} \in \mathcal{Z}} \subset \mathcal{P}(\mathcal{Z})$ such that $d\pi_{\theta\theta}(\mathbf{z}, \mathbf{w}) = dq_\theta(\mathbf{z}) d\nu_{\theta, \mathbf{z}}(\mathbf{w})$, as measures on $\mathcal{Z} \times \mathcal{Z}$. Define the alignment potential field $U_\theta(\mathbf{z})$ by

$$U_\theta(\mathbf{z}) := - \int_{\mathcal{Z}} s(\mathbf{z}, \mathbf{w}) d\nu_{\theta, \mathbf{z}}(\mathbf{w}), \quad \text{for } q_\theta\text{-a.e. } \mathbf{z}.$$

Definition 3.2 (Unimodal parametric energy). Fix $\tau > 0$. Let $\tilde{\rho}_{\theta, \tau}$ be the kernel-smoothed μ -density from Def. 2.2,

²Throughout this paper, $\|\cdot\|$ denotes the ℓ_2 norm for vectors unless otherwise specified.

and let U_θ be the alignment potential defined in Def. 3.1. Define the unimodal parametric energy $\mathcal{J}_\tau : \Theta \rightarrow \mathbb{R}$ as

$$\mathcal{J}_\tau(\theta) := \frac{1}{\tau} \int_{\mathcal{Z}} U_\theta(\mathbf{z}) dq_\theta(\mathbf{z}) - H_\times(q_\theta, \tilde{\rho}_{\theta, \tau}), \quad (3)$$

where $H_\times(q, \tilde{\rho}) := - \int_{\mathcal{Z}} \log \tilde{\rho}(\mathbf{z}) dq(\mathbf{z})$ is the cross-entropy of a measure $q \in \mathcal{P}(\mathcal{Z})$ against a positive density $\tilde{\rho}$.

Theorem 3.1 (Large-batch unimodal dynamics). *Consider the unimodal InfoNCE objective $\mathcal{L}_{\text{NCE}}(\theta)$ in Eq. (1) and the parametric energy $\mathcal{J}_\tau(\theta)$ in Def. 3.2. Assume Asms. 2.1 and 3.1. Then, for any fixed $\tau > 0$ and $\theta \in \Theta$, as $N \rightarrow \infty$:*

$$\begin{aligned} |\mathcal{L}_{\text{NCE}}(\theta) - \mathcal{J}_\tau(\theta) - \log(NV_\kappa(\tau))| &\rightarrow 0, \\ \|\nabla_\theta \mathcal{L}_{\text{NCE}}(\theta) - \nabla_\theta \mathcal{J}_\tau(\theta)\| &\rightarrow 0. \end{aligned} \quad (4)$$

Interpretation. Thm. 3.1 establishes that for sufficiently large N , gradient descent on \mathcal{L}_{NCE} closely tracks that of \mathcal{J}_τ , governed by the partition field $\Gamma_{\theta, \tau}$ (equivalently the kernel-smoothed density $\tilde{\rho}_{\theta, \tau}$).

3.2. Intrinsic Free Energy and Gibbs Equilibrium

Definition 3.3 (Intrinsic unimodal energy). Fix $\tau > 0$ and a Borel measurable potential $U : \mathcal{Z} \rightarrow \mathbb{R}$. Let $\mathcal{P}_\mu(\mathcal{Z})$ denote the set of μ -densities on \mathcal{Z} . We define the intrinsic unimodal energy $\mathcal{F}_{\tau, U} : \mathcal{P}_\mu(\mathcal{Z}) \rightarrow (-\infty, +\infty]$ by

$$\mathcal{F}_{\tau, U}(\rho) := \frac{1}{\tau} \int_{\mathcal{Z}} U(\mathbf{z}) \rho(\mathbf{z}) d\mu(\mathbf{z}) - H(\rho), \quad (5)$$

where $H(\rho) := - \int_{\mathcal{Z}} \rho(\mathbf{z}) \log \rho(\mathbf{z}) d\mu(\mathbf{z})$ is the differential entropy, with the convention that $0 \log 0 := 0$ and $\mathcal{F}_{\tau, U}(\rho) = +\infty$ if either integral is $+\infty$.

Proposition 3.1 (Unique Gibbs equilibrium). *Assume \mathcal{Z} is compact with $\mu(\mathcal{Z}) < \infty$. Fix $\tau > 0$ and let $U : \mathcal{Z} \rightarrow \mathbb{R}$ be measurable and bounded below μ -a.e. Then, $\mathcal{F}_{\tau, U}$ (Eq. (5)) is strictly convex on $\mathcal{P}_\mu(\mathcal{Z})$ and admits a unique minimizer*

$$\rho^*(\mathbf{z}) = \frac{\exp(-U(\mathbf{z})/\tau)}{Z_\tau}, \quad Z_\tau := \int_{\mathcal{Z}} \exp(-U(\mathbf{z})/\tau) d\mu(\mathbf{z}).$$

Proposition 3.2 (Low-temperature concentration). *In the setting of Prop. 3.1, fix $\sigma > 0$ and define*

$$\mathcal{W}^\sigma := \{\mathbf{z} \in \mathcal{Z} : U(\mathbf{z}) \leq \text{ess inf}_\mu U + \sigma\}.$$

Then as $\tau \rightarrow 0^+$, the Gibbs measure $\rho^(\mathbf{z}) d\mu(\mathbf{z})$ concentrates on \mathcal{W}^σ in the sense that, for every open $\mathcal{O} \supset \mathcal{W}^\sigma$, $\rho^* \mu(\mathcal{Z} \setminus \mathcal{O}) \rightarrow 0$.*

Interpretation. In unimodal contrastive learning, the intrinsic landscape has a *single* equilibrium for each τ , and small τ forces mass into near-minimizers of the alignment potential field U . Specifically, Prop. 3.2 predicts monotone concentration onto near-minimizers as τ decreases. Fig. 2a quantifies this by plotting the equilibrium mass inside a fixed sublevel region versus the temperature τ .

Connecting back to \mathcal{J}_τ : sharp kernels control KDE bias.

To transfer this intrinsic geometry back to the parametric energy, we use a sharp-kernel regime where the kernel-smoothed density $\tilde{\rho}_{\theta,\tau}$ approximates the true density ρ_θ of induced representation under the parameterization of θ .

Assumption 3.2 (Sharp diagonal peak). Assume Asm. 2.1. Let $d_{\mathcal{Z}}(\cdot, \cdot)$ denote the geodesic distance on \mathcal{Z} . There exist constants $r > 0$ and $0 < m_1 \leq m_2 < \infty$ such that for all $\mathbf{z} \in \mathcal{Z}$ and all $\mathbf{w} \in \{\mathbf{w} \in \mathcal{Z} : d_{\mathcal{Z}}(\mathbf{z}, \mathbf{w}) < r\}$,

$$-m_2 d_{\mathcal{Z}}(\mathbf{z}, \mathbf{w})^2 \leq s(\mathbf{z}, \mathbf{w}) - s(\mathbf{z}, \mathbf{z}) \leq -m_1 d_{\mathcal{Z}}(\mathbf{z}, \mathbf{w})^2, \quad (6)$$

and the similarity peaks strictly at the identity such that $\arg \max_{\mathbf{w} \in \mathcal{Z}} s(\mathbf{z}, \mathbf{w}) = \mathbf{z}$ for each $\mathbf{z} \in \mathcal{Z}$.

Remark 3.2. Geometrically, Asm. 3.2 forces the normalized kernel mass to concentrate within an $O(\sqrt{\tau})$ geodesic neighborhood of the diagonal (see App. B.2 for a detailed geometric interpretation). This implies that $\tilde{\rho}_{\theta,\tau}$ is effectively a local smoothing of ρ_θ , which we characterize for the low-temperature regime in Lem. C.3 (see App. C.2).

Theorem 3.2 (Low-temperature unimodal energy consistency). Assume Asms. 2.1, 3.1 and 3.2. Fix $\theta \in \Theta$ and assume $q_\theta \ll \mu$ with a strictly positive, continuous density ρ_θ , i.e., $\inf_{\mathbf{z} \in \mathcal{Z}} \rho_\theta(\mathbf{z}) \geq \underline{\rho}_\theta > 0$.³ Define the KDE mismatch $\varepsilon_{\text{kde}}^{(\theta)}(\tau) := \|\tilde{\rho}_{\theta,\tau} - \rho_\theta\|_\infty$. Then, $\exists \tau_0(\theta) > 0$ such that

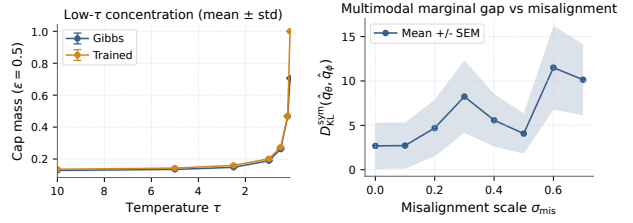
$$|\mathcal{J}_\tau(\theta) - \mathcal{F}_{\tau, U_\theta}(\rho_\theta)| \leq 2\varepsilon_{\text{kde}}^{(\theta)}(\tau)/\underline{\rho}_\theta, \quad \forall 0 < \tau \leq \tau_0(\theta),$$

and in particular $|\mathcal{J}_\tau(\theta) - \mathcal{F}_{\tau, U_\theta}(\rho_\theta)| \rightarrow 0$, as $\tau \rightarrow 0^+$.

Uniformity as an intrinsic tie-breaker. Thm. 3.2 provides the bridge back to training: in the sharp-kernel regime, the parametric energy $\mathcal{J}_\tau(\theta)$ is close to $\mathcal{F}_{\tau, U_\theta}(\rho_\theta)$ up to the KDE mismatch between $\tilde{\rho}_{\theta,\tau}$ and ρ_θ . Consequently, if the encoder family is sufficiently expressive to *realize* the intrinsic Gibbs equilibrium associated with the best attainable potential level within the family, then minimizers of \mathcal{J}_τ inherit the same ground-state concentration behavior predicted by $\mathcal{F}_{\tau, U_\theta}$. Within that aligned basin where U_θ is already near-minimized, the remaining degree of freedom is how mass is arranged, and the entropy term in Eq. (5) selects the most internally dispersed configuration among near-optimal solutions; this is the sense in which ‘‘uniformity’’ emerges. Cor. C.1 formalizes the expressivity condition and establishes the parametric inheritance of the ground state (see App. C.3 for details).

Punchline 1 (Unimodal InfoNCE mechanism). The defining feature of unimodal contrastive learning is its structural cohesion. Because the modality evaluates its cross-entropy against its *own* smoothed density field, the

³See App. B.3 for a detailed discussion on the strict positivity assumption and the role of density floors.



(a) Unimodal concentration. (b) Multimodal marginal gap.

Figure 2. Numerical illustration of the geometric bifurcation. (a) In the unimodal intrinsic problem, the energy is Gibbs-like and concentrates toward low-potential regions as $\tau \downarrow$. (b) In the multimodal setting, cross-modal coupling induces persistent marginal separation, whose magnitude grows with latent misalignment.

intrinsic energy is strictly convex. Alignment dictates the ground-state basin, while entropy provides a unique, uniformly dispersed equilibrium within it.

4. Multimodal InfoNCE: Divergence Coupling

We analyze the symmetric multimodal InfoNCE objective used in CLIP-style training (Eq. (2)). Unlike the unimodal setting, the geometry is *cross-coupled*: each modality induces the effective field seen by the other. This coupling yields qualitatively different landscapes and permits population-level modality gaps. All proofs for the formal statements in this section are provided in App. E.

4.1. Cross-Coupled Multimodal Deterministic Energy

We ask the multimodal analogue of § 3: what deterministic population objective does symmetric InfoNCE optimize at large batch size? As in the unimodal case, the answer is a closed-form parametric energy whose gradient matches the stochastic loss gradient as $N \rightarrow \infty$. The key difference is *coupling*: each modality’s cross-entropy is taken against the other modality’s kernel-smoothed density field.

Assumption 4.1 (Multimodal optimization regularity). In multimodal contrastive learning, assume Asm. 3.1 holds for both encoder families $\{f_\theta\}_{\theta \in \Theta}$ and $\{g_\phi\}_{\phi \in \Phi}$, uniformly over the joint parameter space $\Theta \times \Phi$.

Remark 4.1. Under Asm. 4.1, the symmetric InfoNCE objective has a uniformly bounded joint gradient over $\Theta \times \Phi$, which permits exchanging differentiation with the large-batch limit in the multimodal consistency proof. See Lem. C.2 for the uniform gradient bounds.

Definition 4.1 (Directional alignment potential fields). Let $\pi_{\theta\phi}$ denote the encoded positive-pair law on $\mathcal{Z} \times \mathcal{Z}$ with marginals q_θ and q_ϕ . By disintegration, there exist measurable families of probability measures $\{\nu_{\theta\phi,\mathbf{z}}\}_{\mathbf{z} \in \mathcal{Z}}$ and $\{\nu_{\theta\phi,\mathbf{w}}\}_{\mathbf{w} \in \mathcal{Z}}$ such that $d\pi_{\theta\phi}(\mathbf{z}, \mathbf{w}) = dq_\theta(\mathbf{z}) d\nu_{\theta\phi,\mathbf{z}}(\mathbf{w}) = dq_\phi(\mathbf{w}) d\nu_{\theta\phi,\mathbf{w}}(\mathbf{z})$, as measures on $\mathcal{Z} \times \mathcal{Z}$. Define the di-

rectional alignment potential fields

$$\begin{aligned} U_{\theta \rightarrow \phi}(\mathbf{z}) &:= - \int_{\mathcal{Z}} s(\mathbf{z}, \mathbf{w}) \, d\nu_{\theta\phi, \mathbf{z}}(\mathbf{w}), \quad q_\theta\text{-a.e. } \mathbf{z}, \\ U_{\phi \rightarrow \theta}(\mathbf{w}) &:= - \int_{\mathcal{Z}} s(\mathbf{z}, \mathbf{w}) \, d\nu_{\phi\theta, \mathbf{w}}(\mathbf{z}), \quad q_\phi\text{-a.e. } \mathbf{w}. \end{aligned}$$

Definition 4.2 (Symmetric multimodal parametric energy).

Fix $\tau > 0$. Recall the kernel-smoothed densities $\tilde{\rho}_{\theta, \tau}, \tilde{\rho}_{\phi, \tau}$ from Def. 2.2. Define the directional multimodal energies

$$\begin{aligned} \mathcal{J}_\tau^{x \rightarrow y}(\theta, \phi) &:= \frac{1}{\tau} \int_{\mathcal{Z}} U_{\theta \rightarrow \phi} \, dq_\theta - H_{\times}(q_\theta, \tilde{\rho}_{\phi, \tau}), \\ \mathcal{J}_\tau^{y \rightarrow x}(\theta, \phi) &:= \frac{1}{\tau} \int_{\mathcal{Z}} U_{\phi \rightarrow \theta} \, dq_\phi - H_{\times}(q_\phi, \tilde{\rho}_{\theta, \tau}), \end{aligned}$$

and the symmetric multimodal parametric energy

$$\mathcal{J}_\tau^{\text{Sym}}(\theta, \phi) := \frac{1}{2} (\mathcal{J}_\tau^{x \rightarrow y}(\theta, \phi) + \mathcal{J}_\tau^{y \rightarrow x}(\theta, \phi)). \quad (7)$$

Here, $U_{\theta \rightarrow \phi}$ and $U_{\phi \rightarrow \theta}$ are the θ to ϕ and ϕ to θ directional alignment potential fields from Def. 4.1.

Remark 4.2 (Directional asymmetry is generic). Although both directions are induced by the same pair law $\pi_{\theta\phi}$, the two regular conditional laws $\nu_{\theta\phi, \mathbf{z}}$ and $\nu_{\phi\theta, \mathbf{w}}$ need not coincide. Consequently, $U_{\theta \rightarrow \phi}$ and $U_{\phi \rightarrow \theta}$ are generally distinct: there is no single unimodal-style potential field governing both modalities unless one imposes an additional compatibility condition on the conditional laws.

Theorem 4.1 (Large-batch multimodal dynamics). Consider the multimodal loss $\mathcal{L}_{\text{Sym}}(\theta, \phi)$ in Eq. (2) and the energy $\mathcal{J}_\tau^{\text{Sym}}(\theta, \phi)$ in Def. 4.2. Assume Asms. 2.1 and 4.1. Then, for any fixed $\tau > 0$ and $(\theta, \phi) \in \Theta \times \Phi$, as $N \rightarrow \infty$,

$$\begin{aligned} |\mathcal{L}_{\text{Sym}}(\theta, \phi) - \mathcal{J}_\tau^{\text{Sym}}(\theta, \phi) - \log(NV_\kappa(\tau))| &\rightarrow 0, \\ \|\nabla_{(\theta, \phi)} \mathcal{L}_{\text{Sym}}(\theta, \phi) - \nabla_{(\theta, \phi)} \mathcal{J}_\tau^{\text{Sym}}(\theta, \phi)\| &\rightarrow 0. \end{aligned}$$

Interpretation. The additive term $\log(NV_\kappa(\tau))$ is constant in (θ, ϕ) . Thus, in the large-batch regime, symmetric InfoNCE training tracks gradient on $\mathcal{J}_\tau^{\text{Sym}}$ up to vanishing error. Unlike the unimodal parametric energy, $\mathcal{J}_\tau^{\text{Sym}}$ is intrinsically *cross-coupled*: each modality's cross-entropy term is evaluated against the other's smoothed density.

4.2. Divergence and Barrier-Driven Co-Adaptation

To interpret the coupled parametric energy $\mathcal{J}_\tau^{\text{Sym}}$, we lift it to an intrinsic functional over modality *densities* on \mathcal{Z} . The key difference from the unimodal free energy is a *negative* symmetric divergence coupling, which persists at fixed τ and qualitatively changes the coordinate-wise geometry.

Definition 4.3 (Intrinsic multimodal energy). Fix $\tau > 0$ and Borel measurable potentials $U_{1+2}, U_{2+1} : \mathcal{Z} \rightarrow \mathbb{R}$. Fix

a density floor $\underline{\rho} > 0$ with $\underline{\rho}\mu(\mathcal{Z}) < 1$ and denote the set of strictly positive densities as

$$\mathcal{P}_{\mu, \underline{\rho}}(\mathcal{Z}) := \left\{ \rho \in L^1(\mathcal{Z}) : \rho \geq \underline{\rho} \mu\text{-a.e.}, \int_{\mathcal{Z}} \rho \, d\mu = 1 \right\}.$$

For $(\rho_1, \rho_2) \in \mathcal{P}_{\mu, \underline{\rho}}(\mathcal{Z}) \times \mathcal{P}_{\mu, \underline{\rho}}(\mathcal{Z})$, define the intrinsic multimodal energy by

$$\begin{aligned} \mathcal{F}_{\tau, \mathbf{U}_{1,2}}^{\text{Sym}}(\rho_1, \rho_2) &:= \frac{1}{2} (\mathcal{F}_{\tau, U_{1+2}}(\rho_1) + \mathcal{F}_{\tau, U_{2+1}}(\rho_2)) \\ &\quad - D_{\text{KL}}^{\text{Sym}}(\rho_1, \rho_2), \end{aligned} \quad (8)$$

where $\mathbf{U}_{1,2} := (U_{1+2}, U_{2+1})$, $\mathcal{F}_{\tau, U_{1+2}}$ and $\mathcal{F}_{\tau, U_{2+1}}$ are the unimodal free energies (Eq. (5)), and the symmetric KL divergence $D_{\text{KL}}^{\text{Sym}}(\rho_1, \rho_2) := \frac{1}{2} (D_{\text{KL}}(\rho_1 \parallel \rho_2) + D_{\text{KL}}(\rho_2 \parallel \rho_1))$ with $D_{\text{KL}}(\rho_1 \parallel \rho_2) := \int_{\mathcal{Z}} \rho_1 \log(\rho_1 / \rho_2) \, d\mu$.

Remark 4.3. The constraint $\rho_i \geq \underline{\rho}$ is a technical device that rules out degenerate $-\infty$ energies and makes the best-response geometry explicit. See App. B.3 for a discussion.

Proposition 4.1 (Barrier best response and extremal collapse). Assume \mathcal{Z} is compact with $\mu(\mathcal{Z}) < \infty$, and let $\mathcal{F}_{\tau, \mathbf{U}_{1,2}}^{\text{Sym}}$ be as in Def. 4.3. Fix $\rho_2 \in \mathcal{P}_{\mu, \underline{\rho}}(\mathcal{Z})$ and define the effective potential field by $V_{1|2}(\mathbf{z}) := \frac{1}{\tau} U_{1+2}(\mathbf{z}) + \log \rho_2(\mathbf{z})$. Then, the coordinate map $\rho_1 \mapsto \mathcal{F}_{\tau, \mathbf{U}_{1,2}}^{\text{Sym}}(\rho_1, \rho_2)$ is concave on $\mathcal{P}_{\mu, \underline{\rho}}(\mathcal{Z})$, and its infimum is approached by sequences that concentrate the excess mass $M_{\text{ex}} := 1 - \underline{\rho}\mu(\mathcal{Z})$ onto approximate minimizers of $V_{1|2}$, leaving only the floor $\underline{\rho}$ elsewhere. Formally, for a sufficiently small $\sigma > 0$, let $\mathcal{W}_1^\sigma := \{\mathbf{z} \in \mathcal{Z} : V_{1|2}(\mathbf{z}) \leq \text{ess inf}_\mu V_{1|2} + \sigma\}$ be the sublevel set. Define the σ -approximate density $\rho_1^{(\sigma)}$ by concentrating the excess mass on a shrinking set $\mathcal{S}_1^\sigma \subseteq \mathcal{W}_1^\sigma$:⁴

$$\rho_1^{(\sigma)}(\mathbf{z}) = \underline{\rho} + \mathbb{1}_{\mathcal{S}_1^\sigma}(\mathbf{z}) \cdot M_{\text{ex}} / \mu(\mathcal{S}_1^\sigma), \quad \lim_{\sigma \rightarrow 0} \mu(\mathcal{S}_1^\sigma) = 0. \quad (9)$$

As $\sigma \rightarrow 0$, the energy of $\rho_1^{(\sigma)}$ converges to the infimum:

$$\lim_{\sigma \rightarrow 0} \mathcal{F}_{\tau, \mathbf{U}_{1,2}}^{\text{Sym}}(\rho_1^{(\sigma)}, \rho_2) = \inf_{\rho_1 \in \mathcal{P}_+(\mathcal{Z})} \mathcal{F}_{\tau, \mathbf{U}_{1,2}}^{\text{Sym}}(\rho_1, \rho_2). \quad (10)$$

An analogous statement holds when optimizing in ρ_2 with ρ_1 fixed, with respect to the dual effective potential field $V_{2|1}(\mathbf{z}) := \frac{1}{\tau} U_{2+1}(\mathbf{z}) + \log \rho_1(\mathbf{z})$.

Theorem 4.2 (Low-temperature multimodal energy consistency). Assume Asms. 2.1, 3.2 and 4.1. Fix any $(\theta, \phi) \in \Theta \times \Phi$, and assume $q_\theta \ll \mu$, $q_\phi \ll \mu$ with continuous densities ρ_θ, ρ_ϕ bounded below: $\inf_{\mathbf{z} \in \mathcal{Z}} \rho_\theta(\mathbf{z}) \geq \underline{\rho}_\theta > 0$ and $\inf_{\mathbf{z} \in \mathcal{Z}} \rho_\phi(\mathbf{z}) \geq \underline{\rho}_\phi > 0$. Let $\varepsilon_{\text{kde}}^{(\theta)}(\tau) := \|\tilde{\rho}_{\theta, \tau} - \rho_\theta\|_\infty$ and $\varepsilon_{\text{kde}}^{(\phi)}(\tau) := \|\tilde{\rho}_{\phi, \tau} - \rho_\phi\|_\infty$. Then there exists $\tau_0(\theta, \phi) > 0$

⁴Typically, $\mathcal{S}_1^\sigma = \mathcal{W}_1^\sigma$ for sharp minima, or any vanishing subset $\mathcal{S}_1^\sigma \subset \mathcal{W}_1^\sigma$ for flat minima.

such that for all $0 < \tau \leq \tau_0(\theta, \phi)$,

$$\left| \mathcal{J}_\tau^{\text{Sym}}(\theta, \phi) - \mathcal{F}_{\tau, \mathbf{U}_{\theta, \phi}}^{\text{Sym}}(\rho_\theta, \rho_\phi) \right| \leq \frac{(\varepsilon_{\text{kde}}^{(\theta)}(\tau) + \varepsilon_{\text{kde}}^{(\phi)}(\tau))}{\min\{\rho_\theta, \rho_\phi\}}.$$

Moreover, as $\tau \rightarrow 0^+$, $|\mathcal{J}_\tau^{\text{Sym}}(\theta, \phi) - \mathcal{F}_{\tau, \mathbf{U}_{\theta, \phi}}^{\text{Sym}}(\rho_\theta, \rho_\phi)| \rightarrow 0$. Here, $\mathcal{F}_{\tau, \mathbf{U}_{\theta, \phi}}^{\text{Sym}}(\rho_\theta, \rho_\phi)$ is the intrinsic multimodal energy (Def. 4.3) evaluated at the densities q_θ, q_ϕ and the directional potential fields $\mathbf{U}_{\theta, \phi} := (U_{\theta \rightarrow \phi}, U_{\phi \rightarrow \theta})$.

Remark 4.4 (Negative divergence persists). The limit $\tau \rightarrow 0^+$ only controls the KDE bias (driving $\tilde{\rho}_{\cdot, \tau} \rightarrow \rho_\cdot$); it does not affect the divergence $D_{\text{KL}}^{\text{Sym}}(\rho_\theta, \rho_\phi)$. As it enters Def. 4.3 with a negative sign, the intrinsic landscape rewards separation rather than matching, even in the sharp-kernel regime. Fig. 2b illustrates this persistent repulsion by estimating the symmetric KL divergence of the induced distributions under varying scales of cross-modal misalignment.

Parametric inheritance under model expressivity. Combining Thm. 4.2 with the barrier best-response geometry in Prop. 4.1, one obtains a parametric inheritance statement: under a model expressivity condition, minimizers of the practical energy $\mathcal{J}_\tau^{\text{Sym}}$ concentrate their excess mass near minimizers of the effective barrier potentials $V_{\theta|\phi}$ and $V_{\phi|\theta}$. Cor. C.2 formalizes the model expressivity condition and establishes the parametric inheritance (see App. C.4).

Punchline 2 (Multimodal InfoNCE mechanism). Symmetric multimodal InfoNCE is pairwise attractive yet populationally repulsive. While individual cross-modal pairs align, the cross-coupled geometry can make each modality’s marginal distribution act as a repulsive *population barrier* against the other. This structurally enforced drive for macroscopic separation reveals the modality gap as a natural geometric consequence in the analyzed regime.

5. Empirical Validation

We validate the theoretical picture at two complementary levels. First, in controlled numerical experiments, we isolate the three core mechanisms predicted by the analysis: large-batch gradient consistency, the Gibbs-type intrinsic equilibrium in the unimodal regime, and the emergence of a structural modality gap under controlled cross-modal misalignment. Second, on MS-COCO (Lin et al., 2014), we examine whether the same geometric signatures appear in realistic CLIP-like representations: whether strong pre-trained models still exhibit a measurable modality gap, and whether weakening image–text compatibility enlarges that gap in a systematic way.

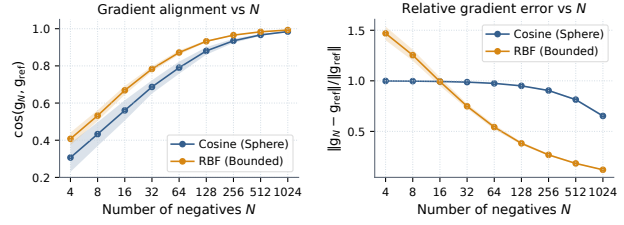


Figure 3. Large-batch gradient consistency across critics. Finite-batch InfoNCE gradients are compared against a high-fidelity large-batch reference as the number of negatives N increases. Left: gradient alignment with the reference (\uparrow). Right: relative gradient error (\downarrow). Results are shown for both the cosine critic in the spherical regime and the RBF critic in the compact Euclidean regime, with mean \pm std over 20 seeds.

5.1. Numerical Validation

Large-batch gradient consistency. We first validate the asymptotic consistency established in Thm. 3.1. Using a synthetic Gaussian-mixture dataset, we compare finite-batch InfoNCE gradients against a high-fidelity large-batch reference under two regimes: a spherical regime with feature normalization and cosine similarity, and a compact Euclidean regime with an RBF critic. For each seed, we fix a batch of anchors/positives together with a large reference pool of negatives, and sweep the number of negatives $N \in \{4, 8, 16, 32, 64, 128, 256, 512, 1024\}$. We then evaluate the batch gradient using two complementary diagnostics: *gradient alignment*, which measures directional agreement with the large-batch reference, and *relative error*, which measures the magnitude deviation.

As shown in Fig. 3, the agreement improves monotonically with N in both regimes: gradient alignment increases, while relative error decreases toward zero. This is exactly the behavior predicted by the theory. As the empirical softmax denominator concentrates around its population counterpart, the stochastic InfoNCE gradient approaches the deterministic energy gradient. The convergence is already strong at moderate N , indicating that the large-batch energy is not merely an asymptotic idealization, but a practically faithful proxy for training dynamics. Since the symmetric multimodal objective in Eq. (2) is the sum of two directional terms, the same consistency mechanism carries over componentwise to the multimodal setting. Full setup details are deferred to App. F.1.

Unimodal equilibrium and low- τ concentration. We next test the intrinsic unimodal picture in § 3. For a fixed alignment potential field U , the free-energy functional $\mathcal{F}_{\tau, U}$ should admit a unique Gibbs equilibrium, and this equilibrium should concentrate near the minimizers of U as $\tau \rightarrow 0$. To verify this, we construct a smooth two-well potential on \mathbb{S}^2 , optimize a particle-based surrogate of $\mathcal{F}_{\tau, U}$, and com-

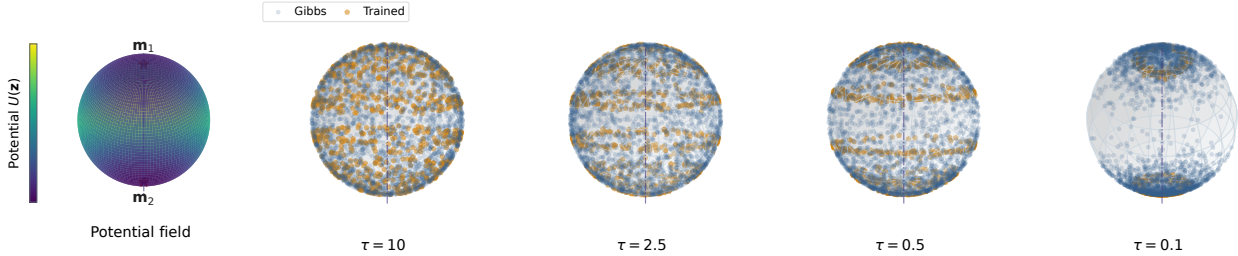


Figure 4. Unimodal potential landscape on S^2 and equilibria across temperature. Left: the two-well potential U , with minima centers m_1 and m_2 marked. Right: Gibbs samples (blue) and trained particles (orange) for several temperatures τ . At high temperature, both distributions remain diffuse due to the stronger role of entropy; as τ decreases, both concentrate around the low-energy wells.

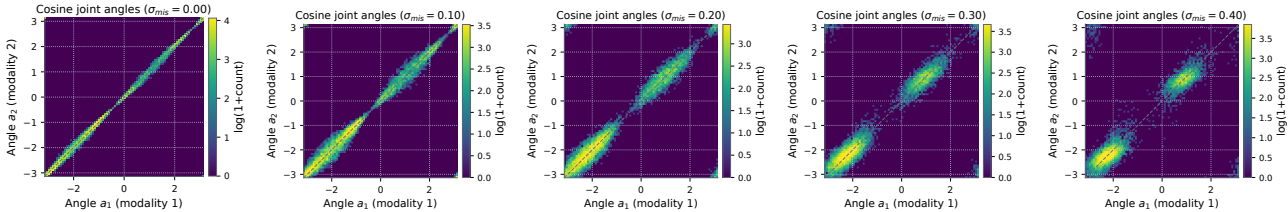


Figure 5. Joint-angle coupling under controlled misalignment. Each panel shows a histogram of (a_1, a_2) for $\sigma_{\text{mis}} \in \{0.0, 0.1, 0.2, 0.3, 0.4\}$. When $\sigma_{\text{mis}} = 0$, the learned coupling is sharply concentrated near the diagonal, indicating a small modality gap. As $\sigma_{\text{mis}} \uparrow$, the diagonal band broadens and deforms, revealing a noisier cross-modal coupling while preserving the coarse latent modes.

pare the resulting particle distribution against the Gibbs law $\rho_\tau^* \propto \exp(-U/\tau)$ across a range of temperatures.

The qualitative agreement is shown in Fig. 4: at high temperature, both the Gibbs samples and the trained particles remain broadly spread over the sphere, reflecting the stronger role of entropy; as τ decreases, both progressively concentrate around the low-energy wells. The quantitative trend is summarized by the cap-mass statistic in Fig. 2a, which measures the mass inside fixed geodesic neighborhoods around the two minima. For both the Gibbs baseline and the trained particle system, this mass increases monotonically as τ decreases, confirming the low-temperature concentration predicted by the intrinsic theory. The trained particles exhibit some semi-regular local packing, induced by the KDE-based entropy surrogate, but this microscopic structure does not alter the macroscopic prediction: the learned equilibrium still follows the Gibbs-type concentration trend. Further details are deferred to App. F.2.

Structural modality gap under controlled misalignment.

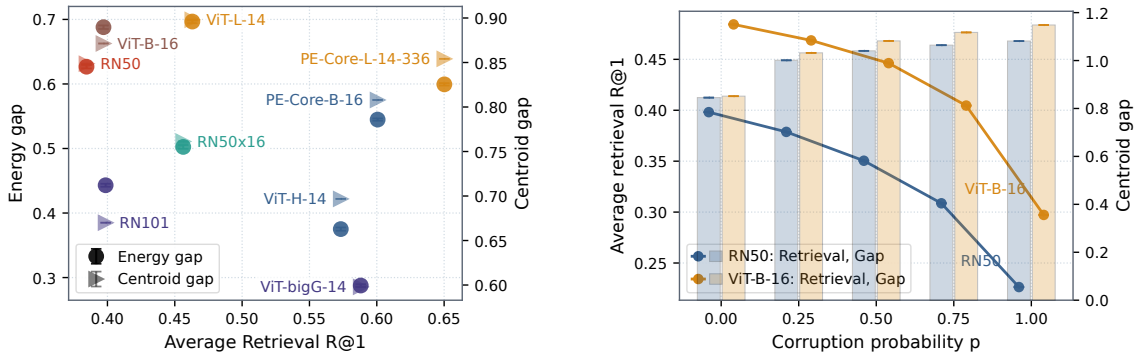
We then test the central multimodal mechanism of § 4: once the two modalities induce heterogeneous conditional laws, exact marginal coincidence should become a fragile knife-edge case rather than a generic equilibrium property. To make this explicit, we construct a latent-angle experiment in which the two modalities share the same underlying semantic variable, but one modality is perturbed by a controlled angular misalignment noise of scale $\sigma_{\text{mis}} \in \{0.0, 0.1, 0.2, 0.3, 0.4\}$. We train symmetric CLIP-

style linear encoders on S^1 and examine both the learned joint coupling and the resulting marginal discrepancy.

The result is a clear qualitative transition. When $\sigma_{\text{mis}} = 0$, the learned joint embedding law is sharply concentrated near the diagonal, indicating near-deterministic cross-modal alignment. As σ_{mis} increases, this diagonal structure progressively broadens and deforms (Fig. 5), revealing a noisier and more entropic cross-modal coupling while still preserving the coarse latent modes. This change is accompanied by the increasing marginal discrepancy reported in Fig. 2b: even mild structured misalignment is sufficient to push the learned marginals apart. These observations support the theoretical claim that the modality gap is not merely a finite-sample artifact or an optimization failure. Rather, once strict pairwise compatibility is violated, symmetric InfoNCE typically fails to maintain identical marginals. Full setup, additional visualizations, and implementation details are deferred to App. F.3.

5.2. MS-COCO Validation

Pretrained CLIP-like models on MS-COCO. We now move from controlled synthetic settings to realistic image-text representations. Our first MS-COCO study is observational: we ask whether strong pretrained CLIP-like models already exhibit a measurable modality gap, and whether better retrieval necessarily corresponds to smaller cross-modal discrepancy. Using frozen OpenCLIP checkpoints, we encode the first 5000 images from MS-COCO `val2017` together with up to five captions per image, and evaluate



(a) Observational study on pretrained OpenCLIP models.

(b) Interventional study with caption corruption.

Figure 6. MS-COCO validation of the modality-gap mechanism. (a) Stronger average retrieval does not imply a smaller modality gap. Models with similar AvgR@1 can exhibit substantially different energy distance and centroid gap, indicating that retrieval quality and cross-modal geometric agreement are related but not equivalent. (b) As the same-category caption corruption probability p increases, average retrieval degrades while the centroid gap grows for both ResNet-50 and ViT-B-16. Thus, even semantically plausible weakening of instance-level image–text correspondence is sufficient to enlarge the modality gap systematically.

retrieval in both directions under the many-captions-to-one-image protocol. As geometric diagnostics, we measure both the centroid gap $\|\mu_I - \mu_T\|$ and the energy distance between the image and text embedding marginals.

The main finding is that retrieval quality and cross-modal geometric agreement are related but clearly not equivalent. As shown in Fig. 6a, models with similar average Recall@1 can still exhibit substantially different centroid and energy gaps; the same non-monotone relation persists when the two retrieval directions are examined separately. Thus, strong pretrained retrieval performance does not imply that the image and text marginals are well matched. In other words, the modality gap persists even in capable pretrained systems, supporting the view that it is a structural property of the learned geometry rather than a mere reparameterization of downstream retrieval quality. Further setup and per-direction analyses are deferred to App. F.4.

Controlled same-category caption corruption. Our second MS-COCO study is interventional. To test more directly whether weakening image–text compatibility enlarges the modality gap, we perform controlled pair corruption on MS-COCO train_{2017} . For each image, with probability $1-p$ we keep one of its own captions, and with probability p we replace it by a caption from a different image that shares at least one COCO category. This preserves coarse semantic relatedness while breaking exact instance-level correspondence. We sweep $p \in \{0, 0.25, 0.50, 0.75, 1.00\}$, and fine-tune pretrained ResNet-50 and ViT-B-16 OpenCLIP models while freezing the backbone towers and updating only the projection heads together with the logit scale.

The trend in Fig. 6b is clean and consistent across both backbones: as p increases, retrieval degrades while the centroid gap grows monotonically. This is important for two

reasons. First, the corruption is deliberately mild: the replacement caption is not arbitrary noise, but is drawn from a semantically related image in the same category. Second, despite this coarse semantic plausibility, weakening the exact pairwise correspondence is already sufficient to produce a substantial increase in cross-modal separation. Together with the pretrained-model study, this directly supports the theoretical mechanism of § 4: once conditional compatibility is weakened, the learned image and text marginals drift further apart. Full details are deferred to App. F.4.

6. Conclusion

We establish a theoretical framework bridging the InfoNCE objective to deterministic energy landscapes, revealing a geometric bifurcation between unimodal and multimodal regimes. While unimodal learning enjoys a well-behaved convex Gibbs landscape, our analysis shows that, under conditional heterogeneity, symmetric InfoNCE can disfavor exact marginal matching. In this regime, the modality gap is not merely a sampling artifact, but can persist as a geometric consequence of a negative symmetric divergence term that induces barrier-driven marginal separation. By isolating this mechanism, our work suggests that pairwise matching alone may be insufficient, thereby motivating divergence-regularized objectives that address the cross-modal gap more directly at its source. See App. G for further discussion.

Impact Statement

This paper presents work whose goal is to advance the field of Machine Learning. There are many potential societal consequences of our work, none of which we feel must be specifically highlighted here.

References

- Arora, S., Khandeparkar, H., Khodak, M., Plevrakis, O., and Saunshi, N. A theoretical analysis of contrastive unsupervised representation learning. In *36th International Conference on Machine Learning, ICML 2019*, pp. 9904–9923, 2019. <https://arxiv.org/pdf/1902.09229>.
- Boyd, S. and Vandenberghe, L. *Convex optimization*. Cambridge university press, 2004. https://stanford.edu/~boyd/cvxbook/bv_cvxbook.pdf.
- Cai, Y., Liu, Y., Zhang, Z., and Shi, J. Q. Clap: Isolating content from style through contrastive learning with augmented prompts. In *European Conference on Computer Vision (ECCV)*, pp. 130–147, 2024. https://link.springer.com/chapter/10.1007/978-3-031-72664-4_8.
- Cai, Y., Liu, Y., Gao, E., Jiang, T., Zhang, Z., van den Hengel, A., and Shi, J. Q. On the value of cross-modal misalignment in multimodal representation learning. In *Advances in Neural Information Processing Systems*, 2025. <https://openreview.net/pdf?id=3KtPujOw5z>.
- Calder, J. and Lee, W. Understanding contrastive learning through variational analysis and neural network optimization perspectives. *arXiv preprint arXiv:2503.10812*, 2025. <https://arxiv.org/abs/2503.10812>.
- Chen, T., Kornblith, S., Norouzi, M., and Hinton, G. A simple framework for contrastive learning of visual representations. In *International conference on machine learning*, pp. 1597–1607. Pmlr, 2020. <https://proceedings.mlr.press/v119/chen20j/chen20j.pdf>.
- Chen, T., Luo, C., and Li, L. Intriguing properties of contrastive losses. *Advances in Neural Information Processing Systems*, 34:11834–11845, 2021. <https://dl.acm.org/doi/10.5555/3540261.3541166>.
- Chuang, C.-Y., Robinson, J., Yen-Chen, L., Torralba, A., and Jegelka, S. Debiased contrastive learning. In *NeurIPS*, 2020. <https://dl.acm.org/doi/10.5555/3495724.3496459>.
- Daunhawer, I., Bizeul, A., Palumbo, E., Marx, A., and Vogt, J. E. Identifiability results for multimodal contrastive learning. In *The Eleventh International Conference on Learning Representations*, 2023. https://openreview.net/forum?id=U_2kuqoTcB.
- Elfving, S., Uchibe, E., and Doya, K. Sigmoid-weighted linear units for neural network function approximation in reinforcement learning. *Neural networks*, 107:3–11, 2018. <https://doi.org/10.1016/j.neunet.2017.12.012>.
- Gutmann, M. U. and Hyvärinen, A. Noise-contrastive estimation: A new estimation principle for unnormalized statistical models. In Teh, Y. W. and Titterton, M. (eds.), *Proceedings of the 13th International Conference on Artificial Intelligence and Statistics (AISTATS 2010)*, volume 9 of *Proceedings of Machine Learning Research*, pp. 297–304, Sardinia, Italy, 2010. PMLR. <http://proceedings.mlr.press/v9/gutmann10a/gutmann10a.pdf>.
- HaoChen, J. Z. and Ma, T. A theoretical study of inductive biases in contrastive learning. In *The Eleventh International Conference on Learning Representations*, 2023. <https://openreview.net/forum?id=AuEgNlEAmed>.
- Hendrycks, D. Gaussian error linear units (gelus). *arXiv preprint arXiv:1606.08415*, 2016. <https://arxiv.org/pdf/1606.08415>.
- Hyvarinen, A. and Morioka, H. Unsupervised feature extraction by time-contrastive learning and nonlinear ica. *Advances in neural information processing systems*, 29, 2016. <https://dl.acm.org/doi/abs/10.5555/3157382.3157519>.
- Ilharco, G., Wortsman, M., Wightman, R., Gordon, C., Carlini, N., Taori, R., Dave, A., Shankar, V., Namkoong, H., Miller, J., Hajishirzi, H., Farhadi, A., and Schmidt, L. Openclip, July 2021. <https://doi.org/10.5281/zenodo.5143773>.
- Ji, W., Deng, Z., Nakada, R., Zou, J., and Zhang, L. The power of contrast for feature learning: A theoretical analysis. *Journal of Machine Learning Research*, 24 (330):1–78, 2023. <https://jmlr.org/papers/volume24/21-1501/21-1501.pdf>.
- Jia, C., Yang, Y., Xia, Y., Chen, Y.-T., Parekh, Z., Pham, H., Le, Q., Sung, Y.-H., Li, Z., and Duerig, T. Scaling up visual and vision-language representation learning with noisy text supervision. In *International conference on machine learning*, pp. 4904–4916. PMLR, 2021. <https://proceedings.mlr.press/v139/jia21b/jia21b.pdf>.
- Kingma, D. P. and Ba, J. Adam: A method for stochastic optimization. In *3rd International Conference on Learning Representations (ICLR)*, 2015. <https://arxiv.org/pdf/1412.6980>.
- Lei, Y. and Ying, Y. Fine-grained analysis of stability and generalization for stochastic gradient descent. In *International Conference on Machine Learning*, pp. 5809–

5819. PMLR, 2020. <https://proceedings.mlr.press/v119/lei20c/lei20c.pdf>.
- Liang, V. W., Zhang, Y., Kwon, Y., Yeung, S., and Zou, J. Y. Mind the gap: Understanding the modality gap in multi-modal contrastive representation learning. *Advances in Neural Information Processing Systems*, 35: 17612–17625, 2022. <https://openreview.net/forum?id=S7Evzt9uit3>.
- Liao, H., Zhou, Y., Zhang, S., Wang, M., and Zhang, S. Theoretical analysis of contrastive learning under imbalanced data: From training dynamics to a pruning solution. In *The Fourteenth International Conference on Learning Representations*, 2026. <https://openreview.net/forum?id=DUXG9E8dEO>.
- Lin, T.-Y., Maire, M., Belongie, S., Hays, J., Perona, P., Ramanan, D., Dollár, P., and Zitnick, C. L. Microsoft coco: Common objects in context. In *European conference on computer vision*, pp. 740–755. Springer, 2014. https://link.springer.com/chapter/10.1007/978-3-319-10602-1_48.
- Liu, Q. and Wang, D. Stein variational gradient descent: A general purpose bayesian inference algorithm. *Advances in neural information processing systems*, 29, 2016. https://papers.nips.cc/paper_files/paper/2016/file/b3ba8f1bee1238a2f37603d90b58898d-Paper.pdf.
- Liu, Y., Zhang, Z., Gong, D., Gao, E., Huang, B., Gong, M., van den Hengel, A., Zhang, K., and Shi, J. Q. Beyond DAGs: A latent partial causal model for multi-modal learning. In *The Fourteenth International Conference on Learning Representations*, 2026. <https://openreview.net/forum?id=bZqCBgm2N0>.
- Loshchilov, I. and Hutter, F. Decoupled weight decay regularization. In *International Conference on Learning Representations*, 2019. <https://openreview.net/forum?id=Bkg6RiCqY7>.
- Miyato, T., Kataoka, T., Koyama, M., and Yoshida, Y. Spectral normalization for generative adversarial networks. In *International Conference on Learning Representations*, 2018. <https://openreview.net/forum?id=B1QRgziT->.
- Mnih, A. and Teh, Y. W. A fast and simple algorithm for training neural probabilistic language models. In *29th International Conference on Machine Learning, ICML 2012*, 2012. <https://icml.cc/2012/papers/855.pdf>.
- Oord, A. v. d., Li, Y., and Vinyals, O. Representation learning with contrastive predictive coding. *arXiv preprint arXiv:1807.03748*, 2018. <https://arxiv.org/abs/1807.03748>.
- Poole, B., Ozair, S., van den Oord, A., Alemi, A. A., and Tucker, G. On variational bounds of mutual information. In *Proceedings of the 36th International Conference on Machine Learning*, volume 97, pp. 5171–5180. PMLR, 2019. <https://proceedings.mlr.press/v97/poole19a.html>.
- Radford, A., Kim, J. W., Hallacy, C., Ramesh, A., Goh, G., Agarwal, S., Sastry, G., Askell, A., Mishkin, P., Clark, J., et al. Learning transferable visual models from natural language supervision. In *International conference on machine learning*, pp. 8748–8763. PMLR, 2021. <https://proceedings.mlr.press/v139/radford21a/radford21a.pdf>.
- Ryu, J. J., Yeddanapudi, P., Xu, X., and Wornell, G. W. Contrastive predictive coding done right for mutual information estimation. In *The Fourteenth International Conference on Learning Representations*, 2026. <https://openreview.net/forum?id=JodkBXWgbA>.
- Saunshi, N., Ash, J., Goel, S., Misra, D., Zhang, C., Arora, S., Kakade, S., and Krishnamurthy, A. Understanding contrastive learning requires incorporating inductive biases. In *International Conference on Machine Learning*, pp. 19250–19286. PMLR, 2022. <https://proceedings.mlr.press/v162/saunshi22a/saunshi22a.pdf>.
- Shi, P., Welle, M. C., Björkman, M., and Kragic, D. Towards understanding the modality gap in clip. In *ICLR 2023 workshop on multimodal representation learning: perks and pitfalls*, 2023. <https://openreview.net/pdf?id=8W3KGzw7fNI>.
- Sun, J., Zhang, S., Li, H., and Wang, M. Contrastive learning with data misalignment: Feature purity, training dynamics and theoretical generalization guarantees. In *The Thirty-ninth Annual Conference on Neural Information Processing Systems*, 2025. <https://openreview.net/forum?id=JM1YzOMDxI>.
- Tian, Y., Krishnan, D., and Isola, P. Contrastive multiview coding. In *European conference on computer vision*, pp. 776–794. Springer, 2020. https://www.ecva.net/papers/eccv_2020/papers_ECCV/papers/123560749.pdf.
- Tschannen, M., Djolonga, J., Rubenstein, P., Gelly, S., and Lucic, M. On mutual information maximization for representation learning. In *Eighth International Conference on Learning Representations*. OpenReview. net,

2020. <https://openreview.net/forum?id=rkxoh24FPH>.
- Uesaka, T., Suzuki, T., Takida, Y., Lai, C.-H., Murata, N., and Mitsufuji, Y. Weighted point set embedding for multimodal contrastive learning toward optimal similarity metric. In *The Thirteenth International Conference on Learning Representations*, 2025. <https://openreview.net/forum?id=uSz2K30RRd>.
- Von Kügelgen, J., Sharma, Y., Gresele, L., Brendel, W., Schölkopf, B., Besserve, M., and Locatello, F. Self-supervised learning with data augmentations provably isolates content from style. *Advances in neural information processing systems*, 34:16451–16467, 2021. https://openreview.net/forum?id=4pf_pOo0Dt.
- Wang, F. and Liu, H. Understanding the behaviour of contrastive loss. In *Proceedings of the IEEE/CVF conference on computer vision and pattern recognition*, pp. 2495–2504, 2021. https://openaccess.thecvf.com/content/CVPR2021/papers/Wang_Understanding_the_Behaviour_of_Contrastive_Loss_CVPR_2021_paper.pdf.
- Wang, T. and Isola, P. Understanding contrastive representation learning through alignment and uniformity on the hypersphere. In *International conference on machine learning*, pp. 9929–9939. PMLR, 2020. <https://dl.acm.org/doi/10.5555/3524938.3525859>.
- Welling, M. and Teh, Y. W. Bayesian learning via stochastic gradient langevin dynamics. In *Proceedings of the 28th international conference on machine learning (ICML-11)*, pp. 681–688, 2011. <https://www.stats.ox.ac.uk/~teh/research/compstats/WelTeh2011a.pdf>.
- Yao, D., Xu, D., Lachapelle, S., Magliacane, S., Taslakian, P., Martius, G., von Kügelgen, J., and Locatello, F. Multi-view causal representation learning with partial observability. In *The Twelfth International Conference on Learning Representations*, 2024. <https://openreview.net/forum?id=OGtnhKQJms>.
- Yin, W., Xiao, Z., Zhou, P., Yu, S., Shen, J., Sonke, J.-J., and Gavves, S. Distributional vision-language alignment by cauchy-schwarz divergence. In *The Fourteenth International Conference on Learning Representations*, 2026. <https://openreview.net/forum?id=UUAjF4xL0e>.
- Yoshida, N., Hayakawa, S., Takida, Y., Uesaka, T., Wakaki, H., and Mitsufuji, Y. Theoretical refinement of clip by utilizing linear structure of optimal similarity. *arXiv preprint arXiv:2510.15508*, 2025. <https://arxiv.org/pdf/2510.15508>.
- Zhai, X., Mustafa, B., Kolesnikov, A., and Beyer, L. Sigmoid loss for language image pre-training. In *Proceedings of the IEEE/CVF international conference on computer vision*, pp. 11975–11986, 2023. https://openaccess.thecvf.com/content/ICCV2023/papers/Zhai_Sigmoid_Loss_for_Language_Image_Pre-Training_ICCV_2023_paper.pdf.
- Zhang, G., Wang, C., Xu, B., and Grosse, R. Three mechanisms of weight decay regularization. In *International Conference on Learning Representations*, 2019. <https://openreview.net/forum?id=B1lz-3Rct7>.
- Zimmermann, R. S., Sharma, Y., Schneider, S., Bethge, M., and Brendel, W. Contrastive learning inverts the data generating process. In *International conference on machine learning*, pp. 12979–12990. PMLR, 2021. <https://proceedings.mlr.press/v139/zimmermann21a/zimmermann21a.pdf>.

Appendix

Contents

A. Related Work	15
B. Interpretation of Assumptions	16
B.1. On the Optimization Regularity Conditions	16
B.2. Interpretation of the Sharp Diagonal Peak Regime	17
B.3. On Density Floors and Positivity of the Effective Laws	17
C. Lemmas and Extended Formal Statements	18
C.1. Uniform Gradient Bounds for InfoNCE Objectives	18
C.2. Sharp-peak Smoothing Implies Vanishing KDE Mismatch	21
C.3. Unimodal Parametric Inheritance and Emergence of Uniformity	24
C.4. Multimodal Parametric Inheritance	26
D. Proofs of Unimodal Formal Statements	29
D.1. Proof of Thm. 3.1	29
D.2. Proof of Prop. 3.1	32
D.3. Proof of Prop. 3.2	34
D.4. Proof of Thm. 3.2	35
E. Proofs of Multimodal Formal Statements	37
E.1. Proof of Thm. 4.1	37
E.2. Proof of Prop. 4.1	41
E.3. Proof of Thm. 4.2	44
F. Experimental Details	45
F.1. Large-Batch Gradient Consistency Across Critics	46
F.2. Unimodal Gibbs Equilibrium and Low-Temperature Concentration	46
F.3. Multimodal Structural Gap under Controlled Misalignment	48
F.4. MS-COCO Experiments: Pretrained Gap and Controlled Pair Corruption	50
G. Discussion	54

Table 1. Core notations used throughout the paper.

Spaces, Measures, Encoders and Laws	
\mathcal{X}, \mathcal{Y}	Observation spaces; in the unimodal case both views lie in \mathcal{X} .
$\mathcal{Z} \subseteq \mathbb{R}^n$	Common representation space, with volume measure μ .
$\mathcal{P}(\mathcal{S})$	Set of probability measures on a measurable space \mathcal{S} .
$\mathcal{P}_\mu(\mathcal{Z})$	Set of probability densities on \mathcal{Z} w.r.t. μ .
$r_{\text{um}} \in \mathcal{P}(\mathcal{X} \times \mathcal{X})$	Unimodal positive-pair law governing $(\mathbf{x}, \tilde{\mathbf{x}})$.
$r_{\text{mm}} \in \mathcal{P}(\mathcal{X} \times \mathcal{Y})$	Multimodal positive-pair law governing (\mathbf{x}, \mathbf{y}) .
$p_{\mathbf{x}}, p_{\mathbf{y}}$	Marginal data laws on \mathcal{X} and \mathcal{Y} , respectively.
Θ, Φ	Compact parameter spaces of the encoder families.
$f_\theta : \mathcal{X} \rightarrow \mathcal{Z}$	Encoder for the first modality.
$g_\phi : \mathcal{Y} \rightarrow \mathcal{Z}$	Encoder for the second modality.
$q_\theta := (f_\theta)_\# p_{\mathbf{x}}$	Encoded marginal law induced by f_θ .
$q_\phi := (g_\phi)_\# p_{\mathbf{y}}$	Encoded marginal law induced by g_ϕ .
$\pi_{\theta\theta} := (f_\theta \times f_\theta)_\# r_{\text{um}}$	Encoded unimodal positive-pair law.
$\pi_{\theta\phi} := (f_\theta \times g_\phi)_\# r_{\text{mm}}$	Encoded multimodal positive-pair law.
InfoNCE Objectives and Kernel Quantities	
$N \in \mathbb{N}_+$	Number of negatives in the InfoNCE denominator.
$s(\mathbf{z}, \mathbf{w})$	Similarity critic on $\mathcal{Z} \times \mathcal{Z}$.
$\kappa_\tau(\mathbf{z}, \mathbf{w}) = \exp(s(\mathbf{z}, \mathbf{w})/\tau)$	Exponential similarity kernel at temperature $\tau > 0$.
$V_\kappa(\tau)$	Kernel volume constant under Asm. 2.1.
$\mathcal{L}_{\text{NCE}}(\theta)$	Empirical unimodal InfoNCE loss.
$\mathcal{L}_{\text{NCE}}^{\text{Sym}}(\theta, \phi)$	Symmetric multimodal InfoNCE loss.
$\mathcal{L}_{\text{NCE}}^{\mathbf{x} \rightarrow \mathbf{y}}(\theta, \phi), \mathcal{L}_{\text{NCE}}^{\mathbf{y} \rightarrow \mathbf{x}}(\phi, \theta)$	Directional multimodal InfoNCE losses for $\mathbf{x} \rightarrow \mathbf{y}$ and $\mathbf{y} \rightarrow \mathbf{x}$.
$\Gamma_{\theta, \tau}, \Gamma_{\phi, \tau}$	Population partition fields at τ , induced by q_θ and q_ϕ , respectively.
$\tilde{\rho}_{\theta, \tau}, \tilde{\rho}_{\phi, \tau}$	Kernel-smoothed densities at τ , induced by q_θ and q_ϕ , respectively.
Unimodal Geometry	
$\nu_{\theta, \mathbf{z}}$	Conditional law of the positive partner given encoded query \mathbf{z} under $\pi_{\theta\theta}$.
$U_\theta(\mathbf{z}) : \mathcal{Z} \rightarrow \mathbb{R}$	Unimodal alignment potential field: the conditional expected similarity at \mathbf{z} .
$H_\times(q, \tilde{\rho})$	Cross-entropy of a probability measure q against a positive density $\tilde{\rho}$.
$H(\rho)$	Differential entropy of density ρ .
$\mathcal{J}_\tau(\theta)$	Unimodal parametric energy optimized in the large-batch limit.
$\mathcal{F}_{\tau, U}(\rho)$	Intrinsic unimodal free-energy functional over densities ρ .
Multimodal Geometry	
$\nu_{\theta\phi, \mathbf{z}}$	Conditional law of the ϕ -encoded partner given \mathbf{z} under $\pi_{\theta\phi}$.
$\nu_{\phi\theta, \mathbf{w}}$	Conditional law of the θ -encoded partner given \mathbf{w} under $\pi_{\theta\phi}$.
$U_{\theta \rightarrow \phi}(\mathbf{z}), U_{\phi \rightarrow \theta}(\mathbf{z})$	Directional alignment potential seen by θ against ϕ , and the reverse version.
$\mathcal{J}_\tau^{\mathbf{x} \rightarrow \mathbf{y}}(\theta, \phi)$	Directional multimodal parametric energy for $x \rightarrow y$.
$\mathcal{J}_\tau^{\mathbf{y} \rightarrow \mathbf{x}}(\theta, \phi)$	Directional multimodal parametric energy for $y \rightarrow x$.
$\mathcal{J}_\tau^{\text{Sym}}(\theta, \phi)$	Symmetric multimodal parametric energy.
$\mathbf{U}_{1,2} := (U_{1 \rightarrow 2}, U_{2 \rightarrow 1})$	Pair of directional potentials in the intrinsic multimodal functional.
$\mathcal{F}_{\tau, \mathbf{U}_{1,2}}^{\text{Sym}}(\rho_1, \rho_2)$	Intrinsic symmetric multimodal energy.
$D_{\text{KL}}(\rho_1 \parallel \rho_2)$	Kullback–Leibler divergence.
$D_{\text{KL}}^{\text{Sym}}(\rho_1, \rho_2)$	Symmetric KL divergence, $\frac{1}{2}(D_{\text{KL}}(\rho_1 \parallel \rho_2) + D_{\text{KL}}(\rho_2 \parallel \rho_1))$.
$\underline{\rho} > 0$	Density floor used to restrict the feasible probability density set.
$\mathcal{P}_{\mu, \underline{\rho}}(\mathcal{Z})$	Strictly positive density class satisfying $\rho \geq \underline{\rho}$ a.e. and $\int_{\mathcal{Z}} \rho d\mu = 1$.
$V_{1 2}(\mathbf{z})$	Effective barrier potential for modality 1 given modality 2, $\frac{1}{\tau}U_{1 \rightarrow 2} + \log \rho_2$.
$V_{2 1}(\mathbf{z})$	Effective barrier potential for modality 2 given modality 1.

A. Related Work

Contrastive objectives and information viewpoints. InfoNCE can be viewed as a modern instance of noise-contrastive density-ratio estimation (NCE): a positive pair is contrasted against negatives drawn from a background marginal through a softmax normalization, inheriting classical NCE principles and neural approximations (Gutmann & Hyvärinen, 2010; Mnih & Teh, 2012; Oord et al., 2018). This connection also underlies its widespread use as a scalable surrogate for mutual-information-style criteria (Poole et al., 2019; Tschannen et al., 2020). Recent work has further clarified that InfoNCE is best interpreted as learning structured density ratios rather than as an accurate mutual-information estimator per se, and proposes refined objectives for MI estimation (orthogonal to representation quality) (Ryu et al., 2026). Multimodal foundation models such as CLIP and ALIGN adopt the symmetric bidirectional InfoNCE objective as the core pretraining loss (Radford et al., 2021; Jia et al., 2021).

Population geometry of contrastive learning. A prominent theoretical lens studies the population landscape induced by contrastive objectives, most notably via the alignment–uniformity decomposition on hyperspherical embeddings (Wang & Isola, 2020; Wang & Liu, 2021; Chen et al., 2021). Related perspectives emphasize that contrastive objectives can admit multiple (and sometimes trivial) minimizers, and that the optimization procedure and parametrization can implicitly select structured solutions (Calder & Lee, 2025). While much of this literature characterizes static properties of minimizers, our study focuses on the mechanistic descent directions induced by InfoNCE. By proving large-batch value and gradient consistency, we bridge the stochastic empirical loss and an explicit deterministic energy landscape, enabling a rigorous analysis of the induced geometry on representation measures beyond the hypersphere to general compact manifolds.

Training-dynamics analyses under stylized models. Complementary to population-level geometric analyses, a growing line of work studies contrastive learning through training dynamics in parameter space under structured data models (e.g., sparse-feature or augmentation-based assumptions), aiming to explain feature selection, suppression, or robustness phenomena. For example, recent analyses characterize stage-wise neuron/weight dynamics under data imperfections such as misalignment or imbalance, and motivate interventions such as filtering or pruning (Sun et al., 2025; Liao et al., 2026). These results provide fine-grained algorithmic insight under specific modeling assumptions and architectures, including Transformer-based encoders under imbalance (Liao et al., 2026). Our emphasis is different: rather than assuming a particular latent feature model to track weight dynamics, we analyze the objective-induced geometry directly on the embedding manifold in a distribution-agnostic framework, exposing how the softmax denominator gives rise to deterministic population fields in the large-batch regime.

Learning-theoretic analyses and objective design. A separate line develops learning-theoretic guarantees for contrastive representations under stylized generative assumptions (e.g., latent-class or multi-view models), and analyzes how negative sampling, false negatives, and objective variants affect downstream transfer (Arora et al., 2019; Saunshi et al., 2022; Chuang et al., 2020; Tian et al., 2020; HaoChen & Ma, 2023; Ji et al., 2023). Recent analyses of CLIP-style training also characterize the structure of optimal similarities and propose refinements that better exploit this structure (Uesaka et al., 2025; Yoshida et al., 2025). Our results are largely orthogonal in emphasis: instead of proposing a new estimator or specializing to a latent generative model, we characterize the deterministic geometry imposed by InfoNCE itself via large-batch energy limits and intrinsic variational functionals.

Multimodal representation alignment. Empirical work shows that CLIP-style alignment can coexist with a persistent population-level modality gap (Liang et al., 2022; Shi et al., 2023), and recent methods attempt to close or control this gap via architectural adapters, alternative losses, or additional alignment regularizers. In particular, Yin et al. (2026) argue that mutual information alone is insufficient for multimodal alignment and propose augmenting InfoNCE with a kernel-estimated Cauchy–Schwarz divergence to explicitly align modality distributions, including settings with unpaired data. Alternative normalization and loss formulations (e.g., replacing the global softmax normalization with pairwise sigmoid objectives) further highlight that the induced cross-modal coupling is sensitive to objective design (Zhai et al., 2023). Our contribution provides a mechanistic account complementary to these approaches: we show that the symmetric InfoNCE objective induces cross-modal coupling where each modality’s density shapes the other’s effective field via a persistent negative symmetric divergence term in the intrinsic landscape. Consequently, the modality gap is not merely an initialization artifact but a structural property of the bidirectional loss geometry, motivating distribution-level regularization as a principled remedy.

Identifiability theory in contrastive learning. A complementary line of theory asks when contrastive objectives can recover latent generative factors under explicit assumptions on the data-generating process. In nonlinear ICA, auxiliary

variables (e.g., temporal nonstationarity) break classical non-identifiability, enabling source recovery up to component-wise transformations (Hyvarinen & Morioka, 2016). For invertible-mixing models, global optima can invert the generator up to linear ambiguities (typically orthogonal transforms on hyperspherical latents), illustrating spectral identifiability phenomena (Zimmermann et al., 2021; Liu et al., 2026). In multi-view models separating invariant “content” from view-varying “style”, results characterize recovery of the invariant block up to an invertible mapping (Von Kügelgen et al., 2021; Cai et al., 2024). Extending to genuinely multimodal settings with distinct generative mechanisms, contrastive learning can block-identify shared cross-modal factors even under nontrivial dependencies (Daunhawer et al., 2023). Broader causal analyses with partial observability establish identifiability of shared information up to smooth bijections (Yao et al., 2024), while data misalignment formulations demonstrate that multimodal contrastive learning encodes exactly the semantics invariant to selection or perturbation biases (Cai et al., 2025). Our work is complementary in scope: rather than deriving recovery guarantees under specified generative models, we characterize the objective-induced optimization geometry itself, and identify a structural mechanism for persistent modality gaps that standard identifiability analyses do not typically address.

B. Interpretation of Assumptions

B.1. On the Optimization Regularity Conditions

We argue that the regularity conditions in Asm. 3.1 are compatible with standard practice in representation learning. We make instances with two dominant geometric regimes: the spherical regime used in modern contrastive learning (e.g., SimCLR (Chen et al., 2020), CLIP (Radford et al., 2021)) and the Euclidean regime common in classical kernel methods. Both admit the generalized exponential form $\kappa_\tau(\mathbf{z}, \mathbf{w}) := \exp(s(\mathbf{z}, \mathbf{w})/\tau)$.

- *Spherical regime (von Mises–Fisher kernel)*. Representations are constrained to the hypersphere \mathbb{S}^{d-1} via ℓ_2 normalization, and the critic is the cosine similarity $s(\mathbf{z}, \mathbf{w}) = \langle \mathbf{z}, \mathbf{w} \rangle$:

$$\kappa_\tau^{(\text{vmf})}(\mathbf{z}, \mathbf{w}) := \exp\left(\frac{\langle \mathbf{z}, \mathbf{w} \rangle}{\tau}\right), \quad \forall \mathbf{z}, \mathbf{w} \in \mathbb{S}^{n-1}. \quad (11)$$

- *Euclidean regime (RBF kernel)*. The representations lie in a compact subset of \mathbb{R}^n , and the similarity critic is the negative squared Euclidean distance $s(\mathbf{z}, \mathbf{w}) = -\|\mathbf{z} - \mathbf{w}\|^2$:

$$\kappa_\tau^{(\text{rbf})}(\mathbf{z}, \mathbf{w}) := \exp\left(-\frac{\|\mathbf{z} - \mathbf{w}\|^2}{\tau}\right). \quad (12)$$

Encoder regularity. Condition Asm. 3.1 (i) requires that for each \mathbf{x} , the map $\theta \mapsto f_\theta(\mathbf{x})$ is C^1 and that its parameter Jacobian is uniformly bounded: $\sup_{\theta \in \Theta} \sup_{\mathbf{x} \in \mathcal{X}} \|J_\theta f_\theta(\mathbf{x})\| < \infty$. For standard neural encoders built from differentiable primitives (e.g., linear maps, convolutions, normalization layers) and smooth activations (e.g., GELU (Hendrycks, 2016), SiLU (Elfving et al., 2018)), the map $\theta \mapsto f_\theta(\mathbf{x})$ is C^1 (or at least piecewise C^1 , which suffices for almost-everywhere analysis). In practice, uniform Jacobian control is promoted by explicit Lipschitz constraints (e.g., spectral normalization, which bounds layer operator norms and hence the network Jacobian via composition (Miyato et al., 2018)) together with standard norm-regularizing training choices such as weight decay (Loshchilov & Hutter, 2019; Zhang et al., 2019). Accordingly, we interpret compactness of Θ as a mild *localization* assumption: although the ambient parameter space is \mathbb{R}^p , successful training typically keeps iterates within a bounded region (often formalized as “SGD iterates belong to a ball” in stability analyses (Lei & Ying, 2020)). One may therefore restrict the analysis to a sufficiently large compact subset Θ_R containing the training trajectory, or equivalently consider projected updates onto Θ_R as standard in constrained optimization (Boyd & Vandenberghe, 2004).

Critic regularity. Condition Asm. 3.1 (ii) requires that s is C^1 on an open neighborhood of $\mathcal{Z} \times \mathcal{Z}$ and that $\sup_{(\mathbf{z}, \mathbf{w}) \in \mathcal{Z} \times \mathcal{Z}} \|\nabla s(\mathbf{z}, \mathbf{w})\| < \infty$. In the spherical regime, $s(\mathbf{z}, \mathbf{w}) = \langle \mathbf{z}, \mathbf{w} \rangle$ is C^∞ on $\mathbb{R}^d \times \mathbb{R}^d$ with gradient norms $\|\nabla_{\mathbf{z}} s\| = \|\mathbf{w}\|$ and $\|\nabla_{\mathbf{w}} s\| = \|\mathbf{z}\|$. Since $\|\mathbf{z}\| = \|\mathbf{w}\| = 1$, these are uniformly bounded by 1. In the Euclidean regime, $s(\mathbf{z}, \mathbf{w}) = -\|\mathbf{z} - \mathbf{w}\|^2$ is also C^∞ with gradients scaling linearly with distance. Thus, provided \mathcal{Z} is compact (e.g., via bounded activations like tanh or explicit clipping), $\|\nabla s\|$ remains uniformly bounded on $\mathcal{Z} \times \mathcal{Z}$.

Boundedness of the kernel. For any fixed $\tau > 0$, the exponential kernel $\kappa_\tau = \exp(s/\tau)$ is strictly positive and bounded. For the spherical regime, $\langle \mathbf{z}, \mathbf{w} \rangle \in [-1, 1]$ implies $\kappa_\tau^{(\text{vmf})}(\mathbf{z}, \mathbf{w}) \in [\exp(-1/\tau), \exp(1/\tau)]$. For the RBF regime on a

compact domain with diameter $D = \text{diam}(\mathcal{Z})$, we have $\kappa_\tau^{(\text{rbf})}(\mathbf{z}, \mathbf{w}) \in [\exp(-D^2/\tau), 1]$. Crucially, in both cases, the kernel is bounded away from zero ($\kappa \geq c > 0$), ensuring that the logarithmic loss terms are well-defined and Lipschitz continuous.

B.2. Interpretation of the Sharp Diagonal Peak Regime

Geometric Interpretation. Asm. 3.2 is a uniform non-degeneracy condition on the similarity critic $s(\mathbf{z}, \mathbf{w})$ near the diagonal $\mathbf{w} = \mathbf{z}$. The inequalities in Eq. (6) state that for each anchor \mathbf{z} , the function $\mathbf{w} \mapsto s(\mathbf{z}, \mathbf{w})$ has an isolated maximizer at $\mathbf{w} = \mathbf{z}$ and admits a locally quadratic upper and lower envelope in geodesic distance. For the exponential kernel $\kappa_\tau(\mathbf{z}, \mathbf{w}) = \exp(s(\mathbf{z}, \mathbf{w})/\tau)$, this condition implies that the normalized kernel

$$\bar{\kappa}_\tau := \frac{\kappa_\tau(\mathbf{z}, \mathbf{w})}{\int_{\mathcal{Z}} \kappa_\tau(\mathbf{z}, \mathbf{u}) d\mu(\mathbf{u})}$$

concentrates its mass in a geodesic ball $\mathbb{B}_{c\sqrt{\tau}}(\mathbf{z}) := \{\mathbf{w} \in \mathcal{Z} \mid d_{\mathcal{Z}}(\mathbf{z}, \mathbf{w}) < c\sqrt{\tau}\}$ for some constant $c > 0$ uniformly in \mathbf{z} . Intuitively, $\bar{\kappa}_\tau(\mathbf{z}, \cdot)$ behaves like a Gaussian bump of bandwidth $\sqrt{\tau}$ centered at \mathbf{z} . As a result, the partition field $\Gamma_{\theta, \tau}(\mathbf{z}) = \int_{\mathcal{Z}} \kappa_\tau(\mathbf{z}, \mathbf{w}) dq_\theta(\mathbf{w})$ probes only a local neighborhood of \mathbf{z} when τ is small, and the smoothed density $\tilde{\rho}_{\theta, \tau} = \Gamma_{\theta, \tau}/V_\kappa(\tau)$ becomes a controlled local smoothing ρ_θ .

Examples. For the RBF regime with negative Euclidean distance as critic $s(\mathbf{z}, \mathbf{w}) = -\|\mathbf{z} - \mathbf{w}\|^2$, Eq. (6) holds with equality. On the hypersphere regime with cosine similarity as critic, $1 - \langle \mathbf{z}, \mathbf{w} \rangle \asymp d_{\mathbb{S}^{n-1}}(\mathbf{z}, \mathbf{w})^2$ for nearby points, so the same local quadratic behavior yields a vMF-type bump.

B.3. On Density Floors and Positivity of the Effective Laws

Several parts of our analysis involve logarithms of representation densities (e.g., cross-entropies and KL-type terms). In the unimodal intrinsic problem this is benign—the entropy term $-H(\rho)$ already acts as an interior regularizer and the Gibbs minimizer is well-defined without imposing a pointwise lower bound. In the *multimodal* intrinsic problem, however, the objective *subtracts* a symmetric KL-type divergence, creating an explicit “barrier” mechanism; without positivity constraints the variational problem becomes ill-posed. This section explains why (i) the *parametric* large-batch objective is automatically interior due to smoothing, and (ii) the intrinsic density floor is a faithful theoretical proxy for that interior regime.

Smoothed densities. In the large-batch expansion, the quantities that appear are the kernel-smoothed μ -densities $\tilde{\rho}_{\theta, \tau}, \tilde{\rho}_{\phi, \tau}$ from Def. 2.2, not the raw pushforwards q_θ, q_ϕ . Because the exponential kernel satisfies $\kappa_\tau(\mathbf{z}, \mathbf{w}) = \exp(s(\mathbf{z}, \mathbf{w})/\tau) > 0$ pointwise, we have for every $\tau > 0$ and every probability measure q_θ ,

$$\tilde{\rho}_{\theta, \tau}(\mathbf{z}) = \frac{1}{V_\kappa(\tau)} \int_{\mathcal{Z}} \kappa_\tau(\mathbf{z}, \mathbf{w}) dq_\theta(\mathbf{w}) > 0, \quad \forall \mathbf{z} \in \mathcal{Z},$$

and analogously for $\tilde{\rho}_{\phi, \tau}$. Moreover, when κ_τ is continuous (as in our standing setting), $\tilde{\rho}_{\theta, \tau}$ is continuous on compact \mathcal{Z} and therefore attains a strictly positive minimum

$$m_{\theta, \tau} := \min_{\mathbf{z} \in \mathcal{Z}} \tilde{\rho}_{\theta, \tau}(\mathbf{z}) > 0,$$

and similarly $m_{\phi, \tau} > 0$. Thus all log-terms appearing in the parametric energy are well-defined at finite temperature. Importantly, $m_{\theta, \tau}$ depends on (θ, τ) and we do *not* assume a uniform lower bound over Θ (or $\Theta \times \Phi$ in the multimodal case).

From smoothed densities to raw parametric densities. When we compare $\mathcal{J}_\tau(\theta)$ to intrinsic functionals expressed in terms of an unsmoothed density $\rho_\theta := dq_\theta/d\mu$ (when $q_\theta \ll \mu$), the only discrepancy is the KDE bias between $\tilde{\rho}_{\theta, \tau}$ and ρ_θ . Concretely, whenever

$$\|\tilde{\rho}_{\theta, \tau} - \rho_\theta\|_\infty \leq \frac{1}{2} m_{\theta, \tau}, \tag{13}$$

we immediately obtain $\rho_\theta(\mathbf{z}) \geq \frac{1}{2} m_{\theta, \tau}$ for all \mathbf{z} , i.e., the raw density inherits a (parameter-dependent) floor. The sharp-peak smoothing lemma (Lem. C.3) is precisely the tool that makes Eq. (13) achievable in the low-temperature regime: under

Asm. 3.2 and mild regularity, the KDE mismatch vanishes as $\tau \downarrow 0^+$ for each fixed θ satisfying the lemma’s hypotheses. Accordingly, the “density floor” used in the intrinsic best-response analysis should be viewed as a technical proxy for the fact that, at any finite τ , the *effective* densities that govern the parametric objective are strictly positive and (in regimes of small KDE bias) the same interior behavior transfers to ρ_θ, ρ_ϕ .

Density floor in multimodal analysis. In the multimodal formulation (Def. 4.3), we restrict (ρ_1, ρ_2) to

$$\mathcal{P}_{\mu, \underline{\rho}}(\mathcal{Z}) := \left\{ \rho \in L^1(\mathcal{Z}) : \rho \geq \underline{\rho} \text{ } \mu\text{-a.e.}, \int_{\mathcal{Z}} \rho \, d\mu = 1 \right\},$$

for some fixed $\underline{\rho} > 0$. This floor serves two roles.

(i) *Well-posedness under negative symmetric divergence.* Because the multimodal functional contains a *negative* symmetric divergence coupling, allowing densities to vanish can make the objective unbounded below. Indeed, if $\rho_1 = 0$ on a set \mathcal{A} with $\mu(\mathcal{A}) > 0$ while $\rho_2 > 0$ on \mathcal{A} , then $D_{\text{KL}}(\rho_2 \parallel \rho_1) = +\infty$ and hence the negative symmetric divergence term drives $\mathcal{F}_{\tau, \mathbf{U}}^{\text{mm}}(\rho_1, \rho_2) = -\infty$. The floor $\rho_i \geq \underline{\rho}$ prevents this degeneracy and makes the best-response problem meaningful. Equivalently, one may view the constraint as a hard version of the standard “interior” condition used to keep log-barrier objectives finite.

(ii) *Transparent best-response geometry.* With the floor, we can decompose

$$\rho_1 = \underline{\rho} + \eta, \quad \eta \geq 0, \quad \int_{\mathcal{Z}} \eta \, d\mu =: M_{\text{ex}} = 1 - \underline{\rho} \mu(\mathcal{Z}),$$

and analogously for ρ_2 . This isolates a fixed “background” mass from an “excess” budget M_{ex} , making the extremal best-response behavior in Prop. 4.1 quantitatively controllable. In this sense, the density floor is not an arbitrary restriction: it is the simplest device that (a) mirrors the intrinsic interiority of the parametric smoothed quantities at finite τ , and (b) exposes the barrier-driven coordinate-collapse mechanism in closed form.

C. Lemmas and Extended Formal Statements

C.1. Uniform Gradient Bounds for InfoNCE Objectives

In this section, we prove uniform gradient bounds for unimodal and multimodal InfoNCE objectives, which are used to justify limit–gradient interchange in Thms. 3.1 and 4.1.

C.1.1. UNIMODAL OPTIMIZATION STABILITY

Lemma C.1 (Stable unimodal optimization). *Assume Asm. 3.1. Fix any temperature $\tau > 0$ and any batch size $N \in \mathbb{N}_+$. Then the unimodal InfoNCE objective defined in Eq. (1) has a uniformly bounded gradient over the parameter space Θ . Formally, there exists a constant $C(\tau) < \infty$ such that $\|\nabla_{\theta} \mathcal{L}_{\text{NCE}}(\theta)\| \leq C(\tau)$, uniformly for all $\theta \in \Theta$.*

Proof intuition. This proof establishes that the InfoNCE gradients cannot explode, providing a uniform upper bound that is strictly independent of the number of negative samples N . The intuition rests on two core mechanisms:

(i) Because the representation manifold is compact and both the encoder and similarity functions are sufficiently smooth with bounded Jacobians, the chain rule guarantees that the gradient of any single pairwise similarity score is inherently bounded.

(ii) The gradient of the log-partition denominator mathematically simplifies to a softmax-weighted sum of the negative-pair gradients. Because this is a convex combination (i.e., a weighted average where coefficients sum to 1), the aggregated gradient vector cannot stretch beyond the maximum length of the individual bounded vectors.

Consequently, the contrastive push from an arbitrarily large sea of negatives is structurally prevented from overwhelming the gradient, ensuring global stability for the entire learning objective.

Proof. Step 1: Bounding components in the loss. Since \mathcal{Z} is compact, the product $\mathcal{Z} \times \mathcal{Z}$ is compact. By Asm. 3.1 (ii), s is C^1 on an open neighborhood of $\mathcal{Z} \times \mathcal{Z}$, so ∇s is continuous on $\mathcal{Z} \times \mathcal{Z}$ and hence attains its maximum norm on this

compact set. For a fixed $\tau > 0$, define the temperature-dependent critic sensitivity bound

$$C_s(\tau) := \sup_{(\mathbf{z}, \mathbf{w}) \in \mathcal{Z} \times \mathcal{Z}} \left\| \nabla_{(\mathbf{z}, \mathbf{w})} \left(\frac{1}{\tau} s(\mathbf{z}, \mathbf{w}) \right) \right\| = \frac{1}{\tau} \sup_{(\mathbf{z}, \mathbf{w}) \in \mathcal{Z} \times \mathcal{Z}} \|\nabla s(\mathbf{z}, \mathbf{w})\| < \infty. \quad (14)$$

Next, by Asm. 3.1 (i), the encoder Jacobian is uniformly bounded:

$$C_\Theta := \sup_{\theta \in \Theta} \sup_{\mathbf{x} \in \mathcal{X}} \|J_\theta f_\theta(\mathbf{x})\| < \infty. \quad (15)$$

For any $\mathbf{x}, \mathbf{x}' \in \mathcal{X}$ with representations $\mathbf{z} = f_\theta(\mathbf{x})$ and $\mathbf{w} = f_\theta(\mathbf{x}')$, define

$$\alpha_\theta(\mathbf{z}, \mathbf{w}) := \nabla_\theta \left(\frac{1}{\tau} s(\mathbf{z}, \mathbf{w}) \right).$$

By the chain rule,

$$\alpha_\theta(\mathbf{z}, \mathbf{w}) = \nabla_{\mathbf{z}} \left(\frac{1}{\tau} s(\mathbf{z}, \mathbf{w}) \right)^\top J_\theta f_\theta(\mathbf{x}) + \nabla_{\mathbf{w}} \left(\frac{1}{\tau} s(\mathbf{z}, \mathbf{w}) \right)^\top J_\theta f_\theta(\mathbf{x}').$$

Therefore, by the triangle inequality and sub-multiplicativity,

$$\|\alpha_\theta(\mathbf{z}, \mathbf{w})\| \leq \left\| \nabla_{\mathbf{z}} \frac{1}{\tau} s(\mathbf{z}, \mathbf{w}) \right\| \cdot \|J_\theta f_\theta(\mathbf{x})\| + \left\| \nabla_{\mathbf{w}} \frac{1}{\tau} s(\mathbf{z}, \mathbf{w}) \right\| \cdot \|J_\theta f_\theta(\mathbf{x}')\| \leq 2C_s(\tau)C_\Theta. \quad (16)$$

Thus, the parameter gradient of any pairwise similarity term is uniformly bounded.

Step 2: Gradient of the empirical partition function. Fix an anchor $\mathbf{z} = f_\theta(\mathbf{x})$, a positive $\mathbf{v} = f_\theta(\tilde{\mathbf{x}})$, and negatives $\{\mathbf{w}_j\}_{j=1}^N$. Define the contrastive set $\mathcal{C}(\mathbf{z}) := \{\mathbf{v}\} \cup \{\mathbf{w}_j\}_{j=1}^N$. The gradient of the log-partition function $\log Z_{\mathcal{B}}(\mathbf{z}) = \log \sum_{\mathbf{w} \in \mathcal{C}(\mathbf{z})} \exp(s(\mathbf{z}, \mathbf{w})/\tau)$ is given by the softmax-weighted sum of the inner gradients (see e.g. [p. 74]boyd2004convex). Since $\kappa_\tau = \exp(s/\tau) > 0$, we may differentiate $\log Z_{\mathcal{B}}$ and write

$$\nabla_\theta \log Z_{\mathcal{B}}(\mathbf{z}) = \sum_{\mathbf{w} \in \mathcal{C}(\mathbf{z})} \sigma_{\mathcal{B}}(\mathbf{w}) \nabla_\theta \log \kappa_\tau(\mathbf{z}, \mathbf{w}) = \sum_{\mathbf{w} \in \mathcal{C}(\mathbf{z})} \sigma_{\mathcal{B}}(\mathbf{w}) \alpha_\theta(\mathbf{z}, \mathbf{w}), \quad (17)$$

where

$$\sigma_{\mathcal{B}}(\mathbf{w}) := \frac{\kappa(\mathbf{z}, \mathbf{w})}{Z_{\mathcal{B}}(\mathbf{z})} \quad \text{satisfies} \quad \sigma_{\mathcal{B}}(\mathbf{w}) \geq 0, \quad \sum_{\mathbf{w} \in \mathcal{C}(\mathbf{z})} \sigma_{\mathcal{B}}(\mathbf{w}) = 1.$$

Therefore, using Eq. (16),

$$\|\nabla_\theta \log Z_{\mathcal{B}}(\mathbf{z})\| \leq \sum_{\mathbf{w} \in \mathcal{C}(\mathbf{z})} \sigma_{\mathcal{B}}(\mathbf{w}) \|\alpha_\theta(\mathbf{z}, \mathbf{w})\| \leq 2C_s(\tau)C_\Theta \sum_{\mathbf{w} \in \mathcal{C}(\mathbf{z})} \sigma_{\mathcal{B}}(\mathbf{w}) = 2C_s(\tau)C_\Theta. \quad (18)$$

Step 3: Bounding the loss gradient. For a batch \mathcal{B} and anchor $\mathbf{z} = f_\theta(\mathbf{x})$, define the per-batch loss

$$\ell_{\mathcal{B}}(\theta) := -\log \kappa_\tau(\mathbf{z}, \mathbf{v}) + \log Z_{\mathcal{B}}(\mathbf{z}),$$

where $\mathbf{v} = f_\theta(\tilde{\mathbf{x}})$ is the positive match. Since $\nabla_\theta \log \kappa_\tau(\mathbf{z}, \mathbf{v}) = \alpha_\theta(\mathbf{z}, \mathbf{v})$,

$$\nabla_\theta \ell_{\mathcal{B}}(\theta) = -\alpha_\theta(\mathbf{z}, \mathbf{v}) + \nabla_\theta \log Z_{\mathcal{B}}(\mathbf{z}).$$

By the triangle inequality and Eqs. (16) and (18),

$$\|\nabla_\theta \ell_{\mathcal{B}}(\theta)\| \leq \|\alpha_\theta(\mathbf{z}, \mathbf{v})\| + \|\nabla_\theta \log Z_{\mathcal{B}}(\mathbf{z})\| \leq 2C_s(\tau)C_\Theta + 2C_s(\tau)C_\Theta = 4C_s(\tau)C_\Theta. \quad (19)$$

Finally, the population objective is $\mathcal{L}_{\text{NCE}}(\theta) = \mathbb{E}_{\mathcal{B}}[\ell_{\mathcal{B}}(\theta)]$. Since $\ell_{\mathcal{B}}$ is differentiable in θ by Asm. 3.1 for each \mathcal{B} and $\|\nabla_\theta \ell_{\mathcal{B}}(\theta)\| \leq 4C_s(\tau)C_\Theta$ provides an integrable dominating function, we may differentiate under the expectation by dominated convergence, obtaining

$$\nabla_\theta \mathcal{L}_{\text{NCE}}(\theta) = \mathbb{E}_{\mathcal{B}}[\nabla_\theta \ell_{\mathcal{B}}(\theta)].$$

Taking norms and applying Jensen's inequality yields

$$\|\nabla_\theta \mathcal{L}_{\text{NCE}}(\theta)\| \leq \mathbb{E}_{\mathcal{B}}[\|\nabla_\theta \ell_{\mathcal{B}}(\theta)\|] \leq 4C_s(\tau)C_\Theta.$$

Thus, for each fixed $\tau > 0$ and any $N \in \mathbb{N}_+$, the gradient of unimodal InfoNCE defined in Eq. (1) is uniformly bounded over Θ by $C(\tau) := 4C_s(\tau)C_\Theta$. \square

C.1.2. MULTIMODAL OPTIMIZATION STABILITY

Lemma C.2 (Stable multimodal optimization). *Assume Asm. 4.1. Fix any $\tau > 0$ and any $N \in \mathbb{N}_+$. Then the symmetric multimodal loss $\mathcal{L}_{\text{Sym}}(\theta, \phi)$ defined in Eq. (2) has uniformly bounded joint gradient over $\Theta \times \Phi$. Formally, there exists a constant $C(\tau) < \infty$ such that*

$$\|\nabla_{(\theta, \phi)} \mathcal{L}_{\text{Sym}}(\theta, \phi)\| \leq C(\tau), \quad \forall (\theta, \phi) \in \Theta \times \Phi.$$

Proof intuition. This proof extends the uniform gradient bound established for the unimodal case to the dual-encoder, cross-modal setting. The core logic inherits the properties of *atomic smoothness* and the *convex bottleneck* detailed previously, applying them to the joint parameter space (Θ, Φ) . The extension relies on two structural observations:

(i) When evaluating a single contrastive direction (e.g., matching a vision anchor to language keys), the partial gradients with respect to either the anchor network (θ) or the key network (ϕ) behave exactly like the unimodal case. The softmax-weighted denominator ensures the gradient for each individual modality remains strictly bounded.

(ii) The total joint gradient across both modalities is the vector concatenation of the individual θ and ϕ updates. By treating these parameter spaces orthogonally, we can apply the Pythagorean theorem to fuse their separate bounds. Because the symmetric loss is simply the average of two bounded directional losses, the triangle inequality yields one absolute, uniform upper bound for the entire cross-modal objective.

Proof. Step 1: Uniform bounds on components. We retain the bound on the similarity critic sensitivity $C_s(\tau)$ from Eq. (14) in unimodal derivations. For the encoders, we define the uniform bound on the Jacobians over the joint space, which is guaranteed by Asm. 4.1. Let C_Θ and C_Φ be the maximal sensitivities:

$$C_\Theta := \sup_{\theta \in \Theta} \sup_{\mathbf{x} \in \mathcal{X}} \|J_\theta f_\theta(\mathbf{x})\| < \infty, \quad C_\Phi := \sup_{\phi \in \Phi} \sup_{\mathbf{y} \in \mathcal{Y}} \|J_\phi g_\phi(\mathbf{y})\| < \infty.$$

We define the global encoder constant $C_{\text{enc}} := \max(C_\Theta, C_\Phi)$. Consider a generic cross-modal representation pair (\mathbf{z}, \mathbf{w}) where \mathbf{z} depends on θ and \mathbf{w} depends on ϕ . The gradient of the kernel term $\kappa_\tau(\mathbf{z}, \mathbf{w})$ with respect to the joint parameter vector (θ, ϕ) splits into block components. Using Eq. (16), the partial gradients satisfy:

$$\|\nabla_\theta \log \kappa_\tau(\mathbf{z}, \mathbf{w})\| \leq C_s(\tau) C_\Theta \leq C_s(\tau) C_{\text{enc}}, \quad \|\nabla_\phi \log \kappa_\tau(\mathbf{z}, \mathbf{w})\| \leq C_s(\tau) C_\Phi \leq C_s(\tau) C_{\text{enc}}. \quad (20)$$

Step 2: Bounding directional partial derivatives. Define a training batch \mathcal{B} as a collection of $N + 1$ independent pairs: a primary positive pair (\mathbf{x}, \mathbf{y}) and N negative keys $\{\mathbf{y}'_j\}_{j=1}^N$ (and similarly in reverse). The symmetric loss is the average of two directional losses computed on this batch:

$$\ell_{\text{Sym}}(\mathcal{B}) = \frac{1}{2} (\ell_{\theta \rightarrow \phi}(\mathcal{B}) + \ell_{\phi \rightarrow \theta}(\mathcal{B})).$$

By the triangle inequality, the norm of the joint gradient satisfies:

$$\|\nabla_{(\theta, \phi)} \ell_{\text{Sym}}\| \leq \frac{1}{2} \|\nabla_{(\theta, \phi)} \ell_{\theta \rightarrow \phi}\| + \frac{1}{2} \|\nabla_{(\theta, \phi)} \ell_{\phi \rightarrow \theta}\|.$$

We first analyze the forward component $\ell_{\theta \rightarrow \phi}$. Here, \mathbf{x} serves as the anchor, \mathbf{y} as the positive key, and the set $\{\mathbf{y}'_j\}_{j=1}^N$ as the negative keys. The loss is:

$$\ell_{\theta \rightarrow \phi} := -\log \kappa_\tau(f_\theta(\mathbf{x}), g_\phi(\mathbf{y})) + \log \left(\kappa_\tau(f_\theta(\mathbf{x}), g_\phi(\mathbf{y})) + \sum_{j=1}^N \kappa_\tau(f_\theta(\mathbf{x}), g_\phi(\mathbf{y}'_j)) \right).$$

Crucially, the joint gradient vector is the concatenation $\nabla_{(\theta, \phi)} \ell_{\theta \rightarrow \phi} = (\nabla_\theta \ell_{\theta \rightarrow \phi}^\top, \nabla_\phi \ell_{\theta \rightarrow \phi}^\top)^\top$. We bound the partial gradients of $\ell_{\theta \rightarrow \phi}$ with respect to each parameter block separately. Note that the set of key representations in the batch is $\mathcal{C}_\phi = \{g_\phi(\mathbf{y})\} \cup \{g_\phi(\mathbf{y}'_j)\}_{j=1}^N$, and we denote the softmax probability assigned to any key $\mathbf{v} \in \mathcal{C}_\phi$ as $\sigma(\mathbf{v})$.

(i) Gradient with respect to θ (anchor sensitivity): In this direction, θ governs only the anchor $f_\theta(\mathbf{x})$; the keys \mathcal{C}_ϕ are constant. We expand the gradient of the loss as the alignment term plus the gradient of the log-partition function:

$$\nabla_\theta \ell_{\theta \rightarrow \phi} = -\nabla_\theta \log \kappa_\tau(f_\theta(\mathbf{x}), g_\phi(\mathbf{y})) + \sum_{\mathbf{v} \in \mathcal{C}_\phi} \sigma(\mathbf{v}) \nabla_\theta \log \kappa_\tau(f_\theta(\mathbf{x}), \mathbf{v}).$$

Applying the triangle inequality and the uniform sensitivity bound $C_s(\tau)C_\Theta$ derived in Eq. (20):

$$\begin{aligned} \|\nabla_\theta \ell_{\theta \rightarrow \phi}\| &\leq \|\nabla_\theta \log \kappa_\tau(f_\theta(\mathbf{x}), g_\phi(\mathbf{y}))\| + \sum_{\mathbf{v} \in \mathcal{C}_\phi} \sigma(\mathbf{v}) \|\nabla_\theta \log \kappa_\tau(f_\theta(\mathbf{x}), \mathbf{v})\| \\ &\leq C_s(\tau)C_\Theta + C_s(\tau)C_\Theta \sum_{\mathbf{v} \in \mathcal{C}_\phi} \sigma(\mathbf{v}) = 2C_s(\tau)C_\Theta. \quad (\text{Since } \sum_{\mathbf{v} \in \mathcal{C}_\phi} \sigma(\mathbf{v}) = 1) \end{aligned}$$

(ii) Gradient with respect to ϕ (key sensitivity): In this direction, ϕ parametrizes every key in the batch (both positive and negative), while the anchor $f_\theta(\mathbf{x})$ acts as a constant. The gradient is:

$$\nabla_\phi \ell_{\theta \rightarrow \phi} = -\nabla_\phi \log \kappa_\tau(f_\theta(\mathbf{x}), g_\phi(\mathbf{y})) + \sum_{\mathbf{v} \in \mathcal{C}_\phi} \sigma(\mathbf{v}) \nabla_\phi \log \kappa_\tau(f_\theta(\mathbf{x}), \mathbf{v}).$$

Similarly, applying the triangle inequality and the sensitivity bound $C_s(\tau)C_\Phi$:

$$\|\nabla_\phi \ell_{\theta \rightarrow \phi}\| \leq C_s(\tau)C_\Phi + C_s(\tau)C_\Phi \sum_{\mathbf{v} \in \mathcal{C}_\phi} \sigma(\mathbf{v}) = 2C_s(\tau)C_\Phi.$$

Step 3: Global uniform bound. Based on the above analysis, the total gradient magnitude for the forward loss is bounded by the vector norm:

$$\|\nabla_{(\theta, \phi)} \ell_{\theta \rightarrow \phi}\| = \sqrt{\|\nabla_\theta \ell_{\theta \rightarrow \phi}\|^2 + \|\nabla_\phi \ell_{\theta \rightarrow \phi}\|^2} \leq \sqrt{(2C_s(\tau)C_\Theta)^2 + (2C_s(\tau)C_\Phi)^2} \leq 2\sqrt{2}C_s(\tau)C_{\text{enc}}.$$

By symmetry, the exact same bound applies to the backward loss $\ell_{\phi \rightarrow \theta}$. Therefore, the batch loss gradient is bounded by:

$$\|\nabla_{(\theta, \phi)} \ell_{\text{Sym}}\| = \frac{1}{2} \|\nabla_{(\theta, \phi)} \ell_{\theta \rightarrow \phi} + \nabla_{(\theta, \phi)} \ell_{\phi \rightarrow \theta}\| \leq \frac{1}{2} (\|\nabla_{(\theta, \phi)} \ell_{\theta \rightarrow \phi}\| + \|\nabla_{(\theta, \phi)} \ell_{\phi \rightarrow \theta}\|) = 2\sqrt{2}C_s(\tau)C_{\text{enc}}.$$

Since $\|\nabla_{(\theta, \phi)} \ell_{\text{Sym}}(\mathcal{B})\|$ is uniformly bounded and ℓ_{Sym} is differentiable a.e. in (θ, ϕ) , we may differentiate under the expectation by dominated convergence, yielding

$$\|\nabla_{(\theta, \phi)} \mathcal{L}_{\text{Sym}}\| = \|\nabla_{(\theta, \phi)} \mathbb{E}_{\mathcal{B}}[\ell_{\text{Sym}}]\| \leq \mathbb{E}_{\mathcal{B}}[\|\nabla \ell_{\text{Sym}}\|] \leq 2\sqrt{2}C_s(\tau)C_{\text{enc}}.$$

Defining $C := 2\sqrt{2}C_s(\tau)C_{\text{enc}} < \infty$, the gradient is uniformly bounded over $\Theta \times \Phi$. \square

C.2. Sharp-peak Smoothing Implies Vanishing KDE Mismatch

The large-batch parametric energy $\mathcal{J}_\tau(\theta)$ depends on the *kernel-smoothed* density $\tilde{\rho}_{\theta, \tau}$ through the cross-entropy term $H_\times(q_\theta, \tilde{\rho}_{\theta, \tau})$, whereas the intrinsic functional $\mathcal{F}_{\tau, U_\theta}$ is expressed in terms of the *true* density ρ_θ and its entropy $H(\rho_\theta)$. To compare $\mathcal{J}_\tau(\theta)$ with $\mathcal{F}_{\tau, U_\theta}(\rho_\theta)$ in Thm. 3.2, we therefore require a quantitative control of the bias introduced by smoothing, i.e., that $\tilde{\rho}_{\theta, \tau}$ approximates ρ_θ when the kernel is sufficiently sharp.

Lemma C.3 (Vanishing KDE error under sharp peak). *Assume Asms. 2.1, 3.1 and 3.2. Fix $\theta \in \Theta$ and assume $q_\theta \ll \mu$ with a continuous density ρ_θ bounded away from zero, i.e. $\inf_{\mathbf{z} \in \mathcal{Z}} \rho_\theta(\mathbf{z}) > \underline{\rho}_\theta > 0$. Define the KDE mismatch $\varepsilon_{\text{kde}}^{(\theta)}(\tau) := \|\tilde{\rho}_{\theta, \tau} - \rho_\theta\|_\infty$, where $\tilde{\rho}_{\theta, \tau}$ is the kernel-smoothed density (Def. 2.2). Then, as $\tau \rightarrow 0^+$, $\varepsilon_{\text{kde}}^{(\theta)}(\tau) \rightarrow 0$.*

Proof intuition. The core objective is to establish that as the temperature τ approaches zero, the kernel-smoothed density $\tilde{\rho}_{\theta, \tau}$ perfectly collapses onto the true continuous density ρ_θ , uniformly across the entire manifold \mathcal{Z} . The intuition relies on two geometric properties:

(i) First, consider how the temperature parameter scales the kernel. The similarity critic is defined to have a sharp, unique peak when a representation is compared to itself. As $\tau \rightarrow 0^+$, the exponential nature of the kernel drastically exaggerates this peak, effectively morphing the kernel into a Dirac delta function. The probability mass assigned to any representation even slightly separated from the target decays exponentially fast. Simultaneously, the compact geometry of the manifold guarantees there is always a stable, non-vanishing volume of space immediately surrounding the target, ensuring the local density does not collapse to zero.

(ii) Second, because the true density ρ_θ is continuous on a compact manifold, it is uniformly continuous—it cannot exhibit infinitely steep cliffs or discontinuous jumps. At near-zero temperatures, the smoothed density $\tilde{\rho}_{\theta,\tau}(\mathbf{z})$ evaluates a weighted average using almost exclusively the points infinitesimally close to \mathbf{z} . Within this microscopic neighborhood, the true density is essentially flat. The distant regions of the manifold, where the true density might differ wildly, are completely muted by the vanishing tail of the kernel. Consequently, the local weighted average perfectly aligns with the true local density, driving the maximum global estimation error to zero.

Proof. Fix any $\theta \in \Theta$. Let $d_{\mathcal{Z}}(\cdot, \cdot)$ denote the geodesic distance on the compact Riemannian manifold \mathcal{Z} as in Asm. 3.2. Since \mathcal{Z} is compact and ρ_θ is continuous, ρ_θ is bounded. Define the normalized kernel

$$\bar{\kappa}_\tau(\mathbf{z}, \mathbf{w}) := \frac{\kappa_\tau(\mathbf{z}, \mathbf{w})}{V_\kappa(\tau)}.$$

We first show that $\bar{\kappa}_\tau$ concentrates near the diagonal $\{\mathbf{z} = \mathbf{w}\}$ as $\tau \rightarrow 0^+$, and then prove Lem. C.3.

Step 1: Uniform concentration of $\bar{\kappa}_\tau$ near the diagonal. Fix any $\delta \in (0, r)$, where r is from Asm. 3.2, and define

$$\mathcal{A}_\delta := \{(\mathbf{z}, \mathbf{w}) \in \mathcal{Z} \times \mathcal{Z} : d_{\mathcal{Z}}(\mathbf{z}, \mathbf{w}) \geq \delta\}.$$

By compactness of \mathcal{Z} , the set \mathcal{A}_δ is compact. Since s is continuous by Asm. 3.1, consider the continuous function

$$g(\mathbf{z}, \mathbf{w}) := s(\mathbf{z}, \mathbf{z}) - s(\mathbf{z}, \mathbf{w}).$$

By Asm. 3.2, for each fixed $\mathbf{z} \in \mathcal{Z}$ the map $\mathbf{w} \mapsto s(\mathbf{z}, \mathbf{w})$ has a unique maximizer at $\mathbf{w} = \mathbf{z}$; hence $g(\mathbf{z}, \mathbf{w}) > 0$ whenever $d_{\mathcal{Z}}(\mathbf{z}, \mathbf{w}) \geq \delta$. Therefore g is strictly positive on \mathcal{A}_δ , and by compactness it attains a strictly positive minimum:

$$m_\delta := \min_{(\mathbf{z}, \mathbf{w}) \in \mathcal{A}_\delta} g(\mathbf{z}, \mathbf{w}) > 0.$$

Equivalently, for all $\mathbf{z} \in \mathcal{Z}$ and all $\mathbf{w} \in \mathcal{Z}$ with $d_{\mathcal{Z}}(\mathbf{z}, \mathbf{w}) \geq \delta$,

$$s(\mathbf{z}, \mathbf{w}) \leq s(\mathbf{z}, \mathbf{z}) - m_\delta. \tag{21}$$

Fix $\eta \in (0, \delta)$. Let $\mathbb{B}_l(\mathbf{z}) := \{\mathbf{w} \in \mathcal{Z} \mid d_{\mathcal{Z}}(\mathbf{z}, \mathbf{w}) < l\}$ denote an open ball with radius l . By the compactness of \mathcal{Z} , any open cover of \mathcal{Z} has a finite subcover. Consider the open cover given by $\{\mathbb{B}_{\eta/2}(\mathbf{z}) \mid \mathbf{z} \in \mathcal{Z}\}$. We can extract a finite subcover, meaning there exist points $\{\mathbf{z}_1, \dots, \mathbf{z}_M\} \subset \mathcal{Z}$ such that

$$\mathcal{Z} = \bigcup_{j=1}^M \mathbb{B}_{\eta/2}(\mathbf{z}_j).$$

For any arbitrary point $\mathbf{z} \in \mathcal{Z}$, the properties of the cover guarantee there exists at least one index $i \in \{1, \dots, M\}$ such that $\mathbf{z} \in \mathbb{B}_{\eta/2}(\mathbf{z}_i)$. Now, choose any point $\mathbf{w} \in \mathbb{B}_{\eta/2}(\mathbf{z}_i)$. By the triangle inequality

$$d_{\mathcal{Z}}(\mathbf{z}, \mathbf{w}) \leq d_{\mathcal{Z}}(\mathbf{z}_i, \mathbf{w}) + d_{\mathcal{Z}}(\mathbf{z}_i, \mathbf{z}).$$

Since both \mathbf{z} and \mathbf{w} are points of the open ball $\mathbb{B}_{\eta/2}(\mathbf{z}_i)$, we have strict inequalities $d_{\mathcal{Z}}(\mathbf{z}_i, \mathbf{w}) < \eta/2$ and $d_{\mathcal{Z}}(\mathbf{z}_i, \mathbf{z}) < \eta/2$. Combining this with the triangle inequality, we have:

$$d_{\mathcal{Z}}(\mathbf{z}, \mathbf{w}) < \frac{\eta}{2} + \frac{\eta}{2} = \eta \implies \mathbf{w} \in \mathbb{B}_\eta(\mathbf{z}).$$

This establishes $\mathbb{B}_{\eta/2}(\mathbf{z}_i) \subseteq \mathbb{B}_\eta(\mathbf{z})$. By the monotonicity of measures, applying μ yields

$$\mu(\mathbb{B}_\eta(\mathbf{z})) \geq \mu(\mathbb{B}_{\eta/2}(\mathbf{z}_i)).$$

Since this holds for the specific i associated with the arbitrary point \mathbf{z} , the measure is bounded below by the minimum across all M patches:

$$\mu(\mathbb{B}_\eta(\mathbf{z})) \geq \min_{1 \leq j \leq M} \mu(\mathbb{B}_{\eta/2}(\mathbf{z}_j)) =: b_\eta > 0.$$

where positivity $b_\eta > 0$ holds because μ has full support on the manifold.

Now, let $\delta \in (0, r)$ be as above and choose $\eta \in (0, \delta)$ so that

$$m_2 \eta^2 < m_\delta, \quad (22)$$

where m_2 is the constant in Asm. 3.2. This is possible since $m_\delta > 0$. Then, for $\mathbf{w} \in \mathbb{B}_\eta(\mathbf{z}) \subset \mathbb{B}_r(\mathbf{z})$, the lower quadratic bound in Asm. 3.2 gives

$$s(\mathbf{z}, \mathbf{w}) \geq s(\mathbf{z}, \mathbf{z}) - m_2 d_{\mathcal{Z}}(\mathbf{z}, \mathbf{w})^2 \geq s(\mathbf{z}, \mathbf{z}) - m_2 \eta^2,$$

so

$$\kappa_\tau(\mathbf{z}, \mathbf{w}) \geq \exp(s(\mathbf{z}, \mathbf{z})/\tau) \exp(-m_2 \eta^2/\tau).$$

Integrating over $\mathbb{B}_\eta(\mathbf{z})$ and using $\mu(\mathbb{B}_\eta(\mathbf{z})) \geq b_\eta$ yields the uniform lower bound

$$V_\kappa(\tau) = \int_{\mathcal{Z}} \kappa_\tau(\mathbf{z}, \mathbf{w}) d\mu(\mathbf{w}) \geq b_\eta \exp(s(\mathbf{z}, \mathbf{z})/\tau) \exp(-m_2 \eta^2/\tau). \quad (23)$$

Here, by Asm. 2.1, $V_\kappa(\tau)$ is independent of \mathbf{z} . (The factor $\exp(s(\mathbf{z}, \mathbf{z})/\tau)$ cancels in the ratio below.)

Next, for $\mathbf{w} \notin \mathbb{B}_\delta(\mathbf{z})$ we have $d_{\mathcal{Z}}(\mathbf{z}, \mathbf{w}) \geq \delta$, so by Eq. (21),

$$\kappa_\tau(\mathbf{z}, \mathbf{w}) = \exp(s(\mathbf{z}, \mathbf{w})/\tau) \leq \exp(s(\mathbf{z}, \mathbf{z})/\tau) \exp(-m_\delta/\tau).$$

Therefore, with $V_\mu := \mu(\mathcal{Z}) < \infty$,

$$\int_{\mathcal{Z} \setminus \mathbb{B}_\delta(\mathbf{z})} \kappa_\tau(\mathbf{z}, \mathbf{w}) d\mu(\mathbf{w}) \leq V_\mu \exp(s(\mathbf{z}, \mathbf{z})/\tau) \exp(-m_\delta/\tau). \quad (24)$$

Dividing Eq. (24) by Eq. (23) and using Eq. (22) yields, uniformly in \mathbf{z} ,

$$\int_{\mathcal{Z} \setminus \mathbb{B}_\delta(\mathbf{z})} \bar{\kappa}_\tau(\mathbf{z}, \mathbf{w}) d\mu(\mathbf{w}) \leq \frac{V_\mu}{b_\eta} \exp\left(-\frac{m_\delta - m_2 \eta^2}{\tau}\right) \xrightarrow{\tau \rightarrow 0^+} 0. \quad (25)$$

Step 2: Sup-norm convergence of the smoothing. Fix $\varepsilon > 0$. Since ρ_θ is continuous on compact \mathcal{Z} , it is uniformly continuous. By uniform continuity in \mathbf{z} of ρ_θ for each fixed $\theta \in \Theta$, choose $\delta \in (0, r)$ such that

$$|\rho_\theta(\mathbf{w}) - \rho_\theta(\mathbf{z})| \leq \varepsilon \quad \text{whenever} \quad d_{\mathcal{Z}}(\mathbf{z}, \mathbf{w}) < \delta.$$

For any $\mathbf{z} \in \mathcal{Z}$, write

$$\tilde{\rho}_{\theta, \tau}(\mathbf{z}) - \rho_\theta(\mathbf{z}) = \int_{\mathcal{Z}} \bar{\kappa}_\tau(\mathbf{z}, \mathbf{w}) (\rho_\theta(\mathbf{w}) - \rho_\theta(\mathbf{z})) d\mu(\mathbf{w}),$$

and split the integral over $\mathbb{B}_\delta(\mathbf{z})$ and its complement. Using $\int_{\mathcal{Z}} \bar{\kappa}_\tau(\mathbf{z}, \mathbf{w}) d\mu(\mathbf{w}) = 1$, the bound on $\mathbb{B}_\delta(\mathbf{z})$, and $|\rho_\theta(\mathbf{w}) - \rho_\theta(\mathbf{z})| \leq 2\|\rho_\theta\|_\infty$ everywhere, we obtain

$$|\tilde{\rho}_{\theta, \tau}(\mathbf{z}) - \rho_\theta(\mathbf{z})| \leq \varepsilon + 2\|\rho_\theta\|_\infty \int_{\mathcal{Z} \setminus \mathbb{B}_\delta(\mathbf{z})} \bar{\kappa}_\tau(\mathbf{z}, \mathbf{w}) d\mu(\mathbf{w}).$$

By the boundedness of ρ_θ , taking the supremum over $\mathbf{z} \in \mathcal{Z}$ and invoking Eq. (25) gives

$$\limsup_{\tau \rightarrow 0^+} \|\tilde{\rho}_{\theta, \tau} - \rho_\theta\|_\infty \leq \varepsilon.$$

Since $\varepsilon > 0$ is arbitrary, and by the non-negativity of norm, $\liminf_{\tau \rightarrow 0^+} \|\tilde{\rho}_{\theta, \tau} - \rho_\theta\|_\infty \geq 0$. Therefore, for each fixed $\theta \in \Theta$,

$$\varepsilon_{\text{kde}}^{(\theta)}(\tau) := \|\tilde{\rho}_{\theta, \tau} - \rho_\theta\|_\infty \xrightarrow{\tau \rightarrow 0^+} 0$$

□

C.3. Unimodal Parametric Inheritance and Emergence of Uniformity

This subsection formalizes the intuition used in § 3.2: unimodal InfoNCE inherits the single-well intrinsic geometry when (i) the kernel smoothing bias is small and (ii) the encoder family is expressive enough to (approximately) realize the intrinsic Gibbs equilibrium at the best attainable potential level.

Recap of objects. Fix $\tau > 0$. For each $\theta \in \Theta$, recall the induced representation law $q_\theta \in \mathcal{P}(\mathcal{Z})$ and encoded positive-pair law $\pi_{\theta\theta} \in \mathcal{P}(\mathcal{Z} \times \mathcal{Z})$. Under the same setting of Thm. 3.2, assume $q_\theta \ll \mu$ and write $\rho_\theta := dq_\theta/d\mu$. Let U_θ be the alignment potential field induced by $\pi_{\theta\theta}$ (Def. 3.1). The intrinsic functional is $\mathcal{F}_{\tau, U_\theta}(\rho)$ (Eq. (5)), and the parametric energy is $\mathcal{J}_\tau(\theta)$ (Def. 3.2).

Free-energy gap equals KL divergence. From Prop. 3.1, for any fixed potential U and temperature τ , define the partition function

$$Z_\tau := \int_{\mathcal{Z}} \exp(-U(\mathbf{z})/\tau) d\mu(\mathbf{z}), \quad (26)$$

and the associated Gibbs density

$$\rho^*(\mathbf{z}) := \frac{\exp(-U(\mathbf{z})/\tau)}{Z_\tau}. \quad (27)$$

Then for any $\rho \in \mathcal{P}_\mu(\mathcal{Z})$ with $\rho \log(\rho/\rho^*) \in L^1(\mu)$,

$$\mathcal{F}_{\tau, U}(\rho) + \log Z_\tau = \tau D_{\text{KL}}(\rho \parallel \rho^*) \geq 0. \quad (28)$$

In particular, ρ^* is the unique minimizer of $\mathcal{F}_{\tau, U}$ and the free-energy suboptimality controls proximity to the Gibbs equilibrium via KL divergence.

Remark C.1 (Proof of Eq. (28)). Expanding $D_{\text{KL}}(\rho \parallel \rho^*) = \int_{\mathcal{Z}} \rho \log(\rho/\rho^*) d\mu$ and substituting $\log \rho^* = -(U/\tau) - \log Z_\tau$ yields Eq. (28).

Expressivity at the best attainable potential level. The intrinsic minimum of $\mathcal{F}_{\tau, U_\theta}$ equals $-\log Z_{\theta, \tau}$ by Eq. (28), where $Z_{\theta, \tau} = \int_{\mathcal{Z}} \exp(-U_\theta(\mathbf{z})/\tau) d\mu(\mathbf{z})$ is the normalization constant of the Gibbs density. We therefore define the *best attainable potential level* at temperature τ as any

$$\hat{\theta} \in \arg \min_{\theta \in \Theta} \left(-\log Z_{\theta, \tau} \right). \quad (29)$$

Assumption C.1 (Expressivity at the best level). There exists a function $\varepsilon_{\text{real}}(\tau) \rightarrow 0$ as $\tau \rightarrow 0^+$ such that for $\hat{\theta}$ in Eq. (29),

$$\mathcal{F}_{\tau, U_{\hat{\theta}}}(\rho_{\hat{\theta}}) + \log Z_{\hat{\theta}, \tau} \leq \varepsilon_{\text{real}}(\tau). \quad (30)$$

Equivalently, $\rho_{\hat{\theta}}$ is an $\varepsilon_{\text{real}}(\tau)$ -approximate minimizer of the intrinsic functional associated with the best attainable potential level.

Ground-state inheritance under encoder expressivity. Under Asm. 3.2 and mild regularity conditions, Thm. 3.2 bounds the gap between $\mathcal{J}_\tau(\theta)$ and $\mathcal{F}_{\tau, U_\theta}(\rho_\theta)$ by KDE mismatch $\varepsilon_{\text{kde}}^{(\theta)}(\tau)$ vanishing as $\tau \rightarrow 0^+$. Furthermore, for a sufficiently expressive encoder family, we establish the following parametric inheritance of the intrinsic ground-state:

Corollary C.1 (Unimodal parametric inheritance under expressivity). *Assume the conditions of Thm. 3.2 hold for $\theta^* \in \arg \min_{\theta \in \Theta} \mathcal{J}_\tau(\theta)$ and for $\hat{\theta}$ in Eq. (29). Assume additionally the expressivity condition Asm. C.1. Fix $\sigma > 0$ and define the σ -ground-state set of U_{θ^*} by*

$$\mathcal{W}_{\theta^*}^\sigma := \{\mathbf{z} \in \mathcal{Z} : U_{\theta^*}(\mathbf{z}) \leq \text{ess inf}_\mu U_{\theta^*} + \sigma\}.$$

Then, as $\tau \rightarrow 0^+$, the learned measure q_{θ^} concentrates on $\mathcal{W}_{\theta^*}^\sigma$ in the sense that for every open $\mathcal{O} \subset \mathcal{Z}$ with $\mathcal{O} \supset \mathcal{W}_{\theta^*}^\sigma$, $q_{\theta^*}(\mathcal{Z} \setminus \mathcal{O}) \rightarrow 0$.*

Proof intuition. The core objective is to show that a fully optimized encoder (θ^*) acts like a cooling thermodynamic system. As $\tau \rightarrow 0^+$, its representations inevitably collapse into the lowest-energy valleys of its alignment potential landscape (the ground state $\mathcal{W}_{\theta^*}^\sigma$). The proof unfolds in three conceptual phases:

(i) For any induced potential field U_θ , the ideal representation distribution is the Gibbs equilibrium (ρ_θ^*). We first establish

a fundamental identity: the gap between the encoder’s actual free energy and the absolute minimum possible free energy exactly equals the KL divergence between the learned distribution and this ideal Gibbs state.

(ii) By our expressivity assumption, the best possible theoretical encoder ($\hat{\theta}$) can arbitrarily approach its own thermodynamic limit. Since the optimized encoder θ^* minimizes the empirical loss, its performance must be at least as good as $\hat{\theta}$ ’s. This ”squeezes” the actual energy gap to zero, forcing the KL divergence between the learned distribution ρ_{θ^*} and its ideal Gibbs state $\rho_{\hat{\theta}^*}$ to vanish as $\tau \rightarrow 0^+$.

(iii) With the KL divergence vanishing, Pinsker’s inequality guarantees the Total Variation distance also drops to zero, making the distributions statistically indistinguishable. From Prop. 3.2, a true Gibbs distribution concentrates entirely inside the lowest-energy valleys as the temperature drops. By tracking this Gibbs state, the representations must identically collapse into this σ -ground-state.

Proof. Step 1: Well-defined “best achievable” equilibrium. We first isolate the intrinsic quantity that governs the “best achievable” equilibrium value at temperature τ . Fix any $\theta \in \Theta$ and $\tau > 0$. By Asm. 2.1, \mathcal{Z} is compact with $\mu(\mathcal{Z}) < \infty$; and by Asm. 3.1, $s : \mathcal{Z} \times \mathcal{Z} \rightarrow \mathbb{R}$ is continuous. Then, by the extreme value theorem, s is bounded on $\mathcal{Z} \times \mathcal{Z}$:

$$S_{\max} := \max_{\mathbf{z}, \mathbf{w} \in \mathcal{Z}} s(\mathbf{z}, \mathbf{w}) < \infty.$$

The induced alignment potential field (Def. 3.1) is $U_{\theta}(\mathbf{z}) = -\int_{\mathcal{Z}} s(\mathbf{z}, \mathbf{w}) d\nu_{\theta, \mathbf{z}}(\mathbf{w})$, hence $U_{\theta}(\mathbf{z}) \geq -S_{\max}$ for all \mathbf{z} . Therefore, for any fixed $\tau > 0$,

$$0 < \exp\left(-\frac{U_{\theta}(\mathbf{z})}{\tau}\right) \leq \exp\left(\frac{S_{\max}}{\tau}\right) \quad \text{for all } \mathbf{z} \in \mathcal{Z},$$

and thus

$$0 < Z_{\theta, \tau} := \int_{\mathcal{Z}} \exp\left(-\frac{U_{\theta}(\mathbf{z})}{\tau}\right) d\mu(\mathbf{z}) \leq \mu(\mathcal{Z}) \exp\left(\frac{S_{\max}}{\tau}\right) < \infty.$$

Thus, the representational energy $\mathcal{F}_{\tau, U_{\theta}}(\rho) = \frac{1}{\tau} \int_{\mathcal{Z}} U_{\theta} \rho d\mu - H(\rho)$ admits the unique Gibbs minimizer $\rho_{\theta}^* \propto e^{-U_{\theta}/\tau}$ (Prop. 3.1). The corresponding minimum is

$$\inf_{\rho \in \mathcal{P}(\mathcal{Z})} \mathcal{F}_{\tau, U_{\theta}}(\rho) = \mathcal{F}_{\tau, U_{\theta}}(\rho_{\theta}^*) = -\log Z_{\theta, \tau}, \quad Z_{\theta, \tau} := \int_{\mathcal{Z}} \exp\left(-\frac{U_{\theta}(\mathbf{z})}{\tau}\right) d\mu(\mathbf{z}). \quad (31)$$

We interpret $-\log Z_{\theta, \tau}$ as the lowest representation energy level induced by the potential field U_{θ} , which is the best intrinsic value attainable by any density in $\mathcal{P}_{\mu}(\mathcal{Z})$ once U_{θ} is fixed.

Step 2: Representation energy gap equals a KL-divergence. Fix θ and τ . Recall that, by Prop. 3.1, the unique Gibbs equilibrium is

$$\rho_{\theta}^*(\mathbf{z}) = \frac{\exp(-U_{\theta}(\mathbf{z})/\tau)}{Z_{\theta, \tau}},$$

we have the pointwise identity

$$\log \rho_{\theta}^*(\mathbf{z}) = -\frac{U_{\theta}(\mathbf{z})}{\tau} - \log Z_{\theta, \tau}.$$

Define the KL divergence $D_{\text{KL}}(\rho_{\theta} \parallel \rho_{\theta}^*)$. Applying Eq. (28) with $\rho = \rho_{\theta}$ and $\rho^* = \rho_{\theta}^*$ yields

$$D_{\text{KL}}(\rho_{\theta} \parallel \rho_{\theta}^*) = \mathcal{F}_{\tau, U_{\theta}}(\rho_{\theta}) + \log Z_{\theta, \tau}.$$

Finally, by Eq. (31), $\inf_{\rho \in \mathcal{P}(\mathcal{Z})} \mathcal{F}_{\tau, U_{\theta}}(\rho) = \mathcal{F}_{\tau, U_{\theta}}(\rho_{\theta}^*) = -\log Z_{\theta, \tau}$, hence

$$\mathcal{F}_{\tau, U_{\theta}}(\rho_{\theta}) - \inf_{\rho \in \mathcal{P}(\mathcal{Z})} \mathcal{F}_{\tau, U_{\theta}}(\rho) = \mathcal{F}_{\tau, U_{\theta}}(\rho_{\theta}) + \log Z_{\theta, \tau} = D_{\text{KL}}(\rho_{\theta} \parallel \rho_{\theta}^*). \quad (32)$$

Step 3: Transfer ground-state concentration to ρ_{θ^*} . Define the approximation error

$$\eta_{\tau}(\theta) := |\mathcal{J}_{\tau}(\theta) - \mathcal{F}_{\tau, U_{\theta}}(\rho_{\theta})|,$$

which satisfies $\eta_\tau(\theta) \rightarrow 0$ for each fixed $\theta \in \Theta$ as $\tau \rightarrow 0^+$, by Thm. 3.2. Let $\theta^* \in \arg \min_{\theta \in \Theta} \mathcal{J}_\tau(\theta)$, and let $\hat{\theta} \in \arg \min_{\theta \in \Theta} (-\log Z_{\theta, \tau})$ as defined in Eq. (29). By optimality, $\mathcal{J}_\tau(\theta^*) \leq \mathcal{J}_\tau(\hat{\theta})$, hence

$$\mathcal{F}_{\tau, U_{\theta^*}}(\rho_{\theta^*}) \leq \mathcal{J}_\tau(\theta^*) + \eta_\tau(\theta^*) \leq \mathcal{J}_\tau(\hat{\theta}) + \eta_\tau(\theta^*) \leq \mathcal{F}_{\tau, U_{\hat{\theta}}}(\rho_{\hat{\theta}}) + \eta_\tau(\theta^*) + \eta_\tau(\hat{\theta}).$$

Adding $\log Z_{\theta^*, \tau}$ and using $\log Z_{\theta^*, \tau} \leq \log Z_{\hat{\theta}, \tau}$ by definition of $\hat{\theta}$, we obtain

$$\begin{aligned} \mathcal{F}_{\tau, U_{\theta^*}}(\rho_{\theta^*}) + \log Z_{\theta^*, \tau} &\leq \mathcal{F}_{\tau, U_{\hat{\theta}}}(\rho_{\hat{\theta}}) + \log Z_{\theta^*, \tau} + \eta_\tau(\theta^*) + \eta_\tau(\hat{\theta}) \\ &\leq \mathcal{F}_{\tau, U_{\hat{\theta}}}(\rho_{\hat{\theta}}) + \log Z_{\hat{\theta}, \tau} + \eta_\tau(\theta^*) + \eta_\tau(\hat{\theta}). \end{aligned}$$

Substituting Eq. (30) yields

$$\mathcal{F}_{\tau, U_{\theta^*}}(\rho_{\theta^*}) + \log Z_{\theta^*, \tau} \leq \varepsilon_{\text{real}}(\tau) + \eta_\tau(\theta^*) + \eta_\tau(\hat{\theta}).$$

Invoking Eq. (32) at $\theta = \theta^*$ yields

$$D_{\text{KL}}(\rho_{\theta^*} \parallel \rho_{\theta^*}^*) \leq \varepsilon_{\text{real}}(\tau) + \eta_\tau(\theta^*) + \eta_\tau(\hat{\theta}) \xrightarrow{\tau \rightarrow 0^+} 0.$$

Hence, by Pinsker's inequality,

$$\|\rho_{\theta^*} - \rho_{\theta^*}^*\|_{\text{TV}} \leq \sqrt{\frac{1}{2} D_{\text{KL}}(\rho_{\theta^*} \parallel \rho_{\theta^*}^*)} \xrightarrow{\tau \rightarrow 0^+} 0. \quad (33)$$

Now fix any open set $\mathcal{O} \subset \mathcal{Z}$ with $\mathcal{O} \supset \mathcal{W}_{\theta^*}^\sigma$, where $\mathcal{W}_{\theta^*}^\sigma := \{\mathbf{z} \in \mathcal{Z} \mid U_{\theta^*}(\mathbf{z}) \leq \text{ess inf}_\mu U_{\theta^*} + \sigma\}$ with any fixed $\sigma > 0$. Applying Prop. 3.2 to the potential U_{θ^*} gives the Gibbs concentration

$$(\rho_{\theta^*}^* \mu)(\mathcal{Z} \setminus \mathcal{O}) \xrightarrow{\tau \rightarrow 0^+} 0.$$

Finally, by the variational characterization of total variation, for any measurable $\mathcal{A} \subseteq \mathcal{Z}$,

$$|q_{\theta^*}(\mathcal{A}) - \rho_{\theta^*}^* \mu(\mathcal{A})| \leq \|\rho_{\theta^*} - \rho_{\theta^*}^*\|_{\text{TV}}.$$

Taking $\mathcal{A} = \mathcal{Z} \setminus \mathcal{O}$ and combining with Eq. (33) yields

$$q_{\theta^*}(\mathcal{Z} \setminus \mathcal{O}) \leq (\rho_{\theta^*}^* \mu)(\mathcal{Z} \setminus \mathcal{O}) + \|\rho_{\theta^*} - \rho_{\theta^*}^*\|_{\text{TV}} \xrightarrow{\tau \rightarrow 0^+} 0,$$

which is the desired ground-state concentration. \square

Remark C.2 (Why this implies uniformity is a tie-breaker). Inside the aligned basin $\{\mathbf{z} : U_\theta(\mathbf{z}) \approx \text{ess inf}_\mu U_\theta\}$, the potential term in $\mathcal{F}_{\tau, U_\theta}$ is nearly constant. In that regime, minimizing $\mathcal{F}_{\tau, U_\theta}$ reduces (approximately) to maximizing entropy subject to remaining constraints imposed by the encoder family, so the selected configuration is the most internally dispersed distribution compatible with being well-aligned. This is the precise sense in which ‘‘uniformity’’ in unimodal contrastive learning is not a competing global force but an entropic tie-breaker within the alignment basin.

C.4. Multimodal Parametric Inheritance

This subsection formalizes the sense in which the practical multimodal energy $\mathcal{J}_\tau^{\text{Sym}}(\theta, \phi)$ inherits the intrinsic barrier-driven geometry of $\mathcal{F}_{\tau, U}^{\text{Sym}}$ when the encoder family is sufficiently expressive. Concretely, fixing one modality (say ϕ), we show that if the image encoder family can realize (up to a vanishing gap) the intrinsic best response against the peer density, then any parametric minimizer concentrates its *excess* mass near minimizers of the effective barrier potential $V_{\theta|\phi} = \frac{1}{\tau} U_{\theta+\phi} + \log \rho_\phi$.

Background-plus-excess decomposition. Given a density floor $\underline{\rho} > 0$ with $\underline{\rho} \mu(\mathcal{Z}) < 1$, any feasible density can be decomposed as

$$\rho(\mathbf{z}) = \underline{\rho} + M_{\text{ex}} \bar{\rho}(\mathbf{z}), \quad M_{\text{ex}} := 1 - \underline{\rho} \mu(\mathcal{Z}), \quad \bar{\rho} \geq 0, \quad \int_{\mathcal{Z}} \bar{\rho} d\mu = 1.$$

Here $\underline{\rho}$ plays the role of a fixed background mass and $\bar{\rho} = (\rho - \underline{\rho})/M_{\text{ex}}$ is the normalized distribution of the remaining excess budget M_{ex} .

Corollary C.2 (Multimodal parametric inheritance under model expressivity). *Assume the setting of Thm. 4.2. Fix a peer encoder $\phi \in \Phi$ and, for each $\tau > 0$, let $\theta^* \in \arg \min_{\theta \in \Theta} \mathcal{J}_\tau^{\text{Sym}}(\theta, \phi)$. Write the density floors parameterized by θ^* as $\underline{\rho}_{\theta^*}$ with $\underline{\rho}_{\theta^*} \mu(\mathcal{Z}) < 1$, and define set of strictly positive μ -densities bounded lower by $\underline{\rho}_{\theta^*}$ as*

$$\mathcal{P}_{\mu, \underline{\rho}_{\theta^*}}(\mathcal{Z}) := \{\rho \in L^1(\mathcal{Z}) : \rho \geq \underline{\rho}_{\theta^*} \mu\text{-a.e.}, \int_{\mathcal{Z}} \rho d\mu = 1\},$$

and the excess mass $M_{\text{ex}}^{(\theta^*)} := 1 - \underline{\rho}_{\theta^*} \mu(\mathcal{Z})$. Define the normalized excess density as $\bar{\rho}_{\theta^*}(\mathbf{z}) := (\rho_{\theta^*}(\mathbf{z}) - \underline{\rho}_{\theta^*})/M_{\text{ex}}^{(\theta^*)}$. Further, assume the encoder family $\{f_\theta\}_\Theta$ is sufficiently expressive: $\exists \varepsilon_{\text{real}}(\tau) \rightarrow 0$ as $\tau \downarrow 0^+$ such that

$$\mathcal{F}_{\tau, \mathbf{U}_{\theta^*}, \phi}^{\text{Sym}}(\rho_{\theta^*}, \rho_\phi) \leq \inf_{\rho \in \mathcal{P}_{\mu, \underline{\rho}_{\theta^*}}(\mathcal{Z})} \mathcal{F}_{\tau, \mathbf{U}_{\theta^*}, \phi}^{\text{Sym}}(\rho, \rho_\phi) + \varepsilon_{\text{real}}(\tau). \quad (34)$$

Let $V_{\theta^*|\phi}(\mathbf{z}) := \frac{1}{\tau} U_{\theta^*|\phi}(\mathbf{z}) + \log \rho_\phi(\mathbf{z})$ be the effective potential field parameterized by (θ^*, ϕ) . For $\sigma > 0$, define $\mathcal{W}_{\theta^*}^\sigma := \{\mathbf{z} \in \mathcal{Z} : V_{\theta^*|\phi}(\mathbf{z}) \leq \text{ess inf}_\mu V_{\theta^*|\phi} + \sigma\}$. Then, for every $\sigma > 0$,

$$\bar{\rho}_{\theta^*} \mu(\mathcal{Z} \setminus \mathcal{W}_{\theta^*}^\sigma) \leq 2 \varepsilon_{\text{real}}(\tau) / (\sigma M_{\text{ex}}^{(\theta^*)}). \quad (35)$$

Moreover, as $\tau \downarrow 0^+$, if the expressivity condition satisfies $\varepsilon_{\text{real}}(\tau)/\sigma \rightarrow 0$ for any $\sigma \downarrow 0$, we have $\bar{\rho}_{\theta^*} \mu(\mathcal{Z} \setminus \mathcal{W}_{\theta^*}^\sigma) \rightarrow 0$. A symmetric statement holds for optimizing in ϕ with θ fixed.

Proof intuition. The proof proceeds by decoupling the induced density ρ_{θ^*} into a fixed background floor $\underline{\rho}_{\theta^*}$ and a free excess mass $M_{\text{ex}}^{(\theta^*)}$. By the expressivity assumption, the parameterized model can closely approach the true coordinate infimum of the intrinsic functional. We construct a sequence of boundary competitors that concentrate all their excess mass strictly inside the sublevel sets of the effective barrier potential $V_{\theta^*|\phi}$, driving the cross-entropy term toward its absolute lower bound $\log \underline{\rho}_{\theta^*}$. By comparing the energy of the parameterized density against these optimal competitors, we show that any excess mass placed outside the sublevel set $\mathcal{W}_{\theta^*}^\sigma$ incurs a strict linear energy penalty. The expressivity gap $\varepsilon_{\text{real}}(\tau)$ bounds this penalty, directly restricting the fraction of excess mass that can "leak" outside the ground state.

Proof. We provide the derivation for the modality \mathcal{X} with parameter $\theta \in \Theta$. The corresponding result for $\phi \in \Phi$ follows by interchanging modalities and notation.

Fix $\phi \in \Phi$ and $\tau > 0$, and let $\theta^* \in \arg \min_{\theta \in \Theta} \mathcal{J}_\tau^{\text{Sym}}(\theta, \phi)$. Since $\rho_{\theta^*} \geq \underline{\rho}_{\theta^*} \mu$ -a.e., $M_{\text{ex}}^{(\theta^*)} = 1 - \underline{\rho}_{\theta^*} \mu(\mathcal{Z}) > 0$, and $\int_{\mathcal{Z}} \rho_{\theta^*} d\mu = 1$, we have $\bar{\rho}_{\theta^*} \geq 0 \mu$ -a.e. and

$$\int_{\mathcal{Z}} \bar{\rho}_{\theta^*} d\mu = (1 - \underline{\rho}_{\theta^*} \mu(\mathcal{Z})) / M_{\text{ex}}^{(\theta^*)} = 1,$$

hence $\bar{\rho}_{\theta^*} \mu$ is a valid probability measure.

Define the effective potential field and its essential infimum

$$V_{\theta^*|\phi}(\mathbf{z}) = \frac{1}{\tau} U_{\theta^*|\phi}(\mathbf{z}) + \log \rho_\phi(\mathbf{z}), \quad v_* := \text{ess inf}_\mu V_{\theta^*|\phi},$$

and for $\sigma > 0$ the sublevel set is $\mathcal{W}_{\theta^*}^\sigma = \{\mathbf{z} \in \mathcal{Z} : V_{\theta^*|\phi}(\mathbf{z}) \leq v_* + \sigma\}$.

Step 1: A quantitative implication of near-optimality. Consider the coordinate functional with the peer encoder ϕ fixed

$$\mathcal{F}_\tau(\rho) := \mathcal{F}_{\tau, \mathbf{U}_{\theta^*}, \phi}^{\text{Sym}}(\rho, q_\phi), \quad \rho \in \mathcal{P}_{\mu, \underline{\rho}_{\theta^*}}(\mathcal{Z}).$$

As made explicit in the proof of Prop. 4.1 by expanding $\mathcal{F}_{\tau, \mathbf{U}_{\theta^*}, \phi}^{\text{Sym}}$ and collecting ρ -dependent terms, \mathcal{F}_τ can be written in the form

$$\mathcal{F}_\tau(\rho) = \frac{1}{2} \int_{\mathcal{Z}} V_{\theta^*|\phi}(\mathbf{z}) \rho(\mathbf{z}) d\mu(\mathbf{z}) + \frac{1}{2} \int_{\mathcal{Z}} q_\phi(\mathbf{z}) \log \rho(\mathbf{z}) d\mu(\mathbf{z}) + \text{const}_\tau(\phi), \quad (36)$$

where $\text{const}_\tau(\phi)$ is independent of ρ . By the floor constraint $\rho \geq \underline{\rho}_{\theta^*} \mu$ -a.e., the monotonicity of the logarithm, and the fact that ρ_ϕ is a probability density ($\int_{\mathcal{Z}} \rho_\phi d\mu = 1$), we have

$$\int_{\mathcal{Z}} \rho_\phi \log \rho d\mu \geq \int_{\mathcal{Z}} \rho_\phi \log \underline{\rho}_{\theta^*} d\mu = \log \underline{\rho}_{\theta^*}.$$

Hence, for any $\rho \in \mathcal{P}_{\mu, \underline{\rho}_{\theta^*}}(\mathcal{Z})$,

$$\mathcal{F}_\tau(\rho) \geq \frac{1}{2} \int_{\mathcal{Z}} V_{\theta^*|\phi} \rho \, d\mu + \frac{1}{2} \log \underline{\rho}_{\theta^*} + \text{const}_\tau(\phi). \quad (37)$$

Let

$$\mathcal{F}_\tau^* := \inf_{\rho \in \mathcal{P}_{\mu, \underline{\rho}_{\theta^*}}(\mathcal{Z})} \mathcal{F}_\tau(\rho).$$

Applying Prop. 4.1 (with density floor $\underline{\rho} = \underline{\rho}_{\theta^*}$) to \mathcal{F}_τ yields, for each $\delta > 0$, a boundary competitor $\rho^{(\delta)} \in \mathcal{P}_{\mu, \underline{\rho}_{\theta^*}}(\mathcal{Z})$ whose excess mass is supported on a shrinking set $\mathcal{S}^\delta \subseteq \mathcal{W}_{\theta^*}^\delta$ with $\mu(\mathcal{S}^\delta) \xrightarrow{\delta \rightarrow 0} 0$, such that $\mathcal{F}_\tau(\rho^{(\delta)}) \rightarrow \mathcal{F}_\tau^*$ as $\delta \rightarrow 0$.

Moreover, since $\rho^{(\delta)} = \underline{\rho}_{\theta^*}$ on $\mathcal{Z} \setminus \mathcal{S}^\delta$ and ρ_ϕ is continuous on compact \mathcal{Z} , we have

$$\begin{aligned} \int_{\mathcal{Z}} \rho_\phi \log \rho^{(\delta)} \, d\mu &= \log \underline{\rho}_{\theta^*} + \int_{\mathcal{S}^\delta} \rho_\phi \log \left(1 + \frac{M_{\text{ex}}^{(\theta^*)}}{\underline{\rho}_{\theta^*} \mu(\mathcal{S}^\delta)} \right) \, d\mu \\ &\leq \log \underline{\rho}_{\theta^*} + \|\rho_\phi\|_\infty \mu(\mathcal{S}^\delta) \log \left(1 + \frac{c}{\mu(\mathcal{S}^\delta)} \right) \\ &= \log \underline{\rho}_{\theta^*} + o_\delta(1), \end{aligned}$$

where $o_\delta(1) \rightarrow 0$ as $\delta \rightarrow 0$ because $\mu(\mathcal{S}^\delta) \log(1/\mu(\mathcal{S}^\delta)) \rightarrow 0$. In addition, since $\rho^{(\delta)} - \underline{\rho}_{\theta^*}$ places all excess mass inside $\{\mathbf{z} \in \mathcal{Z} : V_{\theta^*|\phi}(\mathbf{z}) \leq v_* + \delta\}$,

$$\begin{aligned} \int_{\mathcal{Z}} V_{\theta^*|\phi} \rho^{(\delta)} \, d\mu &= \underline{\rho}_{\theta^*} \int_{\mathcal{Z}} V_{\theta^*|\phi} \, d\mu + M_{\text{ex}}^{(\theta^*)} \int_{\mathcal{Z}} V_{\theta^*|\phi} \bar{\rho}^{(\delta)} \, d\mu \\ &\leq \underline{\rho}_{\theta^*} \int_{\mathcal{Z}} V_{\theta^*|\phi} \, d\mu + M_{\text{ex}}^{(\theta^*)} (v_* + \delta), \end{aligned}$$

where $\bar{\rho}^{(\delta)} := (\rho^{(\delta)} - \underline{\rho}_{\theta^*})/M_{\text{ex}}^{(\theta^*)}$.

Plugging these bounds into Eq. (36) and letting $\delta \rightarrow 0$ yields the upper bound

$$\mathcal{F}_\tau^* \leq \frac{1}{2} \left(\underline{\rho}_{\theta^*} \int_{\mathcal{Z}} V_{\theta^*|\phi} \, d\mu + M_{\text{ex}}^{(\theta^*)} v_* \right) + \frac{1}{2} \log \underline{\rho}_{\theta^*} + \text{const}_\tau(\phi). \quad (38)$$

Now apply Eq. (37) to $\rho = \rho_{\theta^*}$ and subtract Eq. (38). Using

$$\int_{\mathcal{Z}} V_{\theta^*|\phi} \rho_{\theta^*} \, d\mu = \underline{\rho}_{\theta^*} \int_{\mathcal{Z}} V_{\theta^*|\phi} \, d\mu + M_{\text{ex}}^{(\theta^*)} \int_{\mathcal{Z}} V_{\theta^*|\phi} \bar{\rho}_{\theta^*} \, d\mu.$$

we obtain

$$\mathcal{F}_\tau(\rho_{\theta^*}) - \mathcal{F}_\tau^* \geq \frac{M_{\text{ex}}^{(\theta^*)}}{2} \int_{\mathcal{Z}} (V_{\theta^*|\phi}(\mathbf{z}) - v_*) \bar{\rho}_{\theta^*}(\mathbf{z}) \, d\mu(\mathbf{z}). \quad (39)$$

Step 2: Use expressivity and convert to leakage. By the expressivity assumption in Eq. (34),

$$\mathcal{F}_\tau(\rho_{\theta^*}) \leq \mathcal{F}_\tau^* + \varepsilon_{\text{real}}(\tau).$$

Combining with Eq. (39) gives

$$\int_{\mathcal{Z}} (V_{\theta^*|\phi} - v_*) \bar{\rho}_{\theta^*} \, d\mu \leq \frac{2 \varepsilon_{\text{real}}(\tau)}{M_{\text{ex}}^{(\theta^*)}}. \quad (40)$$

Finally, since $V_{\theta^*|\phi}(\mathbf{z}) - v_* \geq \sigma$ μ -a.e. on $\mathcal{Z} \setminus \mathcal{W}_{\theta^*}^\sigma$, we have

$$\int_{\mathcal{Z}} (V_{\theta^*|\phi} - v_*) \bar{\rho}_{\theta^*} \, d\mu \geq \int_{\mathcal{Z} \setminus \mathcal{W}_{\theta^*}^\sigma} (V_{\theta^*|\phi} - v_*) \bar{\rho}_{\theta^*} \, d\mu \geq \sigma \int_{\mathcal{Z} \setminus \mathcal{W}_{\theta^*}^\sigma} \bar{\rho}_{\theta^*} \, d\mu = \sigma \bar{\rho}_{\theta^*} \mu(\mathcal{Z} \setminus \mathcal{W}_{\theta^*}^\sigma),$$

and therefore, by Eq. (40),

$$\bar{\rho}_{\theta^*} \mu(\mathcal{Z} \setminus \mathcal{W}_{\theta^*}^\sigma) \leq \frac{2 \varepsilon_{\text{real}}(\tau)}{\sigma M_{\text{ex}}^{(\theta^*)}},$$

which is exactly Eq. (35). The concluding asymptotic statement follows immediately: if $\sigma \rightarrow 0$ with $\varepsilon_{\text{real}}(\tau)/\sigma \rightarrow 0$, then the right-hand side vanishes and $\bar{\rho}_{\theta^*} \mu(\mathcal{Z} \setminus \mathcal{W}_{\theta^*}^\sigma) \rightarrow 0$ as $\tau \rightarrow 0^+$. \square

D. Proofs of Unimodal Formal Statements

This section provides rigorous proofs for all formal statements concerning our unimodal analysis. Each statement from the main text is restated for self-containment, accompanied by a proof intuition for providing high-level insights.

D.1. Proof of Thm. 3.1

Theorem 3.1 (Large-batch unimodal dynamics). *Consider the unimodal InfoNCE objective $\mathcal{L}_{\text{NCE}}(\theta)$ in Eq. (1) and the parametric energy $\mathcal{J}_\tau(\theta)$ in Def. 3.2. Assume Asms. 2.1 and 3.1. Then, for any fixed $\tau > 0$ and $\theta \in \Theta$, as $N \rightarrow \infty$:*

$$\begin{aligned} |\mathcal{L}_{\text{NCE}}(\theta) - \mathcal{J}_\tau(\theta) - \log(NV_\kappa(\tau))| &\rightarrow 0, \\ \|\nabla_\theta \mathcal{L}_{\text{NCE}}(\theta) - \nabla_\theta \mathcal{J}_\tau(\theta)\| &\rightarrow 0. \end{aligned} \quad (4)$$

Proof intuition. This proof establishes that as the number of negative samples grows infinitely large ($N \rightarrow \infty$), the empirical InfoNCE loss and its gradients perfectly converge to the deterministic, population-level energy functional $\mathcal{J}_\tau(\theta)$. The intuition rests on how the Law of Large Numbers transforms the partition function (i.e., the denominator) of the contrastive loss:

(i) In a finite batch, the positive and negative samples compete inside the denominator. However, as $N \rightarrow \infty$, the single positive sample’s contribution becomes mathematically negligible. Meanwhile, the discrete sum of the N independent negative samples flawlessly approximates the continuous, smoothed density of the entire representation manifold. Consequently, the loss cleanly splits into two decoupled forces: the expected alignment potential pulling positive pairs together, and the population-level cross-entropy pushing representations away from the global background density.

(ii) To guarantee the optimization trajectories match, we analyze the gradients. The derivative of the log-denominator acts as a softmax-weighted average. As the crowd of negatives becomes infinite, the softmax weight assigned to the single positive pair naturally shrinks to zero. Thus, the repulsive “push” from the denominator is dictated entirely by the continuous distribution of negative samples. Because the underlying gradients are strictly bounded, this empirical crowd perfectly tracks the theoretical cross-entropy gradient, making large-batch InfoNCE mathematically equivalent to optimizing the continuous energy landscape.

Proof. Consider a batch \mathcal{B} consisting of a positive pair and N independent negative samples. For a specific anchor $\mathbf{x} \sim p_{\mathbf{x}}$, the batch is constructed as:

$$\mathcal{B} := \{(\mathbf{x}, \tilde{\mathbf{x}}), \mathbf{x}'_1, \dots, \mathbf{x}'_N\},$$

where the positive partner $\tilde{\mathbf{x}}$ is sampled from the positive conditional $r_{\text{um}}(\tilde{\mathbf{x}}|\mathbf{x})$, and the negative samples $\{\mathbf{x}'_j\}_{j=1}^N$ are drawn i.i.d. from the marginal observation distribution $p_{\mathbf{x}}$. Fix any encoder parameter $\theta \in \Theta$, we denote the representations as $\mathbf{z} = f_\theta(\mathbf{x})$, $\mathbf{v} = f_\theta(\tilde{\mathbf{x}})$, and $\mathbf{w}_j = f_\theta(\mathbf{x}'_j)$. The per-batch unimodal InfoNCE loss $\ell_{\mathcal{B}}(\theta; \mathbf{x})$ is defined as:

$$\ell_{\mathcal{B}}(\theta; \mathbf{x}) := -\frac{1}{\tau} s(\mathbf{z}, \mathbf{v}) + \log \underbrace{\left(\kappa_\tau(\mathbf{z}, \mathbf{v}) + \sum_{j=1}^N \kappa_\tau(\mathbf{z}, \mathbf{w}_j) \right)}_{=: Z_{\mathcal{B}}(\mathbf{z})}, \quad (41)$$

where the kernel $\kappa_\tau(\cdot, \cdot) = \exp(s(\cdot, \cdot)/\tau)$ induced by the loss formulation.

Part I. Value consistency. We analyze the asymptotic behavior of the loss as $N \rightarrow \infty$.

Step 1: Isolate the positive bias. First, we decompose the partition sum $Z_{\mathcal{B}}$ inside the logarithm into the positive term and the sum over negatives:

$$Z_{\mathcal{B}} = P + S_N, \quad \text{where } P := \kappa_\tau(\mathbf{z}, \mathbf{v}), \quad S_N := \sum_{j=1}^N \kappa_\tau(\mathbf{z}, \mathbf{w}_j).$$

The logarithmic term $\log Z_{\mathcal{B}}$ becomes:

$$\log Z_{\mathcal{B}} = \log(S_N + P) = \log S_N + \underbrace{\log\left(1 + \frac{P}{S_N}\right)}_{=: \epsilon_N}.$$

Fix $\tau > 0$. Since \mathcal{Z} is compact and s is continuous on $\mathcal{Z} \times \mathcal{Z}$ by Asm. 3.1 (ii), there exist finite constants s_{\min} and s_{\max} such that $s_{\min} \leq s(\mathbf{z}, \mathbf{w}) \leq s_{\max}$ for all $(\mathbf{z}, \mathbf{w}) \in \mathcal{Z} \times \mathcal{Z}$. Consequently, the exponential kernel satisfies the bounds

$$0 < m_\tau := \exp(s_{\min}/\tau) \leq \kappa_\tau(\mathbf{z}, \mathbf{w}) \leq \exp(s_{\max}/\tau) =: M_\tau < \infty.$$

Thus, $m_\tau \leq P \leq M_\tau$ and $Nm_\tau \leq S_N \leq NM_\tau$. Using $\log(1+x) \leq x$ for $x \geq 0$,

$$0 < \epsilon_N = \log\left(1 + \frac{P}{S_N}\right) \leq \frac{P}{S_N} \leq \frac{M_\tau}{Nm_\tau} = O_\tau(N^{-1}).$$

Therefore, for each fixed $\tau > 0$, $\log Z_B = \log S_N + O_\tau(N^{-1})$.

Step 2: Concentration of the negative partition sum. Fix θ and an anchor representation $\mathbf{z} = f_\theta(\mathbf{x})$. For negatives $\mathbf{x}'_j \stackrel{\text{i.i.d.}}{\sim} p_{\mathbf{x}}$, define $\mathbf{w}_j := f_\theta(\mathbf{x}'_j)$ and

$$Y_j(\mathbf{z}) := \kappa_\tau(\mathbf{z}, \mathbf{w}_j), \quad S_N(\mathbf{z}) := \sum_{j=1}^N Y_j(\mathbf{z}).$$

For fixed \mathbf{z} , the variables $\{Y_j(\mathbf{z})\}_{j=1}^N$ are i.i.d. with mean

$$\mu_\kappa(\mathbf{z}) := \mathbb{E}[Y_1(\mathbf{z}) \mid \mathbf{z}] = \int_{\mathcal{Z}} \kappa_\tau(\mathbf{z}, \mathbf{w}) dq_\theta(\mathbf{w}) \equiv \Gamma_{\theta, \tau}(\mathbf{z}) \geq m_\tau,$$

and variance $\sigma_\kappa^2(\mathbf{z}) := \text{Var}(Y_1(\mathbf{z}) \mid \mathbf{z}) < \infty$. Moreover, for each fixed $\tau > 0$, κ_τ is bounded on $\mathcal{Z} \times \mathcal{Z}$, so $Y_j(\mathbf{z})$ is bounded and hence sub-Gaussian. By Hoeffding's inequality, the sample mean concentrates:

$$\frac{S_N(\mathbf{z})}{N} - \mu_\kappa(\mathbf{z}) = O_p(N^{-1/2}).$$

Equivalently, writing

$$\frac{S_N(\mathbf{z})}{N\mu_\kappa(\mathbf{z})} = 1 + \Delta_N(\mathbf{z}), \quad \Delta_N(\mathbf{z}) = O_p(N^{-1/2}),$$

and noting $\mu_\kappa(\mathbf{z}) > 0$ since $\kappa_\tau > 0$, we can expand the logarithm with the Taylor expansion $\log(1+x) = x + O(x^2)$ and $\Delta_N(\mathbf{z}) = o_p(1)$:

$$\log S_N(\mathbf{z}) = \log(N\mu_\kappa(\mathbf{z})) + \log(1 + \Delta_N(\mathbf{z})) = \log N + \log \Gamma_{\theta, \tau}(\mathbf{z}) + O_p(N^{-1/2}),$$

Therefore,

$$\log S_N(\mathbf{z}) = \log N + \log \Gamma_{\theta, \tau}(\mathbf{z}) + O_p(N^{-1/2}).$$

Step 3: Identification of the induced parametric energy. Combining Steps 1–2, for an anchor $\mathbf{z} = f_\theta(\mathbf{x})$ we have

$$\log Z_B(\mathbf{z}) = \log N + \log \Gamma_{\theta, \tau}(\mathbf{z}) + o_p(1),$$

where $o_p(1)$ denotes a term vanishing in probability as $N \rightarrow \infty$ (for fixed $\tau > 0$). Substituting into Eq. (41) yields the per-batch expansion

$$\ell_B(\theta; \mathbf{x}) = -\frac{1}{\tau} s(\mathbf{z}, \mathbf{v}) + \log N + \log \Gamma_{\theta, \tau}(\mathbf{z}) + o_p(1). \quad (42)$$

Taking expectations over the batch construction $(\mathbf{x}, \tilde{\mathbf{x}}) \sim r_{\text{um}}$ and i.i.d. negatives, and using $\mathcal{L}_{\text{NCE}}(\theta) = \mathbb{E}[\ell_B(\theta; \mathbf{x})]$, we obtain

$$\mathcal{L}_{\text{NCE}}(\theta) = \mathbb{E}_{(\mathbf{x}, \tilde{\mathbf{x}})} \left[-\frac{1}{\tau} s(f_\theta(\mathbf{x}), f_\theta(\tilde{\mathbf{x}})) \right] + \mathbb{E}_{\mathbf{x}} [\log \Gamma_{\theta, \tau}(f_\theta(\mathbf{x}))] + \log N + o(1), \quad (43)$$

where $o(1) \rightarrow 0$ as $N \rightarrow \infty$.

By disintegration of $\pi_{\theta\theta} = (f_\theta \times f_\theta)_{\#} r_{\text{um}}$, define $U_\theta(\mathbf{z}) = -\int_{\mathcal{Z}} s(\mathbf{z}, \mathbf{w}) d\nu_{\mathbf{z}}(\mathbf{w})$. Then the law of iterated expectations gives

$$\mathbb{E}_{(\mathbf{x}, \tilde{\mathbf{x}})} \left[-\frac{1}{\tau} s(\mathbf{z}, \mathbf{v}) \right] = \frac{1}{\tau} \mathbb{E}_{\mathbf{z} \sim q_\theta} [U_\theta(\mathbf{z})] = \frac{1}{\tau} \int_{\mathcal{Z}} U_\theta(\mathbf{z}) dq_\theta(\mathbf{z}) \quad (44)$$

Since $\mathbf{z} = f_\theta(\mathbf{x}) \sim q_\theta$, we can rewrite

$$\mathbb{E}_{\mathbf{x}}[\log \Gamma_{\theta,\tau}(f_\theta(\mathbf{x}))] = \mathbb{E}_{\mathbf{z} \sim q_\theta}[\log \Gamma_{\theta,\tau}(\mathbf{z})].$$

Under the constant kernel-volume condition Asm. 2.1, $\tilde{\rho}_{\theta,\tau}(\mathbf{z}) = \Gamma_{\theta,\tau}(\mathbf{z})/V_\kappa(\tau)$ (Def. 2.2), hence

$$\mathbb{E}_{\mathbf{z} \sim q_\theta}[\log \Gamma_{\theta,\tau}(\mathbf{z})] = \log V_\kappa(\tau) + \mathbb{E}_{\mathbf{z} \sim q_\theta}[\log \tilde{\rho}_{\theta,\tau}(\mathbf{z})] = \log V_\kappa(\tau) - H_\times(q_\theta, \tilde{\rho}_{\theta,\tau}), \quad (45)$$

where $H_\times(q_\theta, \tilde{\rho}_{\theta,\tau}) := -\mathbb{E}_{q_\theta}[\log \tilde{\rho}_{\theta,\tau}]$ is the cross-entropy of q_θ against $\tilde{\rho}_{\theta,\tau}$.

Substituting Eqs. (44) and (45) into Eq. (43) yields

$$\begin{aligned} \mathcal{L}_{\text{NCE}}(\theta) &= \frac{1}{\tau} \int_{\mathcal{Z}} U_\theta(\mathbf{z}) dq_\theta(\mathbf{z}) - H_\times(q_\theta, \tilde{\rho}_{\theta,\tau}) + \log(NV_\kappa(\tau)) + o(1) \\ &= \mathcal{J}_\tau(\theta) + \log(NV_\kappa(\tau)) + o(1). \end{aligned}$$

Since θ is arbitrarily chosen from Θ and Θ is compact by Asm. 3.1, this proves the value-consistency $|\mathcal{L}_{\text{NCE}}(\theta) - \mathcal{J}_\tau(\theta) - \log(NV_\kappa(\tau))| \rightarrow 0$ of Thm. 3.1 for any fixed $\theta \in \Theta$.

Part II. Gradient consistency. We now analyze the gradient dynamics of the batch loss $\ell_{\mathcal{B}}(\theta; \mathbf{x})$. Fix $\tau > 0$ in the limit of $N \rightarrow \infty$. Differentiating Eq. (42) with respect to θ yields

$$\nabla_\theta \ell_{\mathcal{B}}(\theta; \mathbf{x}) = -\frac{1}{\tau} \nabla_\theta s(\mathbf{z}, \mathbf{v}) + \nabla_\theta \log Z_{\mathcal{B}}(\mathbf{z}), \quad Z_{\mathcal{B}}(\mathbf{z}) = \mathbf{P} + \mathbf{S}_N, \quad (46)$$

where $\mathbf{P} := \kappa_\tau(\mathbf{z}, \mathbf{v})$ and $\mathbf{S}_N := \sum_{j=1}^N \kappa_\tau(\mathbf{z}, \mathbf{w}_j)$.

Step 1: Reducing the positive term in the log-partition gradient. Let

$$\mathbf{g}_N(\mathbf{z}) := \nabla_\theta \log(\mathbf{P} + \mathbf{S}_N), \quad \mathbf{r}_N(\mathbf{z}) := \nabla_\theta \log \mathbf{S}_N.$$

Then

$$\begin{aligned} \mathbf{g}_N - \mathbf{r}_N &= \nabla_\theta \log(\mathbf{P} + \mathbf{S}_N) - \nabla_\theta \log \mathbf{S}_N \\ &= \frac{\nabla_\theta \mathbf{P} + \nabla_\theta \mathbf{S}_N}{\mathbf{P} + \mathbf{S}_N} - \frac{\nabla_\theta \mathbf{S}_N}{\mathbf{S}_N} \\ &= \frac{\nabla_\theta \mathbf{P}}{\mathbf{P} + \mathbf{S}_N} + \nabla_\theta \mathbf{S}_N \left(\frac{\mathbf{S}_N - (\mathbf{P} + \mathbf{S}_N)}{\mathbf{S}_N(\mathbf{P} + \mathbf{S}_N)} \right) \\ &= \frac{\nabla_\theta \mathbf{P}}{\mathbf{P} + \mathbf{S}_N} - \frac{\mathbf{P}}{\mathbf{S}_N(\mathbf{P} + \mathbf{S}_N)} \nabla_\theta \mathbf{S}_N. \end{aligned} \quad (47)$$

Under Asm. 3.1, the continuity of s on the compact domain $\mathcal{Z} \times \mathcal{Z}$ ensures the kernel κ_τ is uniformly bounded. Furthermore, expanding $\nabla_\theta \kappa_\tau$ via the chain rule yields a product of terms—specifically the kernel, the similarity critic gradient, and the encoder Jacobian—that are all uniformly bounded by assumption. Thus, for any fixed $\tau > 0$, there exist finite constants M_τ, G_τ such that $0 < \kappa_\tau \leq M_\tau$ and $\|\nabla_\theta \kappa_\tau\| \leq G_\tau$. Moreover, since κ_τ is continuous and strictly positive on the compact $\mathcal{Z} \times \mathcal{Z}$, it attains a positive minimum $m_\tau > 0$. Hence

$$\mathbf{P} \leq M_\tau, \quad \|\nabla_\theta \mathbf{P}\| \leq G_\tau, \quad \mathbf{S}_N \geq Nm_\tau, \quad \text{and} \quad \|\nabla_\theta \mathbf{S}_N\| \leq NG_\tau.$$

Taking norms in Eq. (47) and using these bounds gives

$$\|\mathbf{g}_N - \mathbf{r}_N\| \leq \frac{G_\tau}{Nm_\tau} + \frac{M_\tau}{(Nm_\tau)^2} \cdot NG_\tau = O(N^{-1}).$$

Therefore,

$$\nabla_\theta \log Z_{\mathcal{B}}(\mathbf{z}) = \nabla_\theta \log \mathbf{S}_N(\mathbf{z}) + O(N^{-1}). \quad (48)$$

Step 2: Consistency of the negative-sum ratio. Write

$$\nabla_\theta \log \mathbf{S}_N(\mathbf{z}) = \frac{\nabla_\theta \mathbf{S}_N(\mathbf{z})}{\mathbf{S}_N(\mathbf{z})} = \frac{\frac{1}{N} \sum_{j=1}^N \nabla_\theta \kappa_\tau(\mathbf{z}, \mathbf{w}_j)}{\frac{1}{N} \sum_{j=1}^N \kappa_\tau(\mathbf{z}, \mathbf{w}_j)}.$$

Conditioning on the anchor \mathbf{z} , the negatives \mathbf{w}_j are i.i.d. with law q_θ , and both $\kappa_\tau(\mathbf{z}, \mathbf{w})$ and $\nabla_\theta \kappa_\tau(\mathbf{z}, \mathbf{w})$ are bounded (by Lem. C.1). Thus by the law of large numbers,

$$\frac{1}{N} \sum_{j=1}^N \kappa_\tau(\mathbf{z}, \mathbf{w}_j) \xrightarrow{P} \Gamma_{\theta, \tau}(\mathbf{z}), \quad \frac{1}{N} \sum_{j=1}^N \nabla_\theta \kappa_\tau(\mathbf{z}, \mathbf{w}_j) \xrightarrow{P} \mathbb{E}_{\mathbf{w} \sim q_\theta} [\nabla_\theta \kappa_\tau(\mathbf{z}, \mathbf{w})].$$

As $q_\theta = (f_\theta)_\# p_{\mathbf{x}}$ and $\sup_{\theta \in \Theta, \mathbf{x} \in \mathcal{X}} \|\nabla_\theta \kappa_\tau(\mathbf{z}, f_\theta(\mathbf{x}))\| < \infty$ by Asm. 3.1, differentiation under the integral sign is justified (e.g., by dominated convergence). Thus, for each fixed \mathbf{z} ,

$$\mathbb{E}_{\mathbf{w} \sim q_\theta} [\nabla_\theta \kappa_\tau(\mathbf{z}, \mathbf{w})] = \mathbb{E}_{\mathbf{x} \sim p_{\mathbf{x}}} [\nabla_\theta \kappa_\tau(\mathbf{z}, f_\theta(\mathbf{x}))] = \nabla_\theta \mathbb{E}_{\mathbf{x} \sim p_{\mathbf{x}}} [\kappa_\tau(\mathbf{z}, f_\theta(\mathbf{x}))] = \nabla_\theta \Gamma_{\theta, \tau}(\mathbf{z}).$$

Since $\Gamma_{\theta, \tau}(\mathbf{z}) \geq m_\tau > 0$, the continuous mapping theorem yields

$$\nabla_\theta \log S_N(\mathbf{z}) \xrightarrow{P} \frac{\nabla_\theta \Gamma_{\theta, \tau}(\mathbf{z})}{\Gamma_{\theta, \tau}(\mathbf{z})} = \nabla_\theta \log \Gamma_{\theta, \tau}(\mathbf{z}). \quad (49)$$

Combining Eqs. (48) and (49) gives

$$\nabla_\theta \log Z_B(\mathbf{z}) \xrightarrow{P} \nabla_\theta \log \Gamma_{\theta, \tau}(\mathbf{z}). \quad (50)$$

Step 3: Passing to the population objective and identifying $\nabla_\theta \mathcal{J}_\tau$. Recall $\mathcal{L}_{\text{NCE}}(\theta) = \mathbb{E}_{\mathcal{B}}[\ell_{\mathcal{B}}(\theta; \mathbf{x})]$ and $\nabla_\theta \mathcal{L}_{\text{NCE}}(\theta) = \mathbb{E}_{\mathcal{B}}[\nabla_\theta \ell_{\mathcal{B}}(\theta; \mathbf{x})]$ by Lem. C.1. From Eq. (46) and Eq. (50), we have the pointwise (in the batch randomness) convergence

$$\nabla_\theta \ell_{\mathcal{B}}(\theta; \mathbf{x}) = -\frac{1}{\tau} \nabla_\theta s(\mathbf{z}, \mathbf{v}) + \nabla_\theta \log Z_B(\mathbf{z}) \xrightarrow{P} -\frac{1}{\tau} \nabla_\theta s(\mathbf{z}, \mathbf{v}) + \nabla_\theta \log \Gamma_{\theta, \tau}(\mathbf{z}).$$

Moreover, by Lem. C.1, $\|\nabla_\theta \ell_{\mathcal{B}}\|$ is uniformly bounded, so we may use dominated convergence together with Eq. (50) to interchange $\lim_{N \rightarrow \infty}$ and expectation:

$$\nabla_\theta \mathcal{L}_{\text{NCE}}(\theta) = \mathbb{E}_{\mathcal{B}}[\nabla_\theta \ell_{\mathcal{B}}(\theta; \mathbf{x})] \rightarrow -\frac{1}{\tau} \mathbb{E}_{r_{\text{um}}}[\nabla_\theta s(f_\theta(\mathbf{x}), f_\theta(\tilde{\mathbf{x}}))] + \mathbb{E}_{\mathbf{x} \sim p_{\mathbf{x}}}[\nabla_\theta \log \Gamma_{\theta, \tau}(f_\theta(\mathbf{x}))]. \quad (\star)$$

We now identify the two terms in (\star) as the gradient of the parametric energy $\mathcal{J}_\tau(\theta)$. Recall that the alignment potential field as a function of θ by

$$\int_{\mathcal{Z}} U_\theta(\mathbf{z}) dq_\theta(\mathbf{z}) := \mathbb{E}_{(\mathbf{x}, \tilde{\mathbf{x}}) \sim r_{\text{um}}}[-s(f_\theta(\mathbf{x}), f_\theta(\tilde{\mathbf{x}}))].$$

Under Asm. 3.1, $\nabla_\theta s$ is bounded on the relevant compact set, so we may differentiate under the expectation to obtain

$$\nabla_\theta \int_{\mathcal{Z}} U_\theta(\mathbf{z}) dq_\theta(\mathbf{z}) = -\mathbb{E}_{r_{\text{um}}}[\nabla_\theta s(f_\theta(\mathbf{x}), f_\theta(\tilde{\mathbf{x}}))].$$

Therefore the first term in (\star) equals $\frac{1}{\tau} \nabla_\theta \int_{\mathcal{Z}} U_\theta(\mathbf{z}) dq_\theta(\mathbf{z})$.

By definition,

$$H_{\times}(q_\theta, \tilde{\rho}_{\theta, \tau}) := -\mathbb{E}_{\mathbf{z} \sim q_\theta}[\log \tilde{\rho}_{\theta, \tau}(\mathbf{z})] = -\mathbb{E}_{\mathbf{x} \sim p_{\mathbf{x}}}[\log \tilde{\rho}_{\theta, \tau}(f_\theta(\mathbf{x}))].$$

Under Asm. 2.1, $\tilde{\rho}_{\theta, \tau}(\mathbf{z}) = \Gamma_{\theta, \tau}(\mathbf{z})/V_\kappa(\tau)$ with $V_\kappa(\tau)$ constant in θ (Def. 2.2). Hence

$$\nabla_\theta H_{\times}(q_\theta, \tilde{\rho}_{\theta, \tau}) = -\mathbb{E}_{\mathbf{x}}[\nabla_\theta \log \tilde{\rho}_{\theta, \tau}(f_\theta(\mathbf{x}))] = -\mathbb{E}_{\mathbf{x}}[\nabla_\theta \log \Gamma_{\theta, \tau}(f_\theta(\mathbf{x}))],$$

where differentiation under the expectation is justified by boundedness of $\nabla_\theta \log \Gamma_{\theta, \tau}(f_\theta(\mathbf{x}))$. Thus the second term in (\star) equals $-\nabla_\theta H_{\times}(q_\theta, \tilde{\rho}_{\theta, \tau})$. This gives

$$\nabla_\theta \mathcal{L}_{\text{NCE}}(\theta) \rightarrow \frac{1}{\tau} \nabla_\theta \int_{\mathcal{Z}} U_\theta(\mathbf{z}) dq_\theta(\mathbf{z}) - \nabla_\theta H_{\times}(q_\theta, \tilde{\rho}_{\theta, \tau}) = \nabla_\theta \mathcal{J}_\tau(\theta),$$

which proves gradient consistency with the cross-entropy-induced energy \mathcal{J}_τ for each fixed $\tau > 0$. Since θ is arbitrarily chosen from Θ , this proves the gradient-consistency $\|\nabla_\theta \mathcal{L}_{\text{NCE}}(\theta) - \nabla_\theta \mathcal{J}_\tau(\theta)\| \rightarrow 0$ of Thm. 3.1. \square

D.2. Proof of Prop. 3.1

Proposition 3.1 (Unique Gibbs equilibrium). *Assume \mathcal{Z} is compact with $\mu(\mathcal{Z}) < \infty$. Fix $\tau > 0$ and let $U : \mathcal{Z} \rightarrow \mathbb{R}$ be measurable and bounded below μ -a.e. Then, $\mathcal{F}_{\tau, U}$ (Eq. (5)) is strictly convex on $\mathcal{P}_\mu(\mathcal{Z})$ and admits a unique minimizer*

$$\rho^*(\mathbf{z}) = \frac{\exp(-U(\mathbf{z})/\tau)}{Z_\tau}, \quad Z_\tau := \int_{\mathcal{Z}} \exp(-U(\mathbf{z})/\tau) d\mu(\mathbf{z}).$$

Proof intuition. The objective of this proof is to demonstrate that the representation energy functional always settles into a single, predictable equilibrium state—the Gibbs distribution. The logic unfolds in three geometric phases: First, we confirm that the space of all valid probability distributions is convex. If you mathematically blend any two valid distributions, the result remains a valid distribution. This establishes a well-behaved, continuous foundation for optimization. Next, we examine the shape of the energy landscape sitting on top of this foundation. The functional consists of two competing forces: a linear binding energy term (which tilts the landscape) and a negative entropy term. Because negative entropy is strictly convex, it forces the entire landscape to curve upward. Combining these creates a strictly convex bowl. A perfect bowl over a convex domain is mathematically guaranteed to have exactly one absolute lowest point. Finally, as we are guaranteed a unique global minimum, finding it is just a matter of locating where the functional’s derivative is zero. By applying the calculus of variations—constrained by the requirement that the total probability must sum to 1—we derive the Gibbs distribution (ρ^*). This proves that the system’s absolute ground state perfectly balances the thermodynamic pull toward low-energy regions with the entropic push to remain spread out.

Proof. We analyze the properties of the functional $\mathcal{F}_{\tau,U} : \mathcal{P}_\mu(\mathcal{Z}) \rightarrow \mathbb{R}$ defined on the space of probability densities $\mathcal{P}_\mu(\mathcal{Z}) = \{\rho \in L^1(\mathcal{Z}) : \rho \geq 0 \text{ } \mu\text{-a.e.}, \int_{\mathcal{Z}} \rho \, d\mu = 1\}$. The proof proceeds in three steps: establishing the geometry of the domain, proving the convexity of the energy functional, and deriving the unique minimizer.

Step 1: Convexity of the domain $\mathcal{P}(\mathcal{Z})$. First, we verify that the optimization domain $\mathcal{P}_\mu(\mathcal{Z})$ is a convex set. Consider any two densities $\rho_1, \rho_2 \in \mathcal{P}_\mu(\mathcal{Z})$ and a mixing coefficient $\lambda \in (0, 1)$. Define the interpolation $\rho_\lambda := \lambda\rho_1 + (1 - \lambda)\rho_2$. We observe that ρ_λ satisfies the following two conditions. (i) Non-negativity: Since $\rho_1, \rho_2 \geq 0$ and $\lambda \in (0, 1)$ by construction, $\rho_\lambda \geq 0$ μ -a.e. (ii) Normalization: By the linearity of the integral, $\int_{\mathcal{Z}} \rho_\lambda = \lambda \int_{\mathcal{Z}} \rho_1 \, d\mu + (1 - \lambda) \int_{\mathcal{Z}} \rho_2 \, d\mu = 1$. Therefore, $\rho_\lambda \in \mathcal{P}_\mu(\mathcal{Z})$ for any $\lambda \in (0, 1)$, confirming that the space of valid densities $\mathcal{P}_\mu(\mathcal{Z})$ is a convex set.

Step 2: Strict functional convexity. Let $\rho_1, \rho_2 \in \mathcal{P}_\mu(\mathcal{Z})$ be two distinct densities (i.e., $\rho_1 \not\equiv \rho_2$ almost everywhere) and let $\lambda \in (0, 1)$ be a mixing coefficient. Define the convex combination $\rho_\lambda := \lambda\rho_1 + (1 - \lambda)\rho_2$. We now analyze the two components of $\mathcal{F}_{\tau,U}(\rho_\lambda)$ separately.

In the binding energy term, since $U(\mathbf{z})$ acts as a fixed coefficient relative to ρ for fixed $\tau > 0$, the total binding energy $\frac{1}{\tau} \int_{\mathcal{Z}} U(\mathbf{z})\rho(\mathbf{z}) \, d\mu(\mathbf{z})$ is therefore a linear functional. By the linearity of the Lebesgue integral:

$$\begin{aligned} \frac{1}{\tau} \int_{\mathcal{Z}} U(\mathbf{z})\rho(\mathbf{z}) \, d\mu(\mathbf{z}) &= \frac{1}{\tau} \int_{\mathcal{Z}} (\lambda\rho_1(\mathbf{z}) + (1 - \lambda)\rho_2(\mathbf{z}))U(\mathbf{z}) \, d\mu(\mathbf{z}) \\ &= \frac{\lambda}{\tau} \int_{\mathcal{Z}} \rho_1(\mathbf{z})U(\mathbf{z}) \, d\mu(\mathbf{z}) + \frac{1-\lambda}{\tau} \int_{\mathcal{Z}} \rho_2(\mathbf{z})U(\mathbf{z}) \, d\mu(\mathbf{z}). \end{aligned}$$

The entropy term is $-H(\rho) = \int_{\mathcal{Z}} \rho \log \rho \, d\mu$, with the convention $0 \log 0 = 0$. Since $\phi(t) = t \log t$ is strictly convex on $(0, \infty)$ and convex on $[0, \infty)$, we have

$$\int_{\mathcal{Z}} \phi(\rho_\lambda) \, d\mu < \lambda \int_{\mathcal{Z}} \phi(\rho_1) \, d\mu + (1 - \lambda) \int_{\mathcal{Z}} \phi(\rho_2) \, d\mu$$

whenever $\rho_1 \not\equiv \rho_2$ (i.e., they differ on a set of positive μ -measure). Hence $-H$ is strictly convex on $\mathcal{P}_\mu(\mathcal{Z})$. Combining the two parts:

$$\begin{aligned} \mathcal{F}_{\tau,U}(\rho_\lambda) &= \frac{1}{\tau} \int_{\mathcal{Z}} U(\mathbf{z})\rho(\mathbf{z}) \, d\mu(\mathbf{z}) - H(\rho_\lambda) \\ &< \frac{\lambda}{\tau} \int_{\mathcal{Z}} U(\mathbf{z})\rho_1(\mathbf{z}) \, d\mu(\mathbf{z}) + \frac{1-\lambda}{\tau} \int_{\mathcal{Z}} U(\mathbf{z})\rho_2(\mathbf{z}) \, d\mu(\mathbf{z}) - \lambda H(\rho_1) - (1 - \lambda)H(\rho_2) \\ &= \lambda \mathcal{F}_{\tau,U}(\rho_1) + (1 - \lambda) \mathcal{F}_{\tau,U}(\rho_2). \end{aligned}$$

Therefore, the functional $\mathcal{F}_{\tau,U}(\rho)$ is strictly convex over the space of probability densities $\mathcal{P}_\mu(\mathcal{Z})$.

Step 3: Existence and uniqueness of global minimizer. Since $\mathcal{F}_{\tau,U}(\rho)$ is strictly convex on the convex domain $\mathcal{P}_\mu(\mathcal{Z})$, any local minimizer is the unique global minimizer. For fixed $\tau > 0$, we solve for the optimal density $\rho^* \in \mathcal{P}_\mu(\mathcal{Z})$ using the method of Lagrange multipliers. Define the Lagrangian $\Lambda(\rho, \gamma)$ to enforce the normalization constraint $\int_{\mathcal{Z}} \rho(\mathbf{z}) \, d\mu(\mathbf{z}) = 1$:

$$\Lambda(\rho, \gamma) := \mathcal{F}_{\tau,U}(\rho) + \gamma \left(\int_{\mathcal{Z}} \rho(\mathbf{z}) \, d\mu(\mathbf{z}) - 1 \right).$$

Taking the functional derivative with respect to $\rho(\mathbf{z})$ and setting it to zero:

$$\begin{aligned} \frac{\delta \Lambda}{\delta \rho(\mathbf{z})} &= \int_{\mathcal{Z}} \frac{\delta}{\delta \rho(\mathbf{z})} [\rho(\mathbf{w}) \left(\frac{1}{\tau} U(\mathbf{w}) + \log \rho(\mathbf{w}) + \gamma \right)] d\mu(\mathbf{w}) \\ &= \frac{1}{\tau} U(\mathbf{z}) + \log \rho(\mathbf{z}) + 1 + \gamma. \\ &= 0. \end{aligned}$$

Solving for $\rho^*(\mathbf{z})$:

$$\log \rho^*(\mathbf{z}) = -\frac{U(\mathbf{z})}{\tau} - \gamma - 1 \quad \implies \quad \rho^*(\mathbf{z}) = \frac{1}{\exp(\gamma + 1)} \exp\left(-\frac{U(\mathbf{z})}{\tau}\right),$$

where the first term of the right-hand side is a constant determined by the normalization constraint. Therefore, the unique minimizer is the Gibbs distribution:

$$\rho^*(\mathbf{z}) = \frac{1}{Z_\tau} \cdot \exp\left(-\frac{U(\mathbf{z})}{\tau}\right), \quad \text{where } Z_\tau = \int_{\mathcal{Z}} \exp\left(-\frac{U(\mathbf{z})}{\tau}\right) d\mu(\mathbf{z}).$$

Since $\text{ess inf}_\mu U > -\infty$ by assumption, we have $U(\mathbf{z}) \geq m$ for μ -a.e. \mathbf{z} . Hence

$$0 < Z_\tau = \int_{\mathcal{Z}} e^{-U(\mathbf{z})/\tau} d\mu(\mathbf{z}) \leq e^{-m/\tau} \mu(\mathcal{Z}) < \infty,$$

so ρ^* is well-defined. This confirms that the system admits a unique Gibbs equilibrium characterized by the alignment potential field U . \square

D.3. Proof of Prop. 3.2

Proposition 3.2 (Low-temperature concentration). *In the setting of Prop. 3.1, fix $\sigma > 0$ and define*

$$\mathcal{W}^\sigma := \{\mathbf{z} \in \mathcal{Z} : U(\mathbf{z}) \leq \text{ess inf}_\mu U + \sigma\}.$$

Then as $\tau \rightarrow 0^+$, the Gibbs measure $\rho^(\mathbf{z}) d\mu(\mathbf{z})$ concentrates on \mathcal{W}^σ in the sense that, for every open $\mathcal{O} \supset \mathcal{W}^\sigma$, $\rho^* \mu(\mathcal{Z} \setminus \mathcal{O}) \rightarrow 0$.*

Proof intuition. This proof establishes that as the temperature $\tau \rightarrow 0^+$, the Gibbs distribution entirely collapses into the absolute lowest valleys of the potential landscape (the σ -ground state). The argument relies on a direct comparison of exponential decay rates relative to the minimum energy level m . We evaluate the ratio of probability mass between two distinct regions:

(i) In any region strictly outside the ground state, the potential energy is guaranteed to be at least σ higher than the absolute minimum. Consequently, the total probability mass in this outer region decays exponentially fast, strictly bounded above by a factor of $\exp(-\sigma/\tau)$.

(ii) Conversely, because the true minimum m is defined by the essential infimum, there must exist a pocket of volume near the bottom of the valley where the energy is strictly within $\sigma/2$ of the minimum. The probability mass in this core pocket shrinks much more slowly, strictly bounded below by $\exp(-\sigma/(2\tau))$.

By taking the ratio of these two bounds, we mathematically squeeze the outer probability mass against the inner mass. Because $\exp(-\sigma/\tau)$ decays exponentially faster than $\exp(-\sigma/(2\tau))$, their ratio gets crushed to exactly zero as $\tau \rightarrow 0^+$. This guarantees that no statistical mass can survive outside the lowest-energy valleys, resulting in ground-state concentration.

Proof. We analyze the Gibbs-equilibrium measure $\rho^* \mu$ as $\tau \rightarrow 0^+$. Let

$$m := \text{ess inf}_\mu U \quad \text{and} \quad \mathcal{W}^\sigma := \{\mathbf{z} \in \mathcal{Z} : U(\mathbf{z}) \leq m + \sigma\},$$

for an arbitrarily small but fixed $\sigma > 0$.

Consider any open set $\mathcal{O} \subset \mathcal{Z}$ such that $\mathcal{O} \supset \mathcal{W}^\sigma$, and denote $\mathcal{O}^c := \mathcal{Z} \setminus \mathcal{O}$. Since \mathcal{O} contains \mathcal{W}^σ , its complement satisfies

$$\mathcal{O}^c \subset \{\mathbf{z} \in \mathcal{Z} : U(\mathbf{z}) > m + \sigma\}.$$

Therefore, using the Gibbs distribution $\rho^*(\mathbf{z}) = \frac{1}{Z_\tau} \exp(-U(\mathbf{z})/\tau)$,

$$(\rho^* \mu)(\mathcal{O}^c) = \frac{\int_{\mathcal{O}^c} \exp(-U(\mathbf{z})/\tau) d\mu(\mathbf{z})}{\int_{\mathcal{Z}} \exp(-U(\mathbf{w})/\tau) d\mu(\mathbf{w})}.$$

Multiplying numerator and denominator by $\exp(m/\tau)$ yields

$$(\rho^* \mu)(\mathcal{O}^c) = \frac{\int_{\mathcal{O}^c} \exp(-(U(\mathbf{z}) - m)/\tau) d\mu(\mathbf{z})}{\int_{\mathcal{Z}} \exp(-(U(\mathbf{w}) - m)/\tau) d\mu(\mathbf{w})}.$$

(i) *Numerator bound.* For all $\mathbf{z} \in \mathcal{O}^c$ we have $U(\mathbf{z}) - m \geq \sigma$, hence

$$\int_{\mathcal{O}^c} \exp\left(-\frac{U(\mathbf{z}) - m}{\tau}\right) d\mu(\mathbf{z}) \leq \int_{\mathcal{O}^c} \exp\left(-\frac{\sigma}{\tau}\right) d\mu(\mathbf{z}) = \mu(\mathcal{O}^c) \exp\left(-\frac{\sigma}{\tau}\right).$$

(ii) *Denominator lower bound.* By the definition of $m = \text{ess inf}_\mu U$, for any $\eta > 0$ the set $\{\mathbf{z} \in \mathcal{Z} : U(\mathbf{z}) < m + \eta\}$ has strictly positive μ -measure. Fix $\eta := \sigma/2$ and define

$$\mathcal{A} := \left\{ \mathbf{w} \in \mathcal{Z} \mid U(\mathbf{w}) < m + \sigma/2 \right\}, \quad \text{so that} \quad \mu(\mathcal{A}) > 0.$$

On \mathcal{A} we have $U(\mathbf{w}) - m < \sigma/2$, hence

$$\int_{\mathcal{Z}} \exp\left(-\frac{U(\mathbf{w}) - m}{\tau}\right) d\mu(\mathbf{w}) \geq \int_{\mathcal{A}} \exp\left(-\frac{U(\mathbf{w}) - m}{\tau}\right) d\mu(\mathbf{w}) \geq \mu(\mathcal{A}) \exp\left(-\frac{\sigma}{2\tau}\right).$$

Combining the bounds, we obtain

$$(\rho^* \mu)(\mathcal{O}^c) \leq \frac{\mu(\mathcal{O}^c) \exp(-\sigma/\tau)}{\mu(\mathcal{A}) \exp(-\sigma/(2\tau))} = \frac{\mu(\mathcal{O}^c)}{\mu(\mathcal{A})} \exp\left(-\frac{\sigma}{2\tau}\right).$$

Since $\mu(\mathcal{O}^c) \leq \mu(\mathcal{Z}) < \infty$ and $\mu(\mathcal{A}) > 0$ is fixed, the right-hand side converges to 0 as $\tau \rightarrow 0^+$. Hence, for any open neighborhood $\mathcal{O} \supset \mathcal{W}^\sigma$, we have $(\rho^* \mu)(\mathcal{O}^c) \rightarrow 0$, i.e., the Gibbs measure concentrates in any neighborhood of \mathcal{W}^σ . \square

D.4. Proof of Thm. 3.2

Theorem 3.2 (Low-temperature unimodal energy consistency). *Assume Asms. 2.1, 3.1 and 3.2. Fix $\theta \in \Theta$ and assume $q_\theta \ll \mu$ with a strictly positive, continuous density ρ_θ , i.e., $\inf_{\mathbf{z} \in \mathcal{Z}} \rho_\theta(\mathbf{z}) \geq \underline{\rho}_\theta > 0$.⁵ Define the KDE mismatch $\varepsilon_{\text{kde}}^{(\theta)}(\tau) := \|\tilde{\rho}_{\theta, \tau} - \rho_\theta\|_\infty$. Then, $\exists \tau_0(\theta) > 0$ such that*

$$|\mathcal{J}_\tau(\theta) - \mathcal{F}_{\tau, U_\theta}(\rho_\theta)| \leq 2\varepsilon_{\text{kde}}^{(\theta)}(\tau)/\underline{\rho}_\theta, \quad \forall 0 < \tau \leq \tau_0(\theta),$$

and in particular $|\mathcal{J}_\tau(\theta) - \mathcal{F}_{\tau, U_\theta}(\rho_\theta)| \rightarrow 0$, as $\tau \rightarrow 0^+$.

Proof intuition. The objective of this proof is to establish that at low temperatures, the parametric energy functional $\mathcal{J}_\tau(\theta)$ perfectly mirrors the intrinsic thermodynamic free energy $\mathcal{F}_{\tau, U_\theta}(\rho_\theta)$. The argument hinges on translating their algebraic difference into an information-theoretic distance, and then squeezing that distance to zero.

(i) We first algebraically decompose the parametric energy and reveal a fundamental identity: the exact gap between the learned objective and the theoretical free energy is simply the KL divergence between the true representation density (ρ_θ)

⁵See App. B.3 for a detailed discussion on the strict positivity assumption and the role of density floors.

and its kernel-smoothed counterpart $(\tilde{\rho}_{\theta,\tau})$.

(ii) To prove this KL divergence vanishes, we must ensure the logarithmic ratio inside the integral never explodes. By our assumption, the true density is strictly bounded away from zero. Because Lem. C.3 guarantees the smoothed density tracks the true density as $\tau \rightarrow 0^+$, we mathematically guarantee that the smoothed density also never collapses to zero anywhere on the manifold.

(iii) Because both densities remain safely away from zero, the logarithm operates in a stable, Lipschitz-continuous regime. This allows us to upper-bound the complex integral of the KL divergence directly by the maximum worst-case smoothing error (the KDE mismatch). Since this KDE mismatch vanishes at $\tau \rightarrow 0^+$, the KL divergence is crushed to zero, guaranteeing the parametric and intrinsic energy landscapes become indistinguishable.

Proof. Step 1: Well-posedness of the alignment potential term. Fix any $\theta \in \Theta$. Recall the definition of the alignment potential field (Def. 3.1) by

$$U_\theta(\mathbf{z}) := - \int_{\mathcal{Z}} s(\mathbf{z}, \mathbf{w}) d\nu_{\theta,\mathbf{z}}(\mathbf{w}) \quad \text{for } q_\theta\text{-a.e. } \mathbf{z}.$$

Under Asm. 3.1, the critic s is bounded and Borel measurable, hence U_θ is Borel measurable and bounded, and therefore integrable with respect to q_θ . Moreover, $q_\theta \ll \mu$ with a continuous density ρ_θ bounded away from zero by assumption. Thus, the intrinsic representation functional (Eq. (5))

$$\mathcal{F}_{\tau,U_\theta}(\rho_\theta) := \frac{1}{\tau} \int_{\mathcal{Z}} U_\theta(\mathbf{z}) \rho_\theta(\mathbf{z}) d\mu(\mathbf{z}) - H(\rho_\theta)$$

is well-defined for each $\tau > 0$.

Step 2: Difference reduces to a KL divergence. Recall

$$\mathcal{J}_\tau(\theta) = \frac{1}{\tau} \int_{\mathcal{Z}} U_\theta(\mathbf{z}) dq_\theta(\mathbf{z}) - H_\times(q_\theta, \tilde{\rho}_{\theta,\tau}).$$

Using $H_\times(q, \tilde{\rho}) = H(\rho) + D_{\text{KL}}(\rho \| \tilde{\rho})$ where the density is defined by $\rho := dq/d\mu$, we obtain

$$\mathcal{J}_\tau(\theta) = \frac{1}{\tau} \int_{\mathcal{Z}} U_\theta(\mathbf{z}) \rho_\theta d\mu(\mathbf{z}) - H(\rho_\theta) - D_{\text{KL}}(\rho_\theta \| \tilde{\rho}_{\theta,\tau}),$$

and hence

$$\mathcal{F}_{\tau,U_\theta}(\rho_\theta) - \mathcal{J}_\tau(\theta) = D_{\text{KL}}(\rho_\theta \| \tilde{\rho}_{\theta,\tau}). \quad (51)$$

Step 3: Vanishing KL divergence of the smoothing. Fix any $\theta \in \Theta$. By our initial assumption, the true continuous density is uniformly bounded away from zero, meaning $\inf_{\mathbf{z} \in \mathcal{Z}} \rho_\theta(\mathbf{z}) \geq \underline{\rho}_\theta > 0$. Because this lower bound is strictly positive, the quantity $\underline{\rho}_\theta/2$ is also strictly positive and can serve as an arbitrary error tolerance.

Recall from Lem. C.3 that the KDE mismatch vanishes in the low-temperature limit, i.e., $\lim_{\tau \rightarrow 0^+} \varepsilon_{\text{kde}}^{(\theta)}(\tau) = 0$. By the formal definition of a right-sided limit, applying our chosen tolerance $\underline{\rho}_\theta/2$ guarantees the existence of a critical temperature threshold $\tau_0(\theta) > 0$ such that for all $\tau \leq \tau_0(\theta)$, the smoothing error remains strictly bounded by this tolerance:

$$\varepsilon_{\text{kde}}^{(\theta)}(\tau) := \|\tilde{\rho}_{\theta,\tau} - \rho_\theta\|_\infty \leq \frac{\underline{\rho}_\theta}{2}.$$

Then for all \mathbf{z} ,

$$\tilde{\rho}_{\theta,\tau}(\mathbf{z}) \geq \rho_\theta(\mathbf{z}) - \frac{\underline{\rho}_\theta}{2} \geq \frac{\underline{\rho}_\theta}{2}. \quad (52)$$

On $[\underline{\rho}_\theta/2, \infty)$, the derivative of $\log x$ is $1/x \leq 2/\underline{\rho}_\theta$. Hence for all $a, b > \underline{\rho}_\theta/2$,

$$|\log a - \log b| \leq \frac{2}{\underline{\rho}_\theta} |a - b|.$$

Apply this with $a = \rho_\theta(\mathbf{z})$ and $b = \tilde{\rho}_{\theta,\tau}(\mathbf{z})$. Therefore,

$$\left| \log \frac{\rho_\theta(\mathbf{z})}{\tilde{\rho}_{\theta,\tau}(\mathbf{z})} \right| = |\log \rho_\theta(\mathbf{z}) - \log \tilde{\rho}_{\theta,\tau}(\mathbf{z})| \leq \frac{2}{\rho_\theta} |\rho_\theta(\mathbf{z}) - \tilde{\rho}_{\theta,\tau}(\mathbf{z})| \leq \frac{2\varepsilon_{\text{kde}}^{(\theta)}(\tau)}{\rho_\theta}. \quad (53)$$

Now

$$D_{\text{KL}}(\rho_\theta \| \tilde{\rho}_{\theta,\tau}) = \int_{\mathcal{Z}} \rho_\theta(\mathbf{z}) \log \frac{\rho_\theta(\mathbf{z})}{\tilde{\rho}_{\theta,\tau}(\mathbf{z})} d\mu(\mathbf{z}).$$

Using $\int_{\mathcal{Z}} q_\theta d\mu = 1$ and Eq. (53),

$$D_{\text{KL}}(\rho_\theta \| \tilde{\rho}_{\theta,\tau}) \leq \int_{\mathcal{Z}} \rho_\theta(\mathbf{z}) \left| \log \frac{\rho_\theta(\mathbf{z})}{\tilde{\rho}_{\theta,\tau}(\mathbf{z})} \right| d\mu(\mathbf{z}) \leq \frac{2\varepsilon_{\text{kde}}^{(\theta)}(\tau)}{\rho_\theta}. \quad (54)$$

Substituting this to Eq. (51) yields

$$|\mathcal{J}_\tau(\theta) - \mathcal{F}_{\tau, U_\theta}(\rho_\theta)| \leq \frac{2\varepsilon_{\text{kde}}^{(\theta)}(\tau)}{\rho_\theta}.$$

Finally, Lem. C.3 guarantees that the smoothing error $\varepsilon_{\text{kde}}^{(\theta)}(\tau)$ vanishes in the low-temperature limit. Consequently, $|\mathcal{J}_\tau(\theta) - \mathcal{F}_{\tau, U_\theta}(\rho_\theta)| \xrightarrow{\tau \rightarrow 0^+} 0$, which concludes the proof. \square

E. Proofs of Multimodal Formal Statements

This section provides rigorous proofs for all formal statements concerning our multimodal analysis. Each statement from the main text is restated for self-containment, accompanied by a proof intuition for providing high-level insights.

E.1. Proof of Thm. 4.1

Theorem 4.1 (Large-batch multimodal dynamics). *Consider the multimodal loss $\mathcal{L}_{\text{Sym}}(\theta, \phi)$ in Eq. (2) and the energy $\mathcal{J}_\tau^{\text{Sym}}(\theta, \phi)$ in Def. 4.2. Assume Asms. 2.1 and 4.1. Then, for any fixed $\tau > 0$ and $(\theta, \phi) \in \Theta \times \Phi$, as $N \rightarrow \infty$,*

$$\begin{aligned} |\mathcal{L}_{\text{Sym}}(\theta, \phi) - \mathcal{J}_\tau^{\text{Sym}}(\theta, \phi) - \log(NV_\kappa(\tau))| &\rightarrow 0, \\ \|\nabla_{(\theta, \phi)} \mathcal{L}_{\text{Sym}}(\theta, \phi) - \nabla_{(\theta, \phi)} \mathcal{J}_\tau^{\text{Sym}}(\theta, \phi)\| &\rightarrow 0. \end{aligned}$$

Proof intuition. This proof extends the asymptotic analysis of unimodal InfoNCE to the dual-encoder, cross-modal setting. The logic directly inherits the statistical mechanics of the unimodal proof (Thm. 3.1) but applies them independently across the two modalities:

(i) The symmetric loss is the average of two directional losses (e.g., vision-to-language and language-to-vision). By the Law of Large Numbers, the massive empirical sum of negative keys in each direction independently concentrates around the smoothed continuous density of that specific target modality (e.g., the vision anchors push against the continuous background density of the language representations, and vice versa). This cleanly splits the symmetric objective into a shared attractive alignment potential and two distinct, cross-modal repulsive cross-entropies.

(ii) When calculating the joint gradient, the derivative of the log-denominators acts as a softmax-weighted average. As $N \rightarrow \infty$, the positive pairs' influence on the repulsive forces vanishes. Because the parameter spaces Θ and Φ are orthogonal, the empirical gradient of the massive negative crowd in each direction independently and perfectly tracks its respective continuous cross-entropy gradient. Fusing these orthogonal bounds via the Pythagorean theorem guarantees that descending the empirical cross-modal loss is mathematically equivalent to minimizing the continuous, dual-density energy landscape.

Proof. Consider a batch \mathcal{B} consisting of a positive pair $(\mathbf{x}, \mathbf{y}) \sim r_{\text{mm}}$ together with N i.i.d. negatives $\{\mathbf{y}'_j\}_{j=1}^N \stackrel{\text{i.i.d.}}{\sim} p_{\mathbf{y}}$ and N i.i.d. negatives $\{\mathbf{x}'_j\}_{j=1}^N \stackrel{\text{i.i.d.}}{\sim} p_{\mathbf{x}}$, all independent conditional on (\mathbf{x}, \mathbf{y}) . Write the representations

$$\mathbf{z} = f_\theta(\mathbf{x}), \quad \mathbf{w} = g_\phi(\mathbf{y}), \quad \mathbf{w}'_j = g_\phi(\mathbf{y}'_j), \quad \mathbf{z}'_j = f_\theta(\mathbf{x}'_j),$$

and define the exponential kernel $\kappa_\tau(\cdot, \cdot) = \exp(s(\cdot, \cdot)/\tau)$. Denote the directional partition sums

$$Z_{\mathcal{B}}^{\theta+\phi}(\mathbf{z}) := \kappa_\tau(\mathbf{z}, \mathbf{w}) + \sum_{j=1}^N \kappa_\tau(\mathbf{z}, \mathbf{w}'_j), \quad Z_{\mathcal{B}}^{\phi+\theta}(\mathbf{w}) := \kappa_\tau(\mathbf{z}, \mathbf{w}) + \sum_{j=1}^N \kappa_\tau(\mathbf{z}'_j, \mathbf{w}).$$

The symmetric per-batch loss can be written as

$$\ell_{\mathcal{B}}^{\text{Sym}}(\theta, \phi) = \frac{1}{2} \underbrace{\left(-\frac{1}{\tau} s(\mathbf{z}, \mathbf{w}) + \log Z_{\mathcal{B}}^{\theta+\phi}(\mathbf{z})\right)}_{\ell_{\mathcal{B}}^{x \rightarrow y}(\theta, \phi)} + \frac{1}{2} \underbrace{\left(-\frac{1}{\tau} s(\mathbf{z}, \mathbf{w}) + \log Z_{\mathcal{B}}^{\phi+\theta}(\mathbf{w})\right)}_{\ell_{\mathcal{B}}^{y \rightarrow x}(\theta, \phi)}. \quad (55)$$

Part I. Value consistency. Fix any $\tau > 0$ and $(\theta, \phi) \in \Theta \times \Phi$. We analyze the directional loss $\mathcal{L}_{\text{NCE}}^{x \rightarrow y}(\theta, \phi)$; the reverse direction follows by symmetry. From Eq. (55), the corresponding per-batch directional loss is

$$\ell_{\mathcal{B}}^{x \rightarrow y}(\theta, \phi) := -\frac{1}{\tau} s(\mathbf{z}, \mathbf{w}) + \log Z_{\mathcal{B}}^{\theta+\phi}(\mathbf{z}). \quad (56)$$

Step 1: Bias–variance control of the log-partition term. The structure of $Z_{\mathcal{B}}^{\theta+\phi}$ is identical to the unimodal partition function (Eq. (41)), except that negatives are drawn from q_ϕ rather than q_θ . By assumption, \mathcal{Z} is compact and s is continuous, hence κ_τ is bounded on $\mathcal{Z} \times \mathcal{Z}$ for each fixed $\tau > 0$. Let

$$P := \kappa_\tau(\mathbf{z}, \mathbf{w}), \quad S_N^{\theta+\phi}(\mathbf{z}) := \sum_{j=1}^N \kappa_\tau(\mathbf{z}, \mathbf{w}'_j), \quad Z_{\mathcal{B}}^{\theta+\phi} = P + S_N^{\theta+\phi}.$$

As in Step 1 of the unimodal proof (Part I of Thm. 3.1), the positive contribution induces a vanishing bias:

$$\log(P + S_N^{\theta+\phi}) = \log S_N^{\theta+\phi} + \log\left(1 + \frac{P}{S_N^{\theta+\phi}}\right), \quad \log\left(1 + \frac{P}{S_N^{\theta+\phi}}\right) = O_\tau(N^{-1}).$$

Define the population partition function induced by the target encoder ϕ :

$$\Gamma_{\phi, \tau}(\mathbf{z}) := \mathbb{E}_{\mathbf{w} \sim q_\phi} [\kappa_\tau(\mathbf{z}, \mathbf{w})] = \int_{\mathcal{Z}} \kappa_\tau(\mathbf{z}, \mathbf{w}) dq_\phi(\mathbf{w}).$$

Conditioned on the anchor \mathbf{z} , the terms $\kappa_\tau(\mathbf{z}, \mathbf{w}'_j)$ are i.i.d. and bounded, hence by concentration (cf. Step 2 in Part I of Thm. 3.1)

$$\frac{1}{N} S_N^{\theta+\phi}(\mathbf{z}) = \Gamma_{\phi, \tau}(\mathbf{z}) + O_p(N^{-1/2}),$$

which implies, by the same Taylor expansion used in the unimodal proof, that

$$\log S_N^{\theta+\phi}(\mathbf{z}) = \log N + \log \Gamma_{\phi, \tau}(\mathbf{z}) + O_p(N^{-1/2}).$$

Combining the above displays yields the asymptotic expansion

$$\ell_{\mathcal{B}}^{x \rightarrow y}(\theta, \phi) = -\frac{1}{\tau} s(\mathbf{z}, \mathbf{w}) + \log N + \log \Gamma_{\phi, \tau}(\mathbf{z}) + O_p(N^{-1/2}). \quad (57)$$

Step 2: Identification of the directional energy. Taking expectation of Eq. (57) over the batch construction gives

$$\mathcal{L}_{\text{NCE}}^{x \rightarrow y}(\theta, \phi) := \mathbb{E}_{\mathcal{B}}[\ell_{\mathcal{B}}^{\theta+\phi}(\theta, \phi)] = \mathbb{E}\left[-\frac{1}{\tau} s(\mathbf{z}, \mathbf{w})\right] + \mathbb{E}[\log \Gamma_{\phi, \tau}(\mathbf{z})] + \log N + o(1).$$

Here, since κ_τ is uniformly bounded for fixed τ , the reminder term is uniformly integrable, so taking expectations preserves $o_p(1)$ as $o(1)$. Moreover, $o(1) \rightarrow 0$ as $N \rightarrow \infty$ for fixed $\tau > 0$ by boundedness and dominated convergence.

Now, treating \mathbf{x} (equivalently \mathbf{z}) as the anchor and using the disintegration in Def. 4.1, the law of iterated expectation yields

$$\mathbb{E}_{(\mathbf{x}, \mathbf{y}) \sim r_{\text{mm}}} \left[-\frac{1}{\tau} s(f_\theta(\mathbf{x}), g_\phi(\mathbf{y}))\right] = \frac{1}{\tau} \mathbb{E}_{\mathbf{z} \sim q_\theta} [U_{\theta+\phi}(\mathbf{z})] = \frac{1}{\tau} \int_{\mathcal{Z}} U_{\theta+\phi}(\mathbf{z}) dq_\theta(\mathbf{z}).$$

Since $\mathbf{z} = f_\theta(\mathbf{x}) \sim q_\theta$, we have

$$\mathbb{E}[\log \Gamma_{\phi, \tau}(\mathbf{z})] = \mathbb{E}_{\mathbf{z} \sim q_\theta}[\log \Gamma_{\phi, \tau}(\mathbf{z})].$$

Under the constant kernel-volume condition Asm. 2.1, $\tilde{\rho}_{\phi, \tau}(\mathbf{z}) = \Gamma_{\phi, \tau}(\mathbf{z})/V_\kappa(\tau)$ (Def. 2.2), hence

$$\mathbb{E}_{\mathbf{z} \sim q_\theta}[\log \Gamma_{\phi, \tau}(\mathbf{z})] = \log V_\kappa(\tau) + \mathbb{E}_{\mathbf{z} \sim q_\theta}[\log \tilde{\rho}_{\phi, \tau}(\mathbf{z})] = \log V_\kappa(\tau) - H_\times(q_\theta, \tilde{\rho}_{\phi, \tau}).$$

Substituting into the preceding expansion gives

$$\begin{aligned} \mathcal{L}_{\text{NCE}}^{x \rightarrow y}(\theta, \phi) &= \frac{1}{\tau} \int_{\mathcal{Z}} U_{\theta \rightarrow \phi}(\mathbf{z}) d q_\theta(\mathbf{z}) - H_\times(q_\theta, \tilde{\rho}_{\phi, \tau}) + \log(NV_\kappa(\tau)) + o(1) \\ &= \mathcal{J}_\tau^{x \rightarrow y}(\theta, \phi) + \log(NV_\kappa(\tau)) + o(1). \end{aligned}$$

The reverse direction $y \rightarrow x$ follows analogously, yielding the same form with (θ, ϕ) swapped. Averaging the two directional expansions and using the definition Eq. (7) proves the value-consistency: as $N \rightarrow \infty$,

$$|\mathcal{L}_{\text{Sym}}(\theta, \phi) - \mathcal{J}_\tau^{\text{Sym}}(\theta, \phi) - \log(NV_\kappa(\tau))| \rightarrow 0, \quad \forall \tau > 0, (\theta, \phi) \in \Theta \times \Phi.$$

Part II: Gradient consistency. Fix any $\tau > 0$ and $(\theta, \phi) \in \Theta \times \Phi$. Differentiating the batch loss in Eq. (55) gives

$$\nabla \ell_{\mathcal{B}}^{\text{Sym}}(\theta, \phi) = -\frac{1}{\tau} \nabla s(\mathbf{z}, \mathbf{w}) + \frac{1}{2} \nabla \log Z_{\mathcal{B}}^{\theta \rightarrow \phi}(\mathbf{z}) + \frac{1}{2} \nabla \log Z_{\mathcal{B}}^{\phi \rightarrow \theta}(\mathbf{w}), \quad (58)$$

where we denote the joint gradient $\nabla_{(\theta, \phi)}$ as ∇ for simplicity.

Step 1: Removing the positive term in each log-partition gradient. Define

$$\mathbf{g}_N^{\theta \rightarrow \phi} := \nabla \log(\mathbf{P} + \mathbf{S}_N^{\theta \rightarrow \phi}), \quad \mathbf{r}_N^{\theta \rightarrow \phi} := \nabla \log \mathbf{S}_N^{\theta \rightarrow \phi},$$

and analogously $(\mathbf{g}_N^{\phi \rightarrow \theta}, \mathbf{r}_N^{\phi \rightarrow \theta})$. As in Eq. (47), a direct algebraic manipulation yields

$$\mathbf{g}_N^{\theta \rightarrow \phi} - \mathbf{r}_N^{\theta \rightarrow \phi} = \frac{\nabla \mathbf{P}}{\mathbf{P} + \mathbf{S}_N^{\theta \rightarrow \phi}} - \frac{\mathbf{P}}{\mathbf{S}_N^{\theta \rightarrow \phi}(\mathbf{P} + \mathbf{S}_N^{\theta \rightarrow \phi})} \nabla \mathbf{S}_N^{\theta \rightarrow \phi},$$

and the same identity holds with $\theta \rightarrow \phi$ replaced by $\phi \rightarrow \theta$.

By assumption, \mathcal{Z} is compact and s is C^1 with bounded input gradient. Together with the C^1 encoders with uniformly bounded Jacobians, this implies that for each fixed $\tau > 0$ there exist finite constants

$$0 < m_\tau \leq \kappa_\tau(\cdot, \cdot) \leq M_\tau < \infty, \quad \sup_{(\theta, \phi) \in \Theta \times \Phi} \sup_{\mathcal{B}} \|\nabla \kappa_\tau\| \leq G_\tau < \infty.$$

Consequently, uniformly over (θ, ϕ) and batch realizations,

$$\mathbf{P} \leq M_\tau, \quad \|\nabla \mathbf{P}\| \leq G_\tau, \quad \mathbf{S}_N^{\theta \rightarrow \phi} \geq Nm_\tau, \quad \|\nabla \mathbf{S}_N^{\theta \rightarrow \phi}\| \leq NG_\tau,$$

and the same bounds hold for $\mathbf{S}_N^{\phi \rightarrow \theta}$. Taking norms in the identity above gives the uniform bound

$$\|\nabla \log Z_{\mathcal{B}}^{\theta \rightarrow \phi}(\mathbf{z}) - \nabla \log \mathbf{S}_N^{\theta \rightarrow \phi}(\mathbf{z})\| = O(N^{-1}), \quad \|\nabla \log Z_{\mathcal{B}}^{\phi \rightarrow \theta}(\mathbf{w}) - \nabla \log \mathbf{S}_N^{\phi \rightarrow \theta}(\mathbf{w})\| = O(N^{-1}), \quad (59)$$

where the $O(N^{-1})$ constants depend on τ but are uniform over $\Theta \times \Phi$.

Step 2: Consistency of the negative-sum ratios. We treat the direction $\theta \rightarrow \phi$; the reverse direction is analogous. Rewrite

$$\nabla \log \mathbf{S}_N^{\theta \rightarrow \phi} = \frac{\nabla \mathbf{S}_N^{\theta \rightarrow \phi}}{\mathbf{S}_N^{\theta \rightarrow \phi}} = \frac{\frac{1}{N} \sum_{j=1}^N \nabla \kappa_\tau(\mathbf{z}, \mathbf{w}'_j)}{\frac{1}{N} \sum_{j=1}^N \kappa_\tau(\mathbf{z}, \mathbf{w}'_j)}.$$

Conditioning on (\mathbf{x}, \mathbf{y}) , the anchor representations $\mathbf{z} = f_\theta(\mathbf{x})$ and $\mathbf{w} = g_\phi(\mathbf{y})$ are deterministic for fixed (θ, ϕ) . The negatives $\{\mathbf{y}'_j\}_{j=1}^N$ are i.i.d. from $p_{\mathbf{y}}$, hence $\{\mathbf{w}'_j\}_{j=1}^N$ are i.i.d. through the map g_ϕ . Write the kernel-smoothed mass as

$$\Gamma_{\phi, \tau}(\mathbf{z}) = \mathbb{E}_{\mathbf{y}' \sim p_{\mathbf{y}}}[\kappa_\tau(\mathbf{z}, g_\phi(\mathbf{y}'))],$$

which is strictly positive and uniformly bounded: $\Gamma_{\phi,\tau}(\mathbf{z}) \geq m_\tau$. By the law of large numbers and boundedness of κ_τ ,

$$\frac{1}{N} \sum_{j=1}^N \kappa_\tau(\mathbf{z}, \mathbf{w}'_j) \xrightarrow{p} \Gamma_{\phi,\tau}(\mathbf{z}).$$

Similarly, since $\|\nabla \kappa_\tau\|$ is uniformly bounded,

$$\frac{1}{N} \sum_{j=1}^N \nabla \kappa_\tau(\mathbf{z}, \mathbf{w}'_j) \xrightarrow{p} \mathbb{E}_{\mathbf{y}' \sim p_{\mathbf{y}}} [\nabla \kappa_\tau(\mathbf{z}, g_\phi(\mathbf{y}'))].$$

Since the expectation is taken with respect to the parameter-free distribution $p_{\mathbf{y}}$ and, by Asm. 4.1, $\sup_{(\theta,\phi)} \sup_{\mathbf{y}' \in \mathcal{Y}} \|\nabla \kappa_\tau(\mathbf{z}, g_\phi(\mathbf{y}'))\| < \infty$, differentiation under the expectation is justified by dominated convergence. Hence

$$\mathbb{E}_{\mathbf{y}' \sim p_{\mathbf{y}}} [\nabla \kappa_\tau(\mathbf{z}, g_\phi(\mathbf{y}'))] = \nabla \mathbb{E}_{\mathbf{y}' \sim p_{\mathbf{y}}} [\kappa_\tau(\mathbf{z}, g_\phi(\mathbf{y}'))] = \nabla \Gamma_{\phi,\tau}(\mathbf{z}).$$

Since the denominator converges to a strictly positive limit, the continuous mapping theorem yields

$$\nabla \log S_N^{\theta+\phi} \xrightarrow{p} \frac{\nabla \Gamma_{\phi,\tau}(\mathbf{z})}{\Gamma_{\phi,\tau}(\mathbf{z})} = \nabla \log \Gamma_{\phi,\tau}(\mathbf{z}). \quad (60)$$

The reverse direction follows identically by defining

$$\Gamma_{\theta,\tau}(\mathbf{w}) := \mathbb{E}_{\mathbf{x}' \sim p_{\mathbf{x}}} [\kappa_\tau(f_\theta(\mathbf{x}'), \mathbf{w})],$$

and obtaining

$$\nabla \log S_N^{\phi+\theta} \xrightarrow{p} \nabla \log \Gamma_{\theta,\tau}(\mathbf{w}). \quad (61)$$

Combining Eqs. (59) to (61), as $N \rightarrow \infty$, we obtain the batch-level limit

$$\nabla \log Z_{\mathcal{B}}^{\theta+\phi}(\mathbf{z}) \xrightarrow{p} \nabla \log \Gamma_{\phi,\tau}(\mathbf{z}), \quad \nabla \log Z_{\mathcal{B}}^{\phi+\theta}(\mathbf{w}) \xrightarrow{p} \nabla \log \Gamma_{\theta,\tau}(\mathbf{w}). \quad (62)$$

Step 3: Passing to the population objective and identifying $\nabla_{(\theta,\phi)} \mathcal{J}_\tau^{\text{Sym}}$. By Lem. C.2, $\|\nabla \ell_{\mathcal{B}}^{\text{Sym}}(\theta, \phi)\|$ is uniformly bounded over $\Theta \times \Phi$ and all N . Therefore, applying dominated convergence to Eq. (58) together with Eq. (62) yields

$$\begin{aligned} \nabla \mathcal{L}_{\text{Sym}}(\theta, \phi) &= \mathbb{E}_{\mathcal{B}} [\nabla \ell_{\mathcal{B}}^{\text{Sym}}(\theta, \phi)] \longrightarrow -\frac{1}{\tau} \mathbb{E}_{(\mathbf{z}, \mathbf{w}) \sim \pi_{\theta\phi}} [\nabla s(\mathbf{z}, \mathbf{w})] \\ &\quad + \frac{1}{2} \mathbb{E}_{\mathbf{z} \sim q_\theta} [\nabla \log \Gamma_{\phi,\tau}(\mathbf{z})] \\ &\quad + \frac{1}{2} \mathbb{E}_{\mathbf{w} \sim q_\phi} [\nabla \log \Gamma_{\theta,\tau}(\mathbf{w})]. \end{aligned} \quad (63)$$

We now identify the right-hand side as $\nabla \mathcal{J}_\tau^{\text{Sym}}(\theta, \phi)$. First, by the definition of $\pi_{\theta\phi} = (f_\theta \times g_\phi)_{\#} r_{\text{mm}}$ and the law of iterated expectation applied to Def. 4.1,

$$\int_{\mathcal{Z}} U_{\theta+\phi}(\mathbf{z}) dq_\theta(\mathbf{z}) = \mathbb{E}_{(\mathbf{x}, \mathbf{y}) \sim r_{\text{mm}}} [-s(f_\theta(\mathbf{x}), g_\phi(\mathbf{y}))] = \mathbb{E}_{(\mathbf{z}, \mathbf{w}) \sim \pi_{\theta\phi}} [\nabla s(\mathbf{z}, \mathbf{w})],$$

and similarly $\int_{\mathcal{Z}} U_{\phi+\theta}(\mathbf{w}) dq_\phi(\mathbf{w})$ equals the same joint expectation.⁶ Under Asm. 4.1, we may differentiate under the expectation to obtain

$$\nabla \int_{\mathcal{Z}} U_{\theta+\phi}(\mathbf{z}) dq_\theta(\mathbf{z}) = \nabla \int_{\mathcal{Z}} U_{\phi+\theta}(\mathbf{w}) dq_\phi(\mathbf{w}) = -\mathbb{E}_{(\mathbf{z}, \mathbf{w}) \sim \pi_{\theta\phi}} [\nabla s(\mathbf{z}, \mathbf{w})].$$

Second, using $\log \tilde{\rho}_{\phi,\tau} = \log \Gamma_{\phi,\tau} - \log V_\kappa(\tau)$ and $\log \tilde{\rho}_{\theta,\tau} = \log \Gamma_{\theta,\tau} - \log V_\kappa(\tau)$ (Def. 2.2), with $V_\kappa(\tau)$ independent of (θ, ϕ) by Asm. 2.1, we have

$$\begin{aligned} \nabla H_{\times}(q_\theta, \tilde{\rho}_{\phi,\tau}) &= -\nabla \int_{\mathcal{Z}} \log \tilde{\rho}_{\phi,\tau}(\mathbf{z}) dq_\theta(\mathbf{z}) = -\int_{\mathcal{Z}} \nabla \log \Gamma_{\phi,\tau}(\mathbf{z}) dq_\theta(\mathbf{z}), \\ \nabla H_{\times}(q_\phi, \tilde{\rho}_{\theta,\tau}) &= -\nabla \int_{\mathcal{Z}} \log \tilde{\rho}_{\theta,\tau}(\mathbf{w}) dq_\phi(\mathbf{w}) = -\int_{\mathcal{Z}} \nabla \log \Gamma_{\theta,\tau}(\mathbf{w}) dq_\phi(\mathbf{w}), \end{aligned}$$

⁶While the binding energy yields the same expectation, the potential fields $U_{\theta+\phi}$ and $U_{\phi+\theta}$ differ pointwise.

where the derivative passes under the integral by dominated convergence, since $\|\nabla \log \Gamma_{\cdot, \tau}\|$ is uniformly bounded by Asm. 4.1 and Lem. C.2.

Combining these identities with the definition of $\mathcal{J}_\tau^{\text{Sym}}$ in Def. 4.2 shows that the limit in Eq. (63) equals $\nabla \mathcal{J}_\tau^{\text{Sym}}(\theta, \phi)$. Therefore, as $N \rightarrow \infty$, for any fixed $(\theta, \phi) \in \Theta \times \Phi$, the θ - and ϕ -components of the above argument yield

$$\|\nabla_\theta \mathcal{L}_{\text{Sym}} - \nabla_\theta \mathcal{J}_\tau^{\text{Sym}}\| \rightarrow 0, \quad \|\nabla_\phi \mathcal{L}_{\text{Sym}} - \nabla_\phi \mathcal{J}_\tau^{\text{Sym}}\| \rightarrow 0.$$

Consequently, for the joint gradient $\nabla_{(\theta, \phi)} = (\nabla_\theta, \nabla_\phi)$,

$$\left\| \nabla_{(\theta, \phi)} \mathcal{L}_{\text{Sym}} - \nabla_{(\theta, \phi)} \mathcal{J}_\tau^{\text{Sym}} \right\| = \sqrt{\left\| \nabla_\theta \mathcal{L}_{\text{Sym}} - \nabla_\theta \mathcal{J}_\tau^{\text{Sym}} \right\|^2 + \left\| \nabla_\phi \mathcal{L}_{\text{Sym}} - \nabla_\phi \mathcal{J}_\tau^{\text{Sym}} \right\|^2} \rightarrow 0.$$

□

E.2. Proof of Prop. 4.1

Proposition 4.1 (Barrier best response and extremal collapse). *Assume \mathcal{Z} is compact with $\mu(\mathcal{Z}) < \infty$, and let $\mathcal{F}_{\tau, \mathbf{U}_{1,2}}^{\text{Sym}}$ be as in Def. 4.3. Fix $\rho_2 \in \mathcal{P}_{\mu, \underline{\rho}}(\mathcal{Z})$ and define the effective potential field by $V_{1|2}(\mathbf{z}) := \frac{1}{\tau} U_{1+2}(\mathbf{z}) + \log \rho_2(\mathbf{z})$. Then, the coordinate map $\rho_1 \mapsto \mathcal{F}_{\tau, \mathbf{U}_{1,2}}^{\text{Sym}}(\rho_1, \rho_2)$ is concave on $\mathcal{P}_{\mu, \underline{\rho}}(\mathcal{Z})$, and its infimum is approached by sequences that concentrate the excess mass $M_{\text{ex}} := 1 - \rho \mu(\mathcal{Z})$ onto approximate minimizers of $V_{1|2}$, leaving only the floor $\underline{\rho}$ elsewhere. Formally, for a sufficiently small $\sigma > 0$, let $\mathcal{W}_1^\sigma := \{\mathbf{z} \in \mathcal{Z} : V_{1|2}(\mathbf{z}) \leq \text{ess inf}_\mu V_{1|2} + \sigma\}$ be the sublevel set. Define the σ -approximate density $\rho_1^{(\sigma)}$ by concentrating the excess mass on a shrinking set $\mathcal{S}_1^\sigma \subseteq \mathcal{W}_1^\sigma$:⁷*

$$\rho_1^{(\sigma)}(\mathbf{z}) = \underline{\rho} + \mathbb{1}_{\mathcal{S}_1^\sigma}(\mathbf{z}) \cdot M_{\text{ex}} / \mu(\mathcal{S}_1^\sigma), \quad \lim_{\sigma \rightarrow 0} \mu(\mathcal{S}_1^\sigma) = 0. \quad (9)$$

As $\sigma \rightarrow 0$, the energy of $\rho_1^{(\sigma)}$ converges to the infimum:

$$\lim_{\sigma \rightarrow 0} \mathcal{F}_{\tau, \mathbf{U}_{1,2}}^{\text{Sym}}(\rho_1^{(\sigma)}, \rho_2) = \inf_{\rho_1 \in \mathcal{P}_+(\mathcal{Z})} \mathcal{F}_{\tau, \mathbf{U}_{1,2}}^{\text{Sym}}(\rho_1, \rho_2). \quad (10)$$

An analogous statement holds when optimizing in ρ_2 with ρ_1 fixed, with respect to the dual effective potential field $V_{2|1}(\mathbf{z}) := \frac{1}{\tau} U_{2+1}(\mathbf{z}) + \log \rho_1(\mathbf{z})$.

Proof intuition. This proof establishes that when one modality's distribution (ρ_2) is held fixed, the optimal distribution for the other modality (ρ_1) collapses into an extreme, "spiky" state. Rather than spreading out, it flattens to the absolute minimum allowed density everywhere, while dumping all its remaining probability mass into the deepest valley of an effective potential landscape. The logic unfolds in three geometric phases:

(i) Unlike standard convex optimization where distributions seek a balanced equilibrium, the cross-entropy term here makes the functional *concave* with respect to ρ_1 . Concave minimization pushes solutions to the extreme edges of the feasible space. We calculate a theoretical absolute minimum energy (i.e., the floor) by imagining a hypothetical distribution that sits perfectly flat at the strict lower bound $\underline{\rho}$ everywhere, with all its "excess" probability mass magically teleported to the absolute minimum of the effective potential $V_{1|2}$.

(ii) To prove this theoretical floor is physically reachable, we construct a sequence of valid distributions. We take the excess mass and squeeze it into a microscopic, highly concentrated spike (a sublevel set) directly over the lowest valleys of the potential.

(iii) Squeezing mass into an infinitely narrow, tall spike threatens to blow up the logarithmic entropy penalty. However, by exploiting the absolute continuity of the background measure, we can precisely control how fast the spike shrinks. We prove that the log-penalty grows slower than the base shrinks, ultimately crushing the penalty to zero. The sequence touches the theoretical floor, confirming that the optimal coordinate state is a singular concentration atop a flat baseline.

Proof. Fix $\tau > 0$ and $\rho_2 \in \mathcal{P}_{\mu, \underline{\rho}}(\mathcal{Z})$. Throughout, we treat ρ_2 as fixed and analyze ρ_1 (while analysis for ρ_2 applies symmetrically) and write the coordinate map as

$$\mathcal{F}_1(\rho_1) := \mathcal{F}_{\tau, \mathbf{U}_{1,2}}^{\text{Sym}}(\rho_1, \rho_2), \quad \rho_1 \in \mathcal{P}_{\mu, \underline{\rho}}(\mathcal{Z}).$$

⁷Typically, $\mathcal{S}_1^\sigma = \mathcal{W}_1^\sigma$ for sharp minima, or any vanishing subset $\mathcal{S}_1^\sigma \subset \mathcal{W}_1^\sigma$ for flat minima.

Step 1: Concavity of $\rho_1 \mapsto \mathcal{F}_\tau$ and its lower bound. Using $H(\rho_1) = -\int_{\mathcal{Z}} \rho_1 \log \rho_1 d\mu$, $D_{\text{KL}}(\rho_1 \parallel \rho_2) = \int_{\mathcal{Z}} \rho_1 \log(\rho_1/\rho_2) d\mu$, and $D_{\text{KL}}(\rho_2 \parallel \rho_1) = \int_{\mathcal{Z}} \rho_2 \log(\rho_2/\rho_1) d\mu$, expand the ρ_1 -dependent terms in $\mathcal{F}_1(\rho_1)$:

$$\mathcal{F}_1(\rho_1) = \frac{1}{2} \int_{\mathcal{Z}} \rho_1(\mathbf{z}) V_{1|2}(\mathbf{z}) d\mu(\mathbf{z}) + \frac{1}{2} \int_{\mathcal{Z}} \rho_2(\mathbf{z}) \log \rho_1(\mathbf{z}) d\mu(\mathbf{z}) + C(\rho_2), \quad (64)$$

where $V_{1|2}(\mathbf{z}) := \frac{1}{\tau} U_{1+2}(\mathbf{z}) + \log \rho_2(\mathbf{z})$, and $C(\rho_2)$ does not depend on ρ_1 .

We observe $\rho_1 \mapsto \int_{\mathcal{Z}} \rho_1 V_{1|2} d\mu$ is linear, and $\rho_1 \mapsto \int_{\mathcal{Z}} \rho_2 \log \rho_1 d\mu$ is concave on the positive cone since \log is concave and $\rho_2 \geq \underline{\rho} > 0$. Thus, $\rho_1 \mapsto \mathcal{F}_1$ is concave on the convex set $\mathcal{P}_{\mu, \underline{\rho}}(\mathcal{Z})$. Consequently, the infimum over $\mathcal{P}_{\mu, \underline{\rho}}(\mathcal{Z})$ can be approached by a sequence on the boundary.

Now, write any feasible $\rho_1 \in \mathcal{P}_{\mu, \underline{\rho}}(\mathcal{Z})$ as $\rho_1(\mathbf{z}) = \underline{\rho} + \eta(\mathbf{z})$ so that $\eta(\mathbf{z}) \geq 0$. The excess probability mass is strictly positive

$$M_{\text{ex}} = \int_{\mathcal{Z}} \eta(\mathbf{z}) d\mu(\mathbf{z}) > 0.$$

Then, using $V_{1|2}(\mathbf{z}) \geq \text{ess inf}_{\mu} V_{1|2} =: v_*$ and $\log \rho_1(\mathbf{z}) \geq \log \underline{\rho}$ μ -a.e.,

$$\begin{aligned} \int_{\mathcal{Z}} \rho_1 V_{1|2}(\mathbf{z}) d\mu(\mathbf{z}) &= \underline{\rho} \int_{\mathcal{Z}} V_{1|2}(\mathbf{z}) d\mu(\mathbf{z}) + \int_{\mathcal{Z}} \eta(\mathbf{z}) V_{1|2}(\mathbf{z}) d\mu(\mathbf{z}) \\ &\geq \underline{\rho} \int_{\mathcal{Z}} V_{1|2}(\mathbf{z}) d\mu(\mathbf{z}) + v_* M_{\text{ex}}, \end{aligned}$$

and

$$\int_{\mathcal{Z}} \rho_2 \log(\rho_1) d\mu(\mathbf{z}) \geq \int_{\mathcal{Z}} \rho_2 \log \underline{\rho} d\mu(\mathbf{z}) = \log \underline{\rho}.$$

Plugging these into Eq. (64) yields the lower bound

$$\mathcal{F}_1(\rho_1) \geq \frac{1}{2} \left(\underline{\rho} \int_{\mathcal{Z}} V_{1|2}(\mathbf{z}) d\mu(\mathbf{z}) + v_* M_{\text{ex}} \right) + \frac{1}{2} \log \underline{\rho} + C(\rho_2) =: \mathcal{F}_*. \quad (65)$$

Therefore,

$$\inf_{\rho_1 \in \mathcal{P}_{\mu, \underline{\rho}}(\mathcal{Z})} \mathcal{F}_1(\rho_1) \geq \mathcal{F}_*.$$

Step 2: Evaluate the coordinate map \mathcal{F}_1 at $\rho_1^{(\sigma)}$. For each $\sigma > 0$, define the sublevel set

$$\mathcal{W}_1^\sigma = \{\mathbf{z} \in \mathcal{Z} : V_{1|2}(\mathbf{z}) \leq v_* + \sigma\}, \quad \text{with } \mu(\mathcal{W}_1^\sigma) > 0.$$

Further, since μ is the volume measure on the compact manifold \mathcal{Z} , μ is non-atomic. Thus, there exist a shrinking subset $\mathcal{S}_1^\sigma \subseteq \mathcal{W}_1^\sigma$ satisfying $\mu(\mathcal{S}_1^\sigma) \xrightarrow{\sigma \rightarrow 0} 0$ (when \mathcal{W}_1^σ itself is sharp $\mu(\mathcal{W}_1^\sigma) \xrightarrow{\sigma \rightarrow 0} 0$, we simply choose $\mathcal{S}_1^\sigma = \mathcal{W}_1^\sigma$). Defined the density as

$$\rho_1^{(\sigma)}(\mathbf{z}) = \underline{\rho} + \mathbb{1}_{\mathcal{S}_1^\sigma}(\mathbf{z}) \frac{M_{\text{ex}}}{\mu(\mathcal{S}_1^\sigma)}.$$

Since $\rho_1^{(\sigma)} \geq \underline{\rho}$ and

$$\int_{\mathcal{Z}} \rho_1^{(\sigma)} d\mu(\mathbf{z}) = \underline{\rho} \mu(\mathcal{Z}) + \frac{M_{\text{ex}}}{\mu(\mathcal{S}_1^\sigma)} \mu(\mathcal{S}_1^\sigma) = \underline{\rho} \mu(\mathcal{Z}) + M_{\text{ex}} = 1,$$

we have $\rho_1^{(\sigma)} \in \mathcal{P}_{\mu, \underline{\rho}}(\mathcal{Z})$.

Now, evaluate the coordinate map \mathcal{F}_1 at $\rho_1^{(\sigma)}$:

(i) *Linear term.* Since $\mathcal{S}_1^\sigma \subseteq \mathcal{W}_1^\sigma$, we have $V_{1|2}(\mathbf{z}) \leq v_* + \sigma$ on \mathcal{S}_1^σ , hence

$$\int_{\mathcal{Z}} \rho_1^{(\sigma)} V_{1|2}(\mathbf{z}) d\mu = \underline{\rho} \int_{\mathcal{Z}} V_{1|2} d\mu + \frac{M_{\text{ex}}}{\mu(\mathcal{S}_1^\sigma)} \int_{\mathcal{S}_1^\sigma} V_{1|2} d\mu \leq \underline{\rho} \int_{\mathcal{Z}} V_{1|2} d\mu + M_{\text{ex}}(v_* + \sigma).$$

(ii) *Log term.* Split the domain $\mathcal{Z} = (\mathcal{Z} \setminus \mathcal{S}_1^\sigma) \cup \mathcal{S}_1^\sigma$:

$$\int_{\mathcal{Z}} \rho_2 \log \rho_1^{(\sigma)} d\mu = \int_{\mathcal{Z} \setminus \mathcal{S}_1^\sigma} \rho_2 \log \underline{\rho} d\mu + \int_{\mathcal{S}_1^\sigma} \rho_2 \log \left(\underline{\rho} + \frac{M_{\text{ex}}}{\mu(\mathcal{S}_1^\sigma)} \right) d\mu.$$

Using the mass of the spike $m_\sigma := \int_{\mathcal{S}_1^\sigma} \rho_2 d\mu$, the first term is $(1 - m_\sigma) \log \underline{\rho}$. Therefore,

$$\int \rho_2 \log \rho_1^{(\sigma)} d\mu = \log \underline{\rho} + m_\sigma \left(\log \left(\underline{\rho} + \frac{M_{\text{ex}}}{\mu(\mathcal{S}_1^\sigma)} \right) - \log \underline{\rho} \right) = \log \underline{\rho} + m_\sigma L_\sigma,$$

where $L_\sigma := \log \left(1 + \frac{M_{\text{ex}}}{\underline{\rho} \mu(\mathcal{S}_1^\sigma)} \right)$.

Combining terms yields the inequality

$$\mathcal{F}_1(\rho_1^{(\sigma)}) \leq \frac{1}{2} \left(\underline{\rho} \int V_{1|2} d\mu + M_{\text{ex}}(v_* + \sigma) \right) + \frac{1}{2} (\log \underline{\rho} + m_\sigma L_\sigma) + C(\rho_2). \quad (66)$$

Step 3: Conclude convergence. We first analyze the limit of the log-penalty $m_\sigma L_\sigma \rightarrow 0$ as $\sigma \rightarrow 0$. Since $\rho_2 \in L^1(\mu)$ and $\mu(\mathcal{Z}) < \infty$, the integral is absolutely continuous: for every $\varepsilon > 0$ there exists $\delta(\varepsilon) > 0$ such that for any measurable $\mathcal{A} \subset \mathcal{Z}$ with $\mu(\mathcal{A}) \leq \delta(\varepsilon)$,

$$\int_{\mathcal{A}} \rho_2 d\mu \leq \varepsilon.$$

Define the modulus of absolute continuity

$$\Psi(t) := \sup \left\{ \int_{\mathcal{A}} \rho_2 d\mu : \mathcal{A} \subset \mathcal{Z} \text{ measurable, } \mu(\mathcal{A}) \leq t \right\}.$$

Since $\rho_2 \in L^1(\mu)$ and $\mu(\mathcal{Z}) < \infty$, we have $\Psi(t) \rightarrow 0$ as $t \rightarrow 0$. Since $\Psi(t) \rightarrow 0$ as $t \rightarrow 0$ and $|\log t|^{-2} \rightarrow 0$ as $t \rightarrow 0$, we may choose a sequence $\delta_\sigma \rightarrow 0$ such that

$$\delta_\sigma \leq \mu(\mathcal{W}_1^\sigma), \quad \Psi(\delta_\sigma) \leq |\log \delta_\sigma|^{-2}.$$

By non-atomicity of μ , choose $\mathcal{S}_1^\sigma \subseteq \mathcal{W}_1^\sigma$ with $\mu(\mathcal{S}_1^\sigma) = \delta_\sigma$. Then

$$m_\sigma := \int_{\mathcal{S}_1^\sigma} \rho_2 d\mu \leq \Psi(\delta_\sigma) \leq \frac{1}{|\log \delta_\sigma|^2}.$$

With $L_\sigma = \log(1 + M_{\text{ex}}/(\underline{\rho} \mu(\mathcal{S}_1^\sigma)))$ and $\mu(\mathcal{S}_1^\sigma) = \delta_\sigma$, we have

$$L_\sigma \leq \log \left(1 + \frac{M_{\text{ex}}}{\underline{\rho}} \right) + |\log \delta_\sigma| =: K + |\log \delta_\sigma|.$$

Therefore,

$$0 \leq m_\sigma L_\sigma \leq \frac{1}{|\log \delta_\sigma|^2} (K + |\log \delta_\sigma|) = \frac{K}{|\log \delta_\sigma|^2} + \frac{1}{|\log \delta_\sigma|} \xrightarrow{\sigma \rightarrow 0} 0.$$

Thus, the additional log-penalty incurred by the spike vanishes.

Now, subtract \mathcal{F}_* (Eq. (65)) from Eq. (66):

$$\mathcal{F}_1(\rho_1^{(\sigma)}) - \mathcal{F}_* \leq \frac{1}{2} (M_{\text{ex}} \sigma + m_\sigma L_\sigma).$$

Letting $\sigma \rightarrow 0$ gives

$$\limsup_{\sigma \rightarrow 0} \mathcal{F}_1(\rho_1^{(\sigma)}) \leq \mathcal{F}_*.$$

But Step 1 showed $\inf_{\rho_1 \in \mathcal{P}_{\mu, \underline{\rho}}(\mathcal{Z})} \mathcal{F}_1(\rho_1) \geq \mathcal{F}_*$, therefore

$$\inf_{\rho_1 \in \mathcal{P}_{\mu, \underline{\rho}}(\mathcal{Z})} \mathcal{F}_1(\rho_1) = \mathcal{F}_* \quad \text{and} \quad \lim_{\sigma \rightarrow 0} \mathcal{F}_1(\rho_1^{(\sigma)}) = \inf_{\rho_1 \in \mathcal{P}_{\mu, \underline{\rho}}(\mathcal{Z})} \mathcal{F}_1(\rho_1),$$

concluding that the infimum is approached by the boundary solutions concentrating on the minima of the effective potential field $V_{1|2} = \frac{1}{\tau} U_{1+2} + \log \rho_2$.

The ρ_2 -coordinate statement is identical after swapping indices and using $V_{2|1} = \frac{1}{\tau} U_{2+1} + \log \rho_1$. \square

E.3. Proof of Thm. 4.2

Theorem 4.2 (Low-temperature multimodal energy consistency). *Assume Asms. 2.1, 3.2 and 4.1. Fix any $(\theta, \phi) \in \Theta \times \Phi$, and assume $q_\theta \ll \mu$, $q_\phi \ll \mu$ with continuous densities ρ_θ, ρ_ϕ bounded below: $\inf_{\mathbf{z} \in \mathcal{Z}} \rho_\theta(\mathbf{z}) \geq \underline{\rho}_\theta > 0$ and $\inf_{\mathbf{z} \in \mathcal{Z}} \rho_\phi(\mathbf{z}) \geq \underline{\rho}_\phi > 0$. Let $\varepsilon_{\text{kde}}^{(\theta)}(\tau) := \|\tilde{\rho}_{\theta, \tau} - \rho_\theta\|_\infty$ and $\varepsilon_{\text{kde}}^{(\phi)}(\tau) := \|\tilde{\rho}_{\phi, \tau} - \rho_\phi\|_\infty$. Then there exists $\tau_0(\theta, \phi) > 0$ such that for all $0 < \tau \leq \tau_0(\theta, \phi)$,*

$$\left| \mathcal{F}_\tau^{\text{Sym}}(\theta, \phi) - \mathcal{F}_{\tau, \mathbf{U}_{\theta, \phi}}^{\text{Sym}}(\rho_\theta, \rho_\phi) \right| \leq \frac{(\varepsilon_{\text{kde}}^{(\theta)}(\tau) + \varepsilon_{\text{kde}}^{(\phi)}(\tau))}{\min\{\underline{\rho}_\theta, \underline{\rho}_\phi\}}.$$

Moreover, as $\tau \rightarrow 0^+$, $|\mathcal{F}_\tau^{\text{Sym}}(\theta, \phi) - \mathcal{F}_{\tau, \mathbf{U}_{\theta, \phi}}^{\text{Sym}}(\rho_\theta, \rho_\phi)| \rightarrow 0$. Here, $\mathcal{F}_{\tau, \mathbf{U}_{\theta, \phi}}^{\text{Sym}}(\rho_\theta, \rho_\phi)$ is the intrinsic multimodal energy (Def. 4.3) evaluated at the densities q_θ, q_ϕ and the directional potential fields $\mathbf{U}_{\theta, \phi} := (U_{\theta \rightarrow \phi}, U_{\phi \rightarrow \theta})$.

Proof intuition. This proof establishes that in the low-temperature limit, the empirical cross-modal parametric energy perfectly mirrors the theoretical, dual-density thermodynamic free energy. The argument relies on an algebraic cancellation and the geometric stability of the kernel smoothing:

(i) We first decompose both the learned objective and the theoretical free energy into their core components: the cross-modal binding potentials and the internal entropies. When we calculate the exact difference between the two functionals, these complex binding and entropy terms perfectly cancel out. The remaining discrepancy is entirely isolated to the KL divergence between the true marginal densities and their kernel-smoothed counterparts.

(ii) To prove this residual discrepancy vanishes, we rely on the boundary of the true marginals. Because the densities are bounded away from zero, the logarithmic ratio inside the KL divergence operates in a strictly Lipschitz-continuous regime. This allows us to analytically bound the complex integral by the maximum worst-case estimation error (the KDE mismatch) of each modality.

(iii) Because the kernel smoothing of both the vision and language manifolds independently converges to the true underlying densities as $\tau \rightarrow 0^+$, their respective KDE mismatches vanish. This crushes the KL divergence between each modality's raw density and the smoothed density to zero, mathematically guaranteeing that the learned cross-modal energy landscape is indistinguishable from the true thermodynamic landscape.

Proof. Fix any $(\theta, \phi) \in \Theta \times \Phi$. Under Asm. 4.1, s is bounded and Borel measurable, hence both cross-modal potentials $U_{\theta \rightarrow \phi}$ and $U_{\phi \rightarrow \theta}$ from Def. 4.1 are Borel measurable and bounded. Moreover, since \mathcal{Z} is compact and ρ_θ, ρ_ϕ are continuous with $\rho_\theta, \rho_\phi \geq \min\{\underline{\rho}_\theta, \underline{\rho}_\phi\} > 0$, both $\log \rho_\theta$ and $\log \rho_\phi$ are bounded, hence $D_{\text{KL}}(\rho_\theta \| \rho_\phi)$ and $D_{\text{KL}}(\rho_\phi \| \rho_\theta)$ are finite. Consequently, the multimodal functional $\mathcal{F}_{\tau, \mathbf{U}_{\theta, \phi}}^{\text{Sym}}(q_\theta, q_\phi)$ is well-defined.

Step 1: Functional discrepancy reduces to log-ratio perturbations. Recall the directional multimodal parametric energies from Def. 4.2:

$$\mathcal{J}_\tau^{\theta \rightarrow \phi}(\theta, \phi) = \frac{1}{\tau} \mathcal{U}^{\theta \rightarrow \phi}(q_\theta) - H_\times(q_\theta, \tilde{\rho}_{\phi, \tau}), \quad \mathcal{J}_\tau^{\phi \rightarrow \theta}(\theta, \phi) = \frac{1}{\tau} \mathcal{U}^{\phi \rightarrow \theta}(q_\phi) - H_\times(q_\phi, \tilde{\rho}_{\theta, \tau}),$$

and $\mathcal{J}_\tau^{\text{Sym}} = \frac{1}{2}(\mathcal{J}_\tau^{\theta \rightarrow \phi} + \mathcal{J}_\tau^{\phi \rightarrow \theta})$. Using $H_\times(q_1, \rho_2) = H(\rho_1) + D_{\text{KL}}(\rho_1 \| \rho_2)$ with $\rho_1 = dq_1/d\mu$, we can rewrite

$$\mathcal{J}_\tau^{\text{Sym}}(\theta, \phi) = \frac{1}{2} \left(\mathcal{F}_{\tau, U_{\theta \rightarrow \phi}}(\rho_\theta) + \mathcal{F}_{\tau, U_{\phi \rightarrow \theta}}(\rho_\phi) \right) - \frac{1}{2} \left(D_{\text{KL}}(q_\theta \| \tilde{\rho}_{\phi, \tau}) + D_{\text{KL}}(q_\phi \| \tilde{\rho}_{\theta, \tau}) \right). \quad (67)$$

On the other hand, by Def. 4.3 with $D_{\text{KL}}^{\text{Sym}}(\rho_\theta, \rho_\phi) = \frac{1}{2}(D_{\text{KL}}(\rho_\theta \| \rho_\phi) + D_{\text{KL}}(\rho_\phi \| \rho_\theta))$,

$$\mathcal{F}_{\tau, \mathbf{U}_{\theta, \phi}}^{\text{Sym}}(\rho_\theta, \rho_\phi) = \frac{1}{2} \left(\mathcal{F}_{\tau, U_{\theta \rightarrow \phi}}(\rho_\theta) + \mathcal{F}_{\tau, U_{\phi \rightarrow \theta}}(\rho_\phi) \right) - D_{\text{KL}}^{\text{Sym}}(\rho_\theta, \rho_\phi). \quad (68)$$

Subtracting Eq. (68) from Eq. (67), the potential and entropy terms cancel, giving the exact identity

$$\begin{aligned} \mathcal{F}_{\tau, \mathbf{U}_{\theta, \phi}}^{\text{Sym}}(\rho_\theta, \rho_\phi) - \mathcal{J}_\tau^{\text{Sym}}(\theta, \phi) = \\ \frac{1}{2} \left(D_{\text{KL}}(\rho_\theta \| \tilde{\rho}_{\phi, \tau}) - D_{\text{KL}}(\rho_\theta \| \rho_\phi) + D_{\text{KL}}(\rho_\phi \| \tilde{\rho}_{\theta, \tau}) - D_{\text{KL}}(\rho_\phi \| \rho_\theta) \right). \end{aligned} \quad (69)$$

Now, use the elementary difference formula: for any μ -densities p, r_1, r_2 with $r_1, r_2 > 0$ μ -a.e.,

$$D_{\text{KL}}(p \| r_1) - D_{\text{KL}}(p \| r_2) = \int_{\mathcal{Z}} p \log \frac{r_2}{r_1} d\mu.$$

Since $\kappa_\tau > 0$, ρ_θ, ρ_ϕ are probability densities, and $\tilde{\rho}_{\theta,\tau}, \tilde{\rho}_{\phi,\tau} > 0$ everywhere. Apply it to $(p, r_1, r_2) = (\rho_\theta, \tilde{\rho}_{\phi,\tau}, \rho_\phi)$ and $(\rho_\phi, \tilde{\rho}_{\theta,\tau}, \rho_\theta)$ to obtain

$$\mathcal{F}_{\tau, \mathbf{U}_{\theta, \phi}}^{\text{Sym}}(\rho_\theta, \rho_\phi) - \mathcal{J}_\tau^{\text{Sym}}(\theta, \phi) = \frac{1}{2} \left(\int \rho_\theta \log \frac{\rho_\phi}{\tilde{\rho}_{\phi,\tau}} d\mu + \int \rho_\phi \log \frac{\rho_\theta}{\tilde{\rho}_{\theta,\tau}} d\mu \right). \quad (70)$$

Step 2: Nonasymptotic bound by KDE sup-errors. By the lower bounds $\rho_\theta \geq \underline{\rho}_\theta$ and $\rho_\phi \geq \underline{\rho}_\phi$ and the Lem. C.3 applied separately to ρ_θ and ρ_ϕ , there exists $\tau_0(\theta, \phi) > 0$ such that for all $0 < \tau \leq \tau_0(\theta, \phi)$,

$$\varepsilon_{\text{kde}}^{(\theta)}(\tau) = \|\tilde{\rho}_{\theta,\tau} - \rho_\theta\|_\infty \leq \frac{\underline{\rho}_\theta}{2}, \quad \varepsilon_{\text{kde}}^{(\phi)}(\tau) = \|\tilde{\rho}_{\phi,\tau} - \rho_\phi\|_\infty \leq \frac{\underline{\rho}_\phi}{2}.$$

Hence, for all $\mathbf{z} \in \mathcal{Z}$ and all such τ ,

$$\tilde{\rho}_{\theta,\tau}(\mathbf{z}) \geq \frac{\underline{\rho}_\theta}{2}, \quad \tilde{\rho}_{\phi,\tau}(\mathbf{z}) \geq \frac{\underline{\rho}_\phi}{2}. \quad (71)$$

On $[\underline{\rho}_\phi/2, \infty)$, the map $\log(\cdot)$ is Lipschitz with constant $2/\underline{\rho}_\phi$; thus, for all \mathbf{z} ,

$$|\log \rho_\phi(\mathbf{z}) - \log \tilde{\rho}_{\phi,\tau}(\mathbf{z})| \leq \frac{2}{\underline{\rho}_\phi} |\rho_\phi(\mathbf{z}) - \tilde{\rho}_{\phi,\tau}(\mathbf{z})| \leq \frac{2\varepsilon_{\text{kde}}^{(\phi)}(\tau)}{\underline{\rho}_\phi}.$$

Equivalently,

$$\left| \log \frac{\rho_\phi(\mathbf{z})}{\tilde{\rho}_{\phi,\tau}(\mathbf{z})} \right| \leq \frac{2\varepsilon_{\text{kde}}^{(\phi)}(\tau)}{\underline{\rho}_\phi}. \quad (72)$$

Analogously,

$$\left| \log \frac{\rho_\theta(\mathbf{z})}{\tilde{\rho}_{\theta,\tau}(\mathbf{z})} \right| \leq \frac{2\varepsilon_{\text{kde}}^{(\theta)}(\tau)}{\underline{\rho}_\theta}. \quad (73)$$

Now, bound Eq. (70) using $\int_{\mathcal{Z}} \rho_\theta d\mu = \int_{\mathcal{Z}} \rho_\phi d\mu = 1$:

$$\begin{aligned} |\mathcal{F}_{\tau, \mathbf{U}_{\theta, \phi}}^{\text{Sym}}(\rho_\theta, \rho_\phi) - \mathcal{J}_\tau^{\text{Sym}}(\theta, \phi)| &\leq \frac{1}{2} \left(\int \rho_\theta \left| \log \frac{\rho_\phi}{\tilde{\rho}_{\phi,\tau}} \right| d\mu + \int \rho_\phi \left| \log \frac{\rho_\theta}{\tilde{\rho}_{\theta,\tau}} \right| d\mu \right) \\ &\leq \frac{1}{2} \left(\left\| \log \frac{\rho_\phi}{\tilde{\rho}_{\phi,\tau}} \right\|_\infty + \left\| \log \frac{\rho_\theta}{\tilde{\rho}_{\theta,\tau}} \right\|_\infty \right) \leq \frac{1}{2} \left(\frac{2\varepsilon_{\text{kde}}^{(\phi)}(\tau)}{\underline{\rho}_\phi} + \frac{2\varepsilon_{\text{kde}}^{(\theta)}(\tau)}{\underline{\rho}_\theta} \right) \leq \frac{\varepsilon_{\text{kde}}^{(\theta)}(\tau) + \varepsilon_{\text{kde}}^{(\phi)}(\tau)}{\min\{\underline{\rho}_\theta, \underline{\rho}_\phi\}}. \end{aligned}$$

This proves the claimed nonasymptotic bound for all $0 < \tau \leq \tau_0(\theta, \phi)$.

Step 3: Vanishing discrepancy as $\tau \rightarrow 0^+$. By Lem. C.3 applied to ρ_θ and ρ_ϕ (using Asm. 3.2),

$$\varepsilon_{\text{kde}}^{(\theta)}(\tau) \xrightarrow{\tau \rightarrow 0^+} 0, \quad \varepsilon_{\text{kde}}^{(\phi)}(\tau) \xrightarrow{\tau \rightarrow 0^+} 0.$$

Therefore, the bound in Step 2 implies

$$|\mathcal{J}_\tau^{\text{Sym}}(\theta, \phi) - \mathcal{F}_{\tau, \mathbf{U}_{\theta, \phi}}^{\text{Sym}}(\rho_\theta, \rho_\phi)| \xrightarrow{\tau \rightarrow 0^+} 0,$$

for any fixed pair $(\theta, \phi) \in \Theta \times \Phi$. □

F. Experimental Details

This section details the experimental procedures used to empirically validate our theoretical framework. Specifically, we provide comprehensive setups for evaluating: (i) the convergence of finite-batch InfoNCE gradients to their deterministic counterparts; (ii) the Gibbs-shaped concentration and spread behavior of unimodal training under sharp kernels; (iii) the emergence of a persistent, population-level modality gap induced by conditional heterogeneity; and (iv) the real-world implications of cross-modal divergence via probing and fine-tuning CLIP models on MS-COCO.

F.1. Large-Batch Gradient Consistency Across Critics

This experiment provides a numerical validation of the large-batch consistency established in Thm. 3.1. We verify that as the number of negatives N increases, the stochastic InfoNCE descent direction aligns increasingly well with the deterministic energy gradient. Crucially, since the multimodal symmetric objective (Eq. (2)) is the sum of two directional terms, establishing consistency for the unimodal gradient implies consistency for the full multimodal objective by linearity.

Data and pairing. We construct a synthetic unimodal dataset in $\mathcal{X} \subset \mathbb{R}^m$ ($m = 64$) from a mixture of $K = 4$ Gaussians: $\mathbf{x} \sim \sum_{k=1}^K \pi_k \mathcal{N}(\boldsymbol{\mu}_k, \sigma^2 \mathbf{I})$. The component means $\{\boldsymbol{\mu}_k\}$ are random directions scaled by a separation factor of 4, with $\sigma = 1$. Positive pairs are generated via an additive noise $\tilde{\mathbf{x}} = \mathbf{x} + \boldsymbol{\varepsilon}$, where $\boldsymbol{\varepsilon} \sim \mathcal{N}(\mathbf{0}, \sigma_{\text{aug}}^2 \mathbf{I})$. Negative samples $\{\mathbf{x}_j^-\}_{j=1}^N$ are i.i.d. draws from the same data distribution.

Encoder and regimes. We employ a linear encoder $f_{\mathbf{W}}(\mathbf{x})$ with parameters $\mathbf{W} \in \mathbb{R}^{n \times m}$ ($n = 128$) under two distinct geometric regimes:

$$\mathbf{z} = f_{\mathbf{W}}(\mathbf{x}) = \begin{cases} \text{normalize}(\mathbf{W}\mathbf{x}) \in \mathbb{S}^{n-1}, & \text{(Spherical regime)} \\ \tanh(\mathbf{W}\mathbf{x}) \in [-1, 1]^n, & \text{(Compact Euclidean regime)}. \end{cases}$$

The spherical case corresponds to the standard feature-normalized setting, while the compact Euclidean case mirrors our theoretical assumption of a compact \mathcal{Z} without enforcing explicit normalization, allowing for distance-based critics.

We evaluate the exponential kernel defined in § 2 with the two canonical critics: the cosine critic $s_{\text{cos}}(\mathbf{z}, \mathbf{w}) = \langle \mathbf{z}, \mathbf{w} \rangle$ and the RBF critic $s_{\text{rbf}}(\mathbf{z}, \mathbf{w}) = -\frac{1}{n} \|\mathbf{z} - \mathbf{w}\|^2$, with temperatures $\tau_{\text{cos}} = 0.1$ and $\tau_{\text{rbf}} = 1.0$, respectively. The RBF critic includes $1/n$ scaling to maintain $O(1)$ logits. We set augmentation noise $\sigma_{\text{aug}} = 0.05$ for the cosine regime and $\sigma_{\text{aug}} = 0.2$ for the RBF regime.

Loss and gradients. For each seed, we sample a fixed batch of $B = 64$ anchors/positives and a large “reference” pool of $N_{\text{ref}} = 4096$ negatives. For a given N , we compute the loss $\hat{\ell}_{B,N}(\mathbf{W})$ using the first N negatives from this pool:

$$\hat{\ell}_{B,N}(\mathbf{W}) = \frac{1}{B} \sum_{i=1}^B \left[-\frac{1}{\tau} s(\mathbf{z}_i, \tilde{\mathbf{z}}_i) + \log \left(\exp(s(\mathbf{z}_i, \tilde{\mathbf{z}}_i)/\tau) + \sum_{j=1}^N \exp(s(\mathbf{z}_i, \mathbf{w}_j^-)/\tau) \right) \right].$$

Let $\mathbf{g}_N := \nabla_{\mathbf{W}} \hat{\ell}_{B,N}(\mathbf{W})$ denote the gradient estimate using N negatives, and $\mathbf{g}_{\text{ref}} := \mathbf{g}_{N_{\text{ref}}}$ denote the high-fidelity reference gradient. Fixing the negative pool ensures that variations in \mathbf{g}_N are attributable solely to the sample size N .

Metrics and results. We sweep $N \in \{4, 8, 16, 32, 64, 128, 256, 512, 1024\}$ and report two metrics: (i) *gradient alignment* $\cos(\mathbf{g}_N, \mathbf{g}_{\text{ref}})$, measuring directional accuracy; and (ii) *relative error* $\|\mathbf{g}_N - \mathbf{g}_{\text{ref}}\|/\|\mathbf{g}_{\text{ref}}\|$, measuring magnitude deviation. Results are averaged over 20 random seeds; error bars indicate ± 1 standard deviation across seeds. As shown in Fig. 3, across both the spherical and RBF regimes, the gradient alignment score increases monotonically with N while the relative error decreases. This confirms our theoretical claims: as the denominator concentrates, the stochastic InfoNCE gradient converges to the deterministic energy gradient. The rapid convergence (alignment > 0.95 at $N = 256$) suggests that the large-batch energy landscape is a faithful proxy for practical training dynamics even at moderate batch sizes.

F.2. Unimodal Gibbs Equilibrium and Low-Temperature Concentration

This experiment provides a numerical verification of the intrinsic unimodal geometry characterized in § 3. Specifically, we validate the variational perspective by demonstrating that: (i) for fixed $\tau > 0$, the functional $\mathcal{F}_{\tau,U}$ admits a unique Gibbs-type equilibrium (Prop. 3.1); and (ii) as $\tau \rightarrow 0^+$, this equilibrium concentrates exponentially around the minimizers of U , confirming the ground-state convergence predicted in Prop. 3.2.

Representation space and potential field. We define the domain as the unit sphere $\mathcal{Z} = \mathbb{S}^2 \subset \mathbb{R}^3$ equipped with surface measure μ and geodesic distance $d_{\mathbb{S}^2}$. We construct a smooth, non-isotropic potential $U(\mathbf{z})$ using a log-sum-exp mixture of two von-Mises–Fisher-like modes:

$$U(\mathbf{z}) := -\frac{1}{\gamma} \log(w \exp(\kappa \langle \mathbf{z}, \mathbf{m}_1 \rangle) + (1-w) \exp(\kappa \langle \mathbf{z}, \mathbf{m}_2 \rangle)), \quad \mathbf{z} \in \mathbb{S}^2, \quad (74)$$

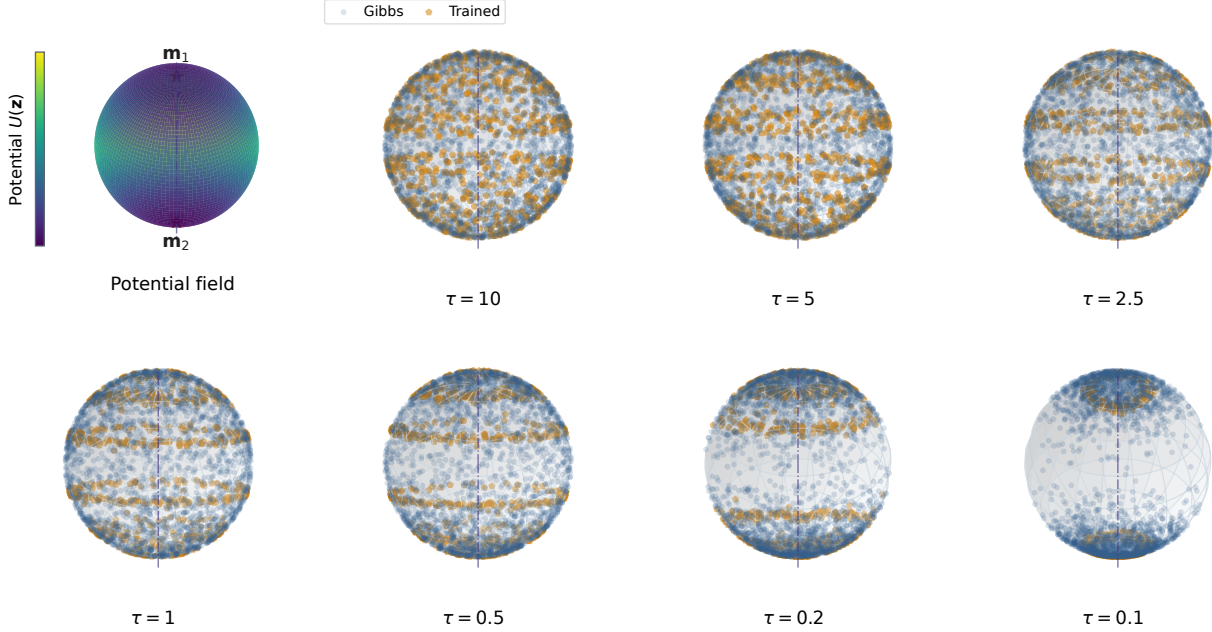


Figure 7. Unimodal potential landscape on \mathbb{S}^2 and equilibria across temperature τ . Left top: the 2-well potential U in Eq. (74) (colored by value), with minima centers $\mathbf{m}_1, \mathbf{m}_2$. Others: Gibbs samples (blue; importance-resampled) and trained particles (orange; minimizing Eq. (76)) across various temperatures. As τ decreases, both distributions concentrate around the low-energy wells.

with $\gamma = 12$, concentration $\kappa = 12$, and mixture weight $w = 0.5$. The modes are centered at $\mathbf{m}_1 = (0, 0, 1)$ and a separated direction $\mathbf{m}_2 = (0.85, 0.15, -0.50)/\|(0.85, 0.15, -0.50)\|$, creating two distinct low-energy basins (Fig. 7, left top).

Particle training objective. To emulate minimization of $\mathcal{F}_{\tau, U}(\rho) = \frac{1}{\tau} \int_{\mathcal{Z}} U \rho \, d\mu - H(\rho)$ (Def. 3.3) without committing to a parametric encoder, we represent ρ by M particles $\{\mathbf{z}_i\}_{i=1}^M \subset \mathbb{S}^2$ and optimize a standard particle/KDE surrogate. We parameterize unconstrained variables $\{\mathbf{v}_i\}_{i=1}^M \subset \mathbb{R}^3$ and project to the sphere $\mathbf{z}_i = \mathbf{v}_i/\|\mathbf{v}_i\|$ at each iteration. We approximate the density at particle locations by a wrapped Gaussian kernel on the sphere,

$$\hat{\rho}_h(\mathbf{z}_i) := \frac{1}{M} \sum_{j=1}^M \exp\left(-\frac{d_{\mathbb{S}^2}(\mathbf{z}_i, \mathbf{z}_j)^2}{2h^2}\right), \quad (75)$$

with bandwidth $h = 0.35$. The optimized objective is the particle approximation

$$\hat{\mathcal{F}}_{\tau, U}(\{\mathbf{z}_i\}) := \frac{1}{\tau} \cdot \frac{1}{M} \sum_{i=1}^M U(\mathbf{z}_i) + \frac{1}{M} \sum_{i=1}^M \log \hat{\rho}_h(\mathbf{z}_i), \quad (76)$$

where the second term is the KDE-based surrogate for $-H(\rho)$ up to an additive constant. We minimize Eq. (76) using Adam (Kingma & Ba, 2015) for 5000 steps with learning rate 5×10^{-2} , while injecting Gaussian noise from $\mathcal{N}(\mathbf{0}, \sigma^2 \mathbf{I})$ with $\sigma = 0.06$ at each iteration. This injection approximates a Langevin diffusion process (Welling & Teh, 2011), ensuring that the particles maintain active exploration of the landscape to escape shallow local traps, while the gradient of the entropy term drives the global dispersion.

We sweep $\tau \in \{10, 5.0, 2.5, 1.0, 0.5, 0.2, 0.1\}$ and run 20 seeds. As a reference, we estimate the Gibbs equilibrium $\rho_{\tau}^*(\mathbf{z}) \propto \exp(-U(\mathbf{z})/\tau)$ (Prop. 3.1) by importance sampling: we draw $n_{\text{mc}} = 120,000$ uniform points on \mathbb{S}^2 , weight by $\exp(-U/\tau)$, and compute weighted expectations. For visualization, we use a separate pool of 24,000 uniform points and perform weighted sampling without replacement to draw 2400 Gibbs points per τ .

Evaluation metric. To quantify low- τ concentration, we report the *cap mass* within geodesic radius $\varepsilon = 0.50$ around either potential well: $\text{CapMass}_{\varepsilon}(\rho) := (\rho \mu)(\mathcal{C}_{\varepsilon}(\mathbf{m}_1) \cup \mathcal{C}_{\varepsilon}(\mathbf{m}_2))$, where $\mathcal{C}_{\varepsilon}(\mathbf{m}) := \{\mathbf{z} \in \mathbb{S}^2 : d_{\mathbb{S}^2}(\mathbf{z}, \mathbf{m}) \leq \varepsilon\}$. For the

trained particles, this is simply the fraction of particles whose distance to $\{\mathbf{m}_1, \mathbf{m}_2\}$ is at most ε . For the Gibbs baseline, we compute the same quantity as a weighted Monte Carlo estimate. We report the mean \pm standard error over the 20 seeds.

Results. Fig. 7 visualizes the potential landscape and the learned equilibrium across τ . At high temperature (e.g., $\tau = 10$), both the Gibbs samples and the trained particles spread broadly over the sphere: the entropy term in $\mathcal{F}_{\tau,U}$ is comparatively strong, producing a diffuse equilibrium consistent with the “entropic dispersion” force. As τ decreases (e.g., $\tau = 0.2, \tau = 0.1$), the potential term $\frac{1}{\tau} \int_{\mathcal{Z}} U \rho d\mu$ dominates, and both distributions increasingly concentrate near the two low-energy basins. Notably, the trained particles exhibit semi-regular lattice-like bands, in contrast to the purely random scatter of the Gibbs samples. This micro-structure is an intrinsic consequence of the optimization: the KDE entropy term induces a repulsive force between particles, causing them to self-organize into low-discrepancy packing configurations to maximize mutual separation. This behavior is a known feature of particle-based variational inference, where it effectively yields a variance-reduced discretization of the target density (Liu & Wang, 2016). Crucially, this microscopic regularity does not violate the macroscopic prediction: at $\tau = 0.1$, the global mass is visibly localized around the wells, matching the qualitative prediction of ground-state concentration (Prop. 3.2).

This trend is quantified in Fig. 2a: the cap mass $\text{CapMass}_\varepsilon(\rho)$ increases as τ decreases for both the Gibbs baseline and the trained particles. The trained curve closely tracks the trend, with small deviations attributable to finite particle count M , finite optimization time, and the fixed KDE bandwidth h which imposes a smoothing scale on the entropy surrogate. Overall, the experiment supports the unimodal message: minimizing the free-energy produces a unique Gibbs-type equilibrium at each τ , and the equilibrium exhibits systematic low-temperature concentration near minimizers of U , thereby validating the mechanistic picture used to analyze the unimodal parametric energy in § 3.

E.3. Multimodal Structural Gap under Controlled Misalignment

This experiment provides a controlled empirical validation of the *multimodal* mechanism developed in § 4, grounded in the well-documented *modality gap* phenomenon observed in CLIP-style training (Liang et al., 2022). Our theory explains this gap as an objective-induced geometric necessity: although symmetric multimodal InfoNCE admits a stable large-batch deterministic limit, its intrinsic landscape is inherently *cross-coupled*, with equilibrium determined by the interplay of two directional alignment fields. When the two modalities exhibit heterogeneous conditional laws—arising from noise, distinct semantic density, or mismatched semantic structure—these fields generically fail to share a common potential, yielding a persistent negative symmetric divergence. We test this mechanism in a controlled setting by showing that exact marginal matching is a *knife-edge* condition: even mild, structured misalignment introduces a structural wedge that forces the population-level marginals apart.

Latent variables and paired observations. We generate paired observations $(\mathbf{x}_1, \mathbf{x}_2)$ representing two modalities that stem from a shared latent angle $\alpha \in (-\pi, \pi]$. To strictly rule out the trivial solution where marginals are uniform (and thus trivially match regardless of noise), we sample the shared latent α from a *non-uniform*, multi-peaked mixture of von Mises–Fisher distributions:

$$\alpha \sim w \text{VM}(\mu_1, \kappa) + (1 - w) \text{VM}(\mu_2, \kappa), \quad \text{with } w = 0.7, \mu_1 = 0, \mu_2 = \pi, \kappa = 6.$$

Both modalities observe this angle as a projection onto the 2D unit circle, corrupted by independent Gaussian observation noise $\xi_1, \xi_2 \sim \mathcal{N}(\mathbf{0}, \sigma_{\text{obs}}^2 \mathbf{I})$, where $\sigma_{\text{obs}} = 0.02$. Modality 1 is generated by mapping the shared latent directly to the observation space:

$$\mathbf{x}_1 := [\cos \alpha, \sin \alpha]^\top + \xi_1.$$

Modality 2 observes a *misaligned* version of the latent. We introduce an additive angular shift $\eta \sim \mathcal{N}(0, \sigma_{\text{mis}}^2)$ before mapping it to the observation space:

$$\mathbf{x}_2 := [\cos(\alpha + \eta), \sin(\alpha + \eta)]^\top + \xi_2.$$

Thus, increasing the variance of the misalignment σ_{mis} increases the *cross-modal conditional mismatch* between \mathbf{x}_1 and \mathbf{x}_2 , while keeping the marginal complexity of both modalities comparable.

Encoders, learning objective, and protocol. To isolate the directional alignment dynamics and prevent magnitude from confounding the representation geometry, we apply bias-free linear encoders $f, g : \mathbb{R}^2 \rightarrow \mathbb{R}^2$ to the observed modalities.

The unnormalized embeddings $\tilde{\mathbf{z}}_1 = f(\mathbf{x}_1)$ and $\tilde{\mathbf{z}}_2 = g(\mathbf{x}_2)$ are then projected onto the unit circle:

$$\mathbf{z}_1 = \frac{\tilde{\mathbf{z}}_1}{\|\tilde{\mathbf{z}}_1\|}, \quad \mathbf{z}_2 = \frac{\tilde{\mathbf{z}}_2}{\|\tilde{\mathbf{z}}_2\|} \in \mathbb{S}^1.$$

We adopt a cosine similarity critic $s(\mathbf{z}, \mathbf{w}) = \langle \mathbf{z}, \mathbf{w} \rangle$ and an corresponding exponential kernel $\kappa_\tau(\mathbf{z}, \mathbf{w}) = \exp(s(\mathbf{z}, \mathbf{w})/\tau)$ with a temperature of $\tau = 0.07$. This kernel directly instantiates the InfoNCE objective central to our multimodal analysis. Specifically, for a batch of N paired observations, training minimizes the symmetric CLIP loss:

$$\mathcal{L}_{\text{CLIP}}(f, g) = \frac{1}{2}(\mathcal{L}_{\text{CE}}(\mathbf{S}/\tau, \mathbf{y}_{\text{diag}}) + \mathcal{L}_{\text{CE}}(\mathbf{S}^\top/\tau, \mathbf{y}_{\text{diag}})),$$

where $\mathbf{S} \in \mathbb{R}^{N \times N}$ is the pairwise similarity matrix with entries $\mathbf{S}_{ij} := \langle \mathbf{z}_{1,i}, \mathbf{z}_{2,j} \rangle$, \mathcal{L}_{CE} denotes the standard cross-entropy loss, and the target \mathbf{y}_{diag} indicates that the matched positive pairs lie strictly on the diagonal ($i = j$).

Using Adam with learning rate 5×10^{-3} for 2000 steps and batch size as 256. We sweep eight misalignment scales $\sigma_{\text{mis}} \in \{0, 0.1, 0.2, 0.3, 0.4, 0.5, 0.6, 0.7\}$; larger scales induce progressively more severe cross-modal misalignment, yet all settings retain a meaningful statistical dependence between positive pairs. For each σ_{mis} , we repeat training over 20 random seeds (seeds 0–19). The large batch size makes the training dynamics closer to the large-batch deterministic regime in Thm. 4.1, whose proof follows the same Monte-Carlo concentration logic as the asymmetric case but applied to the bidirectional symmetric normalization.

Evaluation metrics. After training, we evaluate the learned representations on $n_{\text{eval}} = 8000$ fresh paired samples. For the unit-normalized embeddings $\mathbf{z}_1, \mathbf{z}_2 \in \mathbb{S}^1$, we compute the embedding angles $a_1 = \text{atan2}(\mathbf{z}_{1,y}, \mathbf{z}_{1,x})$ and $a_2 = \text{atan2}(\mathbf{z}_{2,y}, \mathbf{z}_{2,x})$, where the subscripts x and y denote the respective coordinate axes. The following visual diagnostics are considered: (i) *Marginal gap.* We discretize a_1 and a_2 into 60 bins on $(-\pi, \pi]$ and estimate the two empirical angle marginals $\hat{\rho}_\theta$ and $\hat{\rho}_\phi$. As a scalar summary of marginal mismatch, we report the symmetric KL divergence $D_{\text{KL}}^{\text{Sym}}(\hat{\rho}_\theta, \hat{\rho}_\phi)$ averaged over 20 random seeds (seeds 0–19), with error bars or shadow areas showing \pm standard error. (ii) *Polar marginals.* To visualize *where* the mismatch occurs on the circle, we plot the two estimated angle marginals as polar density curves for each misalignment scale σ_{mis} . (iii) *Joint-angle heatmaps.* To visualize the learned *cross-modal coupling* beyond marginals, we plot a log-scaled 2D histogram, i.e., a $\log(1 + \text{count})$ heatmap, of the joint distribution of (a_1, a_2) . Diagonal concentration indicates near-deterministic alignment $a_2 \approx a_1$; off-diagonal spread indicates systematic cross-modal mismatch. (iv) *Angle-shift density.* Finally, we compute the wrapped angular difference $\Delta a := \text{wrap}(a_2 - a_1) \in (-\pi, \pi]$ and plot its empirical density. This directly measures the distribution of residual misalignment in embedding space.

For the scalar marginal-gap curve, we average over 20 random seeds and report the mean with a \pm SEM band. For the qualitative diagnostics (polar marginals, joint-angle heatmaps, and angle-shift densities), we display one fixed representative run (seed 0) and reuse the same held-out latent sample across all misalignment scales, matching the animation setup.

Results. Fig. 2b shows that the marginal discrepancy $D_{\text{KL}}^{\text{Sym}}(\hat{q}_\theta, \hat{q}_\phi)$ increases as the latent misalignment scale σ_{mis} grows. Since the encoder architecture, critic function, and optimization protocol remain fixed across all runs, this result isolates the conditional mismatch σ_{mis} as the primary driver of the gap. It confirms that as the two modalities become less conditionally compatible, the symmetric InfoNCE objective is forced to sacrifice marginal alignment, inducing a persistent modality separation that cannot be resolved by optimization alone.

The polar marginals in Fig. 8 provide a structural view of *how* this separation manifests geometrically. First, across all settings ($\sigma_{\text{mis}} \geq 0$), the learned angular marginals are clearly *multi-peaked* rather than uniform. The density concentrates in specific angular regions, reflecting the underlying non-uniform latent law (a two-component von Mises–Fisher mixture) and confirming that the encoders successfully recover the latent structure up to a global rotation. Second, the evolution of these peaks reveals the gap mechanism. At $\sigma_{\text{mis}} = 0$, the polar curves for the two modalities nearly overlap, consistent with a compatible pairing law where symmetric InfoNCE can simultaneously achieve alignment and marginal coincidence. However, for any $\sigma_{\text{mis}} > 0$, the curves begin to diverge within the same modal regions: the peaks shift relative to each other, and their probability masses differ. This mismatch becomes visually more pronounced as σ_{mis} increases, tracking the quantitative rise in the gap curve.

The joint-angle heatmaps in Fig. 9 elucidate the mechanism behind this separation. At $\sigma_{\text{mis}} = 0$, probability mass concentrates sharply along the diagonal $a_2 \approx a_1$, indicating a near-deterministic coupling. Because the latent distribution is bimodal, this diagonal concentration is not uniform but forms distinct bright spots (high-density clusters) corresponding to

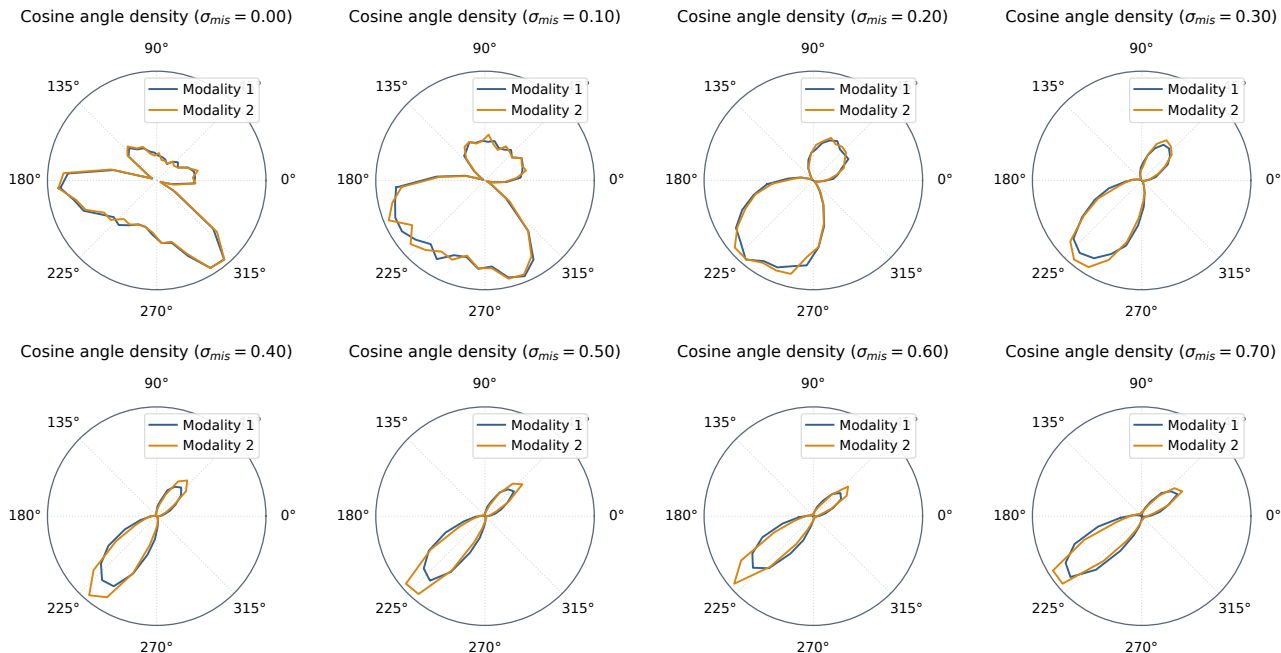


Figure 8. Polar marginals across misalignment. Estimated angle marginals of the two modalities on S^1 . The mismatch becomes visually apparent for $\sigma_{\text{mis}} > 0$ and grows with σ_{mis} .

the latent modes. As σ_{mis} increases, these clusters persist—indicating the model still captures the coarse latent semantics—but they deform into thickened, elongated ellipses. The diagonal band broadens significantly, reflecting that the conditional law of a_2 given a_1 has become intrinsically noisy. Crucially, this is not merely a symmetric blur around the diagonal; the deformation is accompanied by the shifts in marginal occupancy observed in Fig. 8. This confirms that under the symmetric objective, broadening conditional alignment structurally necessitates a shift in the marginal supports.

Finally, the angle-shift densities in Fig. 10 quantify the residual embedding misalignment $\Delta a = \text{wrap}(a_2 - a_1)$. As σ_{mis} increases, the distribution of Δa transitions from a sharp peak at zero to a progressively wider distribution with heavy tails. The residual shift becomes both larger in magnitude and more variable, matching the signature expected from the injection of additive latent noise $\eta \sim \mathcal{N}(0, \sigma_{\text{mis}}^2)$.

In summary, these empirical patterns provide direct validation for the multimodal mechanism characterized in § 4. Our theoretical analysis posits that the symmetric objective consists of two directional alignment fields coupled via their marginals. In this experiment, the controlled perturbation $\alpha + \eta$ creates heterogeneous conditional laws, meaning the optimal alignment from Modality 1 to Modality 2 is no longer the inverse of the alignment from Modality 2 to Modality 1. Consequently, the two directions of the symmetric objective cannot be governed by a single, unified potential function. Empirically, this manifests as a geometric tug-of-war between the modalities, yielding two distinct observable effects: (i) The broadening diagonal band in Fig. 9 reflects the necessary rise in conditional entropy driven by the mismatched conditionals. (ii) The widening marginal separation in Fig. 2b and Fig. 8 confirms our prediction that marginal coincidence is a fragile, knife-edge property that rapidly destabilizes once misalignment is introduced. Together, these observations demonstrate that the population-level modality gap is neither a finite-sample artifact nor a symptom of under-training. Rather, it is a fundamental consequence of the objective’s geometry: when strict pairwise compatibility is violated (here, for any $\sigma_{\text{mis}} > 0$), the symmetric InfoNCE equilibrium inherently cannot maintain identical marginals.

E.4. MS-COCO Experiments: Pretrained Gap and Controlled Pair Corruption

We complement the synthetic experiments with two studies on MS-COCO. The first is an observational study of pretrained CLIP-like models, designed to assess whether these models exhibit a modality gap and whether improved retrieval performance necessarily corresponds to a smaller cross-modal distributional discrepancy. The second is a controlled intervention study designed to test whether weakening image-text compatibility during training systematically enlarges the

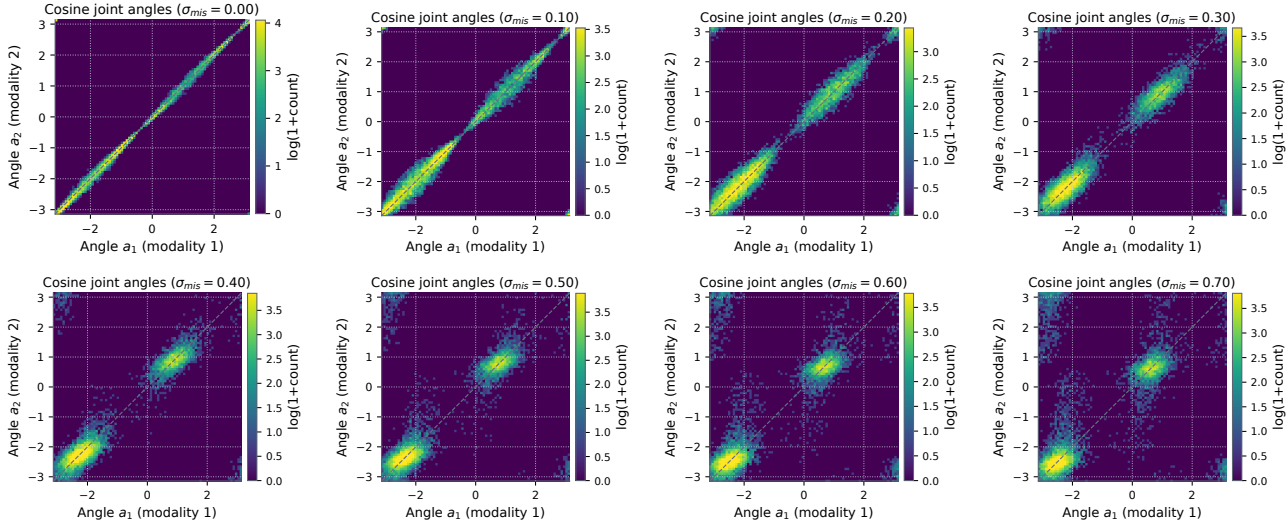


Figure 9. Joint-angle coupling across misalignment. 2D histograms of (a_1, a_2) from $\sigma_{\text{mis}} = 0.0$ to $\sigma_{\text{mis}} = 0.7$. Diagonal concentration (small σ_{mis}) indicates near-deterministic alignment; increasing off-diagonal spread (large σ_{mis}) indicates intrinsically noisy coupling.

Table 2. Retrieval performance and cross-modal discrepancy for pretrained OpenCLIP checkpoints evaluated on the first 5,000 images of MS-COCO val_{2017} . Retrieval is reported as image-to-text and text-to-image Recall@1. Cross-modal discrepancy is quantified by the energy distance, RBF-MMD² at the median bandwidth, the centroid gap $\|\mu_I - \mu_T\|$, and centroid cosine similarity. Lower energy distance, MMD², and centroid gap indicate smaller cross-modal discrepancy.

Model	I→T R@1	T→I R@1	$\mathcal{E}(p_I, p_T)$	$\text{MMD}_{\sigma=\text{med}}^2$	$\ \mu_I - \mu_T\ $	$\cos(\mu_I, \mu_T)$
PE-Core-L-14	0.741	0.559	0.599	0.255	0.854	0.097
PE-Core-B-16	0.703	0.499	0.545	0.237	0.808	0.189
ViT-bigG-14	0.670	0.506	0.288	0.129	0.598	0.384
ViT-H-14	0.662	0.485	0.375	0.159	0.697	0.048
ViT-L-14	0.569	0.357	0.697	0.303	0.898	0.184
ResNet-50x16	0.559	0.354	0.502	0.230	0.761	0.349
RN101	0.498	0.299	0.443	0.228	0.670	0.604
ViT-B-16	0.492	0.302	0.688	0.313	0.871	0.309
ResNet-50	0.480	0.289	0.627	0.276	0.849	0.237

modality gap. Together, these studies relate the intrinsic geometric analysis to realistic image-text representations.

F.4.1. PROBING PRETRAINED MODELS ON MS-COCO

Setup and evaluations. We evaluate a collection of pretrained CLIP (using the OpenCLIP (Ilharco et al., 2021) official artifacts) checkpoints on MS-COCO val_{2017} . For each checkpoint, we use the first 5000 validation images and up to 5 captions per image, yielding one normalized image embedding (\mathbf{z}_I) per image and one normalized text embedding (\mathbf{z}_T) per caption. Retrieval is evaluated in both directions under the many-captions-to-one-image matching protocol. Image-to-text Recall@ K assesses whether any of the top- K retrieved captions is associated with the query image, whereas text-to-image Recall@ K assesses whether the correct image appears among the top- K retrieved images for a given caption. We report retrieval performance using Recall@1 (R@1), and define AvgR@1 as the mean of the R@1 scores in the two retrieval directions.

To quantify cross-modal discrepancy, we compute the centroid gap

$$\|\mu_I - \mu_T\|, \quad \text{with } \mu_I = \mathbb{E}[\mathbf{z}_I], \mu_T = \mathbb{E}[\mathbf{z}_T],$$

and the energy distance

$$\mathcal{E}(p_I, p_T) = 2\mathbb{E}[d(\mathbf{z}_I, \mathbf{z}_T)] - \mathbb{E}[d(\mathbf{z}_I, \mathbf{z}'_I)] - \mathbb{E}[d(\mathbf{z}_T, \mathbf{z}'_T)],$$

where p_I and p_T denote the image and text embedding marginals, $\mathbf{z}_I, \mathbf{z}'_I \sim p_I$ and $\mathbf{z}_T, \mathbf{z}'_T \sim p_T$ are independent laws, and

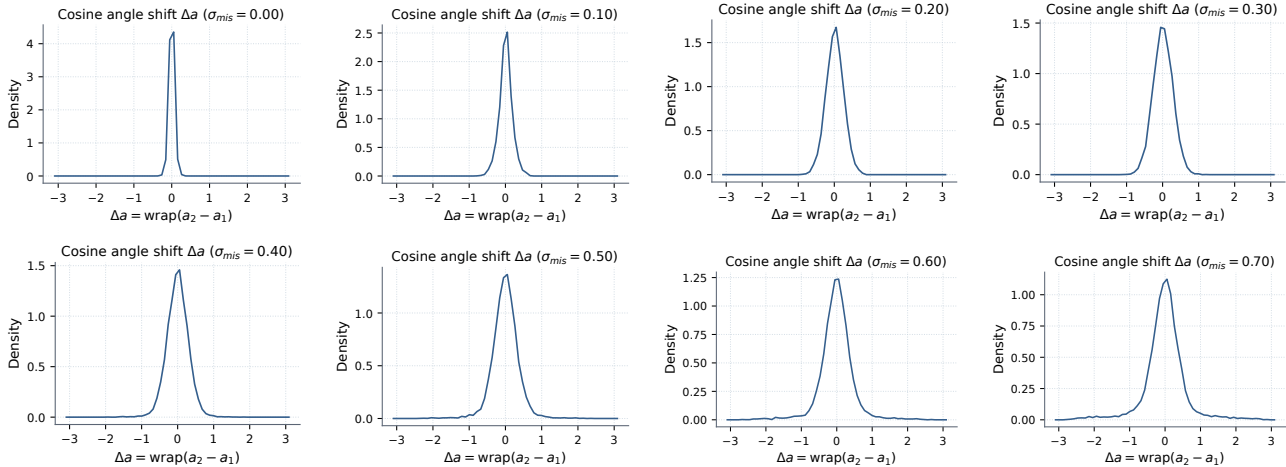


Figure 10. Residual embedding-space misalignment. Densities of $\Delta a = \text{wrap}(a_2 - a_1)$ from $\sigma_{\text{mis}} = 0.0$ to $\sigma_{\text{mis}} = 0.7$. The distribution broadens as σ_{mis} increases, indicating larger and more variable residual misalignment in representation space.

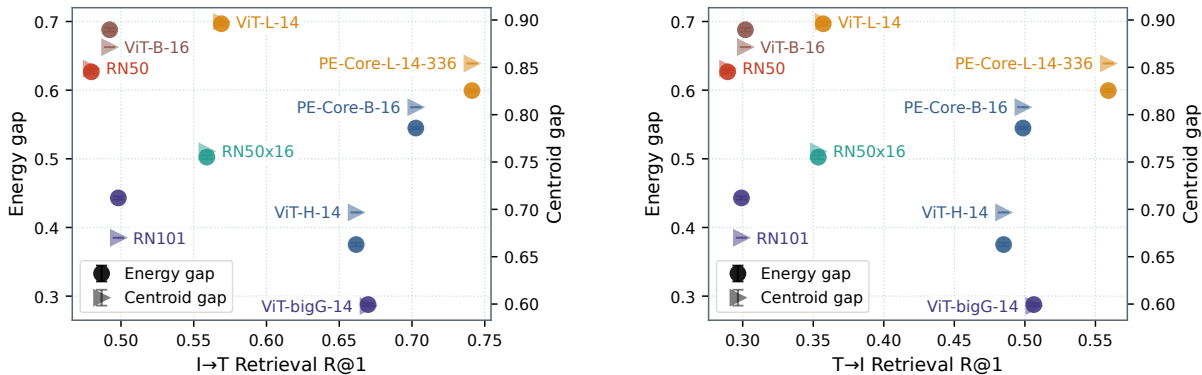


Figure 11. Directional retrieval versus cross-modal gap on MS-COCO for pretrained OpenCLIP checkpoints. Left: image-to-text retrieval ($I \rightarrow T$ R@1) versus gap. Right: text-to-image retrieval ($T \rightarrow I$ R@1) versus gap. In both panels, the left y-axis shows energy distance and the right y-axis shows centroid gap. The relation is clearly non-monotone: models with similar directional retrieval can exhibit substantially different cross-modal discrepancy. This confirms that retrieval performance and modality gap are related but not equivalent, and that strong pretrained models may still maintain a substantial structural separation between image and text marginals.

$d(\cdot, \cdot)$ is the Euclidean distance between normalized embeddings. Whereas the centroid gap captures only the separation between the modality means, the energy distance compares cross-modal distances with within-modal distances and thus provides a broader measure of distributional mismatch. Unlike retrieval, which evaluates alignment between matched image-caption pairs, the energy distance operates at the distribution level: it is small when image and text embeddings are well mixed and large when cross-modal distances remain systematically greater than within-modal distances. We additionally report an RBF-MMD diagnostic using a bandwidth selected by the median-distance heuristic.

Results. As shown in Tab. 2, the results indicate that retrieval and cross-modal discrepancy are only partially aligned. As already seen in the AvgR@1 plot in Fig. 6 (left), better retrieval often corresponds to a smaller gap, but the trend is clearly non-monotone. For instance, PE-Core-L-14 achieves the best retrieval yet still has a large energy distance and centroid gap, whereas ViT-bigG-14 attains slightly lower retrieval but the smallest gap values in the table. The separate $I \rightarrow T$ and $T \rightarrow I$ versus gap plots (Fig. 11) show that this is not caused by averaging: models with nearly identical directional retrieval can still differ substantially in energy and centroid discrepancy, e.g., ViT-bigG-14 versus PE-Core-B-16 in $T \rightarrow I$ retrieval, or ViT-L-14 versus ResNet-50x16 in $I \rightarrow T$ retrieval. The RBF-MMD values follow the same broad ordering, confirming that the effect is not metric-specific. Overall, these results show that the modality gap persists even in strong pretrained CLIP variants and is not reducible to retrieval performance alone; instead, it reflects an additional geometric property of the learned image and text marginals.

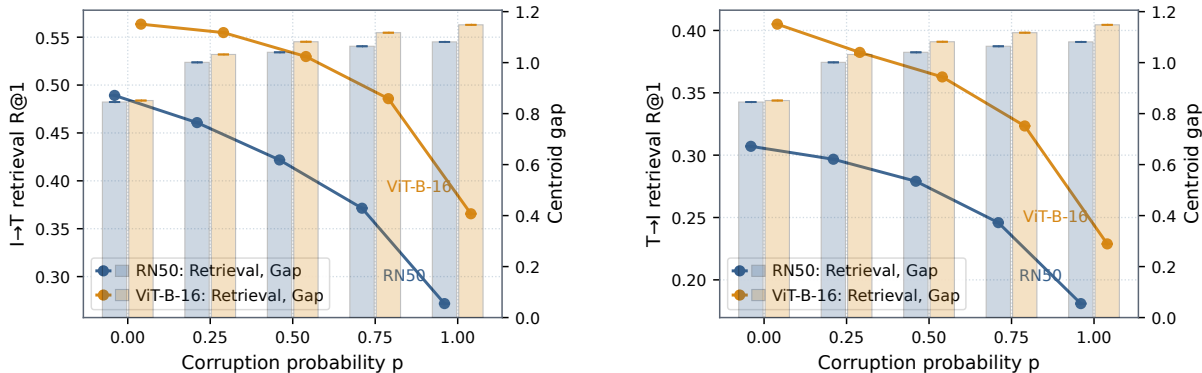


Figure 12. Directional retrieval under same-category caption corruption on MS-COCO. Left: image-to-text retrieval (I→T R@1) versus corruption probability p . Right: text-to-image retrieval (T→I R@1) versus p . Bars show the centroid gap on the right axis. For both RN50 and ViT-B-16, increasing same-category mispairing degrades retrieval in both directions while systematically enlarging the modality gap.

F.4.2. CONTROLLED SAME-CATEGORY PAIR CORRUPTION ON MS-COCO

Setup and evaluations. To test more directly whether weakening image–text compatibility enlarges the modality gap, we perform a controlled corruption experiment on MS-COCO train_{2017} . We first build an index that records, for each image, its caption set, its COCO category labels, and the pool of other images sharing each category. During training, the image is always kept fixed. With probability $1 - p$, we pair it with one of its own captions; with probability p , we instead replace the caption by a randomly chosen caption from a *different* image that shares at least one category with the current image. Thus, the corruption preserves coarse semantic relatedness while breaking exact instance-level correspondence. We sweep the corruption probability over $p \in \{0, 0.25, 0.50, 0.75, 1.00\}$.

We fine-tune pretrained OpenCLIP backbones (ResNet-50 and ViT-B-16) using the standard symmetric CLIP loss. To isolate the effect of pair corruption rather than full-model adaptation, we freeze the backbone towers and update only the projection heads together with the logit scale. Training uses AdamW with learning rate 10^{-5} , weight decay 0.05, batch size 256, and 5000 optimization steps. Evaluation follows the same protocol as in the previous experiment: we encode the first 5000 images of MS-COCO val_{2017} together with up to 5 captions per image, report image-to-text and text-to-image Recall@1, and define AvgR@1 as their mean. As the geometric diagnostic, we report the centroid gap $\|\mu_I - \mu_T\|$.

Results. As shown in Fig. 6 (right), the effect of corruption is clean for both backbones. As the caption corruption probability p increases, retrieval performance degrades while the centroid gap grows. For ResNet-50, AvgR@1 drops from 0.398 at $p = 0$ to 0.226 at $p = 1$, while the centroid gap increases from 0.845 to 1.081. For ViT-B-16, AvgR@1 drops from 0.484 to 0.297, while the centroid gap rises from 0.851 to 1.148. The same pattern holds in both retrieval directions, as shown in Fig. 12: for ResNet-50, I→T R@1 decreases from 0.489 to 0.272 and T→I R@1 from 0.307 to 0.181; for ViT-B-16, I→T R@1 decreases from 0.564 to 0.366 and T→I R@1 from 0.405 to 0.229.

Several aspects of this trend are important. First, the corruption is not arbitrary: the replacement caption is sampled from a same-category image, so the supervisory signal remains semantically plausible at a coarse level. Nevertheless, this weaker form of mispairing is already sufficient to produce a substantial geometric separation between image and text marginals. Second, the centroid gap reacts very early: even moving from $p = 0$ to $p = 0.25$ causes a sharp increase in gap for both ResNet-50 and ViT-B-16, while the retrieval drop is initially much milder. This suggests that cross-modal distributional separation is highly sensitive to degradation in pairwise compatibility, and may emerge before retrieval collapses. Third, the monotone behavior is consistent across both architectures, indicating that the phenomenon is not tied to one particular backbone family.

Overall, this experiment provides a controlled real-data analogue of the theory developed in the main text. Exact image–text compatibility is progressively weakened, and the learned representations respond in two coupled ways: matched-pair retrieval worsens, and the image/text marginals drift farther apart. This is precisely the behavior predicted by the structural-gap view of symmetric contrastive learning: once pairwise compatibility is degraded, optimization can no longer maintain the same degree of cross-modal coincidence, and the modality gap widens systematically.

G. Discussion

Our analysis suggests that contrastive learning should be understood not only through pointwise alignment, but through the population geometry it induces on the representation space. In the large-batch regime, InfoNCE gives rise to deterministic fields and intrinsic energies over \mathcal{Z} . This perspective clarifies why strong retrieval performance can coexist with persistent modality-level discrepancies: pairwise matching does not by itself control the induced marginal geometry. In particular, the multimodal theory predicts that improving alignment alone need not eliminate the modality gap unless the population-level coupling is also reshaped. This points to a practical lesson for evaluation and objective design: beyond retrieval, one should monitor distributional diagnostics of the learned marginals, and interventions aimed at closing the gap should act on the induced geometry itself, for example, through explicit discrepancy regularization, shared reference fields, or other mechanisms that reduce the barrier-like coupling between modalities.

A second implication is that directionality is structural rather than incidental. Because the two conditional laws of the encoded pair distribution generally differ, the two modalities induce distinct directional potentials, so multimodal alignment cannot in general be reduced to a single shared field. This helps explain why gap behavior may differ across retrieval directions and why data curation, annotation structure, and modality-specific noise can materially affect optimization. At the same time, our conclusions are sharpest in the large-batch, low-temperature, compact-manifold regime considered here. Extending the analysis to finite-batch and finite-temperature training, heterogeneous geometries, and singular or boundary-supported measures remains important future work. More broadly, our theory characterizes the geometry induced by the objective; whether that geometry recovers meaningful latent structure is a separate question, requiring additional assumptions on the data-generating process and model class.